MULTI-SENSOR REMOTE SENSING FOR UNDERSTANDING THE INTERACTING ENVIRONMENTAL DISTURBANCES OF FOREST FIRE AND PLANT DISEASE

by

Yinan He

A dissertation submitted to the faculty of
The University of North Carolina at Charlotte
in partial fulfillment of the requirements
for the degree of Doctor of Philosophy in
Geography

Charlotte

2019

Approved by:

_____
Dr. Gang Chen

_____
Dr. Ross K. Meentemeyer

_____
Dr. Brian Magi

_____
Dr. Craig Allan

_____
Dr. Tao Hong

ABSTRACT

Yinan He. Multi-sensor Remote Sensing for Understanding the Interacting Environmental Disturbances of Forest Fire and Plant Disease. (Under the direction of DR. GANG CHEN)

Forests are increasingly affected by a variety of environmental disturbances, including emerging infectious diseases (EIDs) and wildfire, which have caused extensive tree mortality in forest biomass worldwide. Those two types of disturbances may interact and lead to unexpected patterns of tree mortality, posing great challenges to sustainable forest management. Compared to high-cost, labor intensive and time consuming field mensuration, remote sensing offers a low-cost, efficient, and timely solution for monitoring the disturbances over large and complex landscapes. However, the potential of remote sensing in understanding interacting disturbances has yet to be well investigated. To bridge the research gap, this study developed several models integrating multi-sensor remote sensing techniques to investigate the response of forest ecosystem to EID-wildfire interactions. There are three research objectives: (i) developing a remote sensing model to detect the long-term spatial patterns of EID-caused tree mortality in the forest that was simultaneously affected by non-EID disturbances; (ii) developing a remote-sensing model to estimate post-fire burn severity in the presence of forest EID; and (iii) assessing the role of wildfire in determining the spread pattern of EID and exploring the consequence of EID-wildfire interaction on forest recovery at the landscape scale. The study was conducted in the Big Sur ecosystem, where sudden oak death and wildfire coexist and cause a large number of tree deaths. For sudden oak death-caused tree mortality estimation, remote sensing and ecological species distribution modeling were integrated to capture the isolated, patchy distribution patterns of sudden

oak death for over a decade. The results revealed an annual disease infection rate of 7% from 2005 to 2016, which was consistent with field observations. For fire severity mapping, the proposed Disturbance Weighting Analysis Model (DWAM) decomposed the burn contribution from diseased and non-diseased trees using remote sensing technology and substantially improved the map accuracy. The outcome from DWAM indicated a 42% improvement of RMSE (root mean square error) as compared with a recently developed, high-performance model. Meanwhile, DWAM's superior performance was consistent across all three disease infection stages. Based on the derived disease and burn severity estimation, my research further found that wildfire played a significant role in shaping the spread patterns of sudden oak death and the forest landscapes were significantly altered even after eight years of fire occurrence when compared to the pre-fire status. This study demonstrates the feasibility of multi-sensor remote sensing in monitoring forest disturbance interactions at the landscape scale.

ACKNOWLEDGMENTS

The completion of this dissertation is attributed to many people's support.

I would like to extend my sincere gratitude to my advisor Dr. Gang Chen. This educational journey towards the doctorate would not have been possible without his positive presence, patient guidance and valuable suggestions made me successfully complete this study. He gave me much advice both in research or life. His guidance and patience provided me with an unprecedented research environment, prepared me to be a self-motivated and independent thinker, and helped me formulate my long-term career goals.

I would also like to thank my committee members, Dr. Craig Allan, Dr. Brian Magi, Dr. Ross K. Meentemeyer, and Dr. Tao Hong. Their instructions help broaden my horizon to accomplish my study and will always be valuable for my future career and academic research. Dr. Sheng-Guo Wang also deserves my sincere thanks. Without his generous funding support in the last year, I would not be able to complete this dissertation. I am deeply grateful to all my friends and colleagues from the Department of Geography and Earth Sciences at UNC Charlotte.

My deepest gratitude goes to my beloved wife, Juan Geng for providing me with constant love and motivation. I would like to express my special thanks to my parents for tolerating my rather long absence, their care and support motivate me to move on and be a better person.

To all people in my life, for inspiring and encouraging my educational journey, I am grateful.

TABLE OF CONTENTS

LIST OF TABLES

LIST OF FIGURES

INTRODUCTION

Research Background

Forest disturbances are defined as the events that cause changes in the structure and composition of a forest ecosystem, beyond the growth and death of individual organisms (Asner, 2013). They affect the biodiversity, stand structure, and functioning of the forest ecosystem in varying ways (Anderegg et al., 2013). Due to rapid environmental change and intensive human interventions, forest ecosystems are increasingly affected by multiple disturbances, including emerging infectious diseases (EIDs) and wildfire, which are presenting a considerable challenge to forest resource management. Recent studies discovered that wildfire dynamics can be affected by the invasion of exotic forest diseases or insects; meanwhile, the spatiotemporal patterns of disease/insect progression are also affected by wildfire events (Chen et al., 2015ab; Riley et al., 2019; Simler et al., 2018). Those two types of disturbances may interact and lead to unexpected patterns of tree mortality, making forest management a challenging task (Chen et al., 2017). Understanding the disturbance processes and the response of forest ecosystems to interacting disturbances can advance our understanding of ecosystem resilience and recovery, which supports sustainable forest resources management (Daniel et al., 2017).

Insects attack different strata of the tree, e.g., defoliators feed on leaves or needles, and bark/wood borers bore into the bark/wood; while forest diseases are generally caused by infectious and transmissible pathogens, such as bacteria, fungi, viruses, and helminths (Chen and Meentemeyer, 2016). Over the past few decades, the frequency and intensity of disease- and insect-caused disturbances have substantially increased, resulting in extensive tree mortality in key forest biomes worldwide (Cobb et

al. 2017; Dlamini et al. 2019; Oboite and Comeau, 2019; Seidl et al. 2014; Potterf et al. 2019). Forests are subject to recurring fires as another significant disturbance, which undermine the biodiversity and resilience of forest ecosystem (Chuvieco et al. 2019; Daniel et al. 2017; Pettinari and Chuvieco, 2017; Veraverbeke et al., 2018). Fires directly transform living and dead organic matter to charred or blackened residues (Kokaly et al., 2007; Lewis et al., 2007), affecting the structure, function, and spatial patterns of ecological succession (Turner et al., 1998; Metz et al., 2013). Wildfires and diseases/insects often co-occur in forest ecosystems, resulting in interacting disturbances (Turner 2010). Diseases/insects alter both physical and biological factors, affect wildfire dynamics and influence its severity by increasing surface fuels (Chen et al., 2017; Riley et al., 2019). Meanwhile, disease-/insect-caused tree mortality also increases landscape heterogeneity which may enhance the fire-resistance of a forest landscape (Lee et al., 2009). Wildfire damages the disease-/insect-infected hosts and alters the environment in which animals live, in turn, changes patterns of tree mortality and forest regeneration trajectories (Beh et al., 2012; Davis et al., 2012; Loehman et al., 2017; Powell et al., 2012; Sánchez-Pinillos et al., 2019).

While traditional field measurements are still the most accurate way to quantify such interacting disturbances, it becomes time-consuming and costly when applied to a wider range of areas at the regional or continental scale. Remote sensing provides a viable solution for effectively monitoring the effects of forest disturbances and is particularly useful for monitoring large and topographically complex landscapes where traditional field surveys are not logically feasible (Keeley, 2009; Hatala et al., 2010). Although individual forest disturbances have been well studied with remote sensing, e.g.,

disease- or insect-caused tree mortality (Janousek et al., 2019; Pasquarella et al., 2017; Skowronek et al., 2017; Václavík and Meentemeyer, 2012; Vaughn et al., 2018), and wildfire (Chuvieco, et al., 2006; De Santis et al. 2009; Fernandez-Manso et al., 2016; Meng et al., 2017; Quintano et al., 2017), the potential of remote sensing to study wildfire-disease interaction has yet to be well investigated. Several critical issues still remain in the literature.

First, remote detection of disease-caused tree mortality relies on the indicators of tree damage or distinct symptoms (i.e., altered spectral and spatial characteristics), which are different from their healthy counterparts (He et al., 2019b; Lentile et al., 2006; Wulder et al., 2006; Keeley, 2009). However, due to the co-occurrence of multiple disturbances (e.g., wildfire and drought), the damaged trees may present similar spectral and spatial symptoms, introducing a major challenge in remote sensing-based modeling using single sensors. A critical question remains to be answered: Can remote sensing be applied to retrieve disease-caused tree mortality in the regions that other disturbances (e.g., wildfire and drought) also affect the forest?

Second, remote sensing-based forest burn severity estimation relies on the altered spectral responses between pre- and post-fire burned trees (He et al., 2019a). The widely used modeling methods consists of empirical and physical models (Hultquist et al., 2014). Empirical models depend on classical regression or machine learning to link field observed burn severity with remotely sensed spectral bands and spectral indices, such as Normalized Burn Ratio (NBR; López-García and Caselles, 1991), differenced Normalized Burn Ratio (dNBR; Key and Benson, 2006), and relative differenced Normalized Burn Ratio (RdBR; Miller and Thode, 2007). Physical models attempt to

simulate the physical interactions between radiation and burned trees (Chuvieco, et al., 2006De Santis et al., 2009). However, none of the existing models have considered the phenomenon that both fire and non-fire disturbances may co-exist and alter the biophysical and biochemical properties of trees in similar ways (Chen et al., 2015a). The ignorance of such phenomenon is likely to cause significant overestimation in burn severity mapping (Chen et al., 2017). This raises an important question: How to incorporate per-fire forest disturbances in remote sensing modeling to improve the performance of burn severity estimation?

Lastly, current researches on the disease-wildfire interactions are mainly based on field observations for exploring their relationships (Beh et al., 2012; Jenkins et al., 2014; Loehman et al., 2017; Powell et al., 2012; Simler et al., 2018). However, limited field samples are typically not sufficient for an accurate analysis of disturbance-related spatial patterns and their change trajectories. Such information is critical for locating susceptible trees and promoting effective forest management (Kane et al., 2017). While remote sensing approaches and derived products have demonstrated abilities in capturing forest spatiotemporal patterns, their capacity to analyze interacting disturbances was rarely evaluated (Chen and Meentemeyer, 2016).

Dissertation Objectives

An opportunity to study such EID-wildfire interacting disturbances occurred in the Big Sur forest ecoregion of California's central coastal, where a non-native invasive pathogen *Phytophthora ramorum*, also named the sudden oak death, had been involving a multi-year progress since first observed in the mid-1990s (Rizzo et al., 2005). In 2008, a wildfire - Basin Complex Fire - was ignited by a dry lightning storm in late June and

burned 35% (28,383 ha) of our study area. The purpose of this dissertation research is to utilize multi-sensor remote sensing to assess the impact of environmental interacting disturbances of wildfire and disease sudden oak death on forest ecosystem dynamics. More specifically, the three objectives of this study are:

1) to develop a remote sensing model that can capture long-term, spatiotemporal patterns of disease-caused tree mortality in forest landscapes where non-disease disturbances (e.g., fire and drought) coexist;

2) to develop a remote sensing model to map burn severity in forest landscapes, aiming to reduce the effects of tree damage caused by disease-caused disturbance; and

3) to investigate the role of wildfire in changing the spread pattern of forest disease and the effects of disease-wildfire interaction on forest recovery pattern.

Dissertation Structure

This dissertation is organized in a way that each chapter addresses an objective and represents a stand-alone publication-style (or already published) article. This dissertation consists of five parts, including Introduction, Chapter 1, Chapter 2, Chapter 3, and Conclusions. The Introduction chapter provides the research background, objectives, and dissertation structure. Chapter 1 addresses Objective 1, where a new model integrating multi-sensor remote sensing and species distribution modeling is proposed to capture the spatiotemporal patterns of disease-caused tree mortality over one decade. This Chapter has been published in the journal *Remote Sensing of Environment* (***He, Y., Chen, G., Potter, C., Meentemeyer, R.K., 2019b. Integrating multi-sensor remote sensing and species distribution modeling to map the spread of emerging forest***

disease and tree mortality. Remote Sens. Environ. 231, 111238.). Chapter 2 deals with Objective 2, where a Disturbance Weighting Analysis Model (DWAM) was developed to consider the contributions from both fire and disease disturbances in post-fire burn severity modeling. This Chapter has also been published in the journal *Remote Sensing of Environment* (***He, Y., Chen, G., De Santis, A., Roberts, D.A., Zhou, Y., Meentemeyer, R.K., 2019a. A disturbance weighting analysis model (DWAM) for mapping wildfire burn severity in the presence of forest disease. Remote Sens. Environ. 221, 108–121.***). Chapter 3 responds to Objective 3, where the role of wildfire in determining disease transmission and the disease-fire effect on post-fire forest recovery is quantified. This Chapter has been submitted to the journal *Forest Ecology and Management* (***He, Y., Chen, G., Zhao, K., Meentemeyer, R.K., Effects of Wildfire on the Spread of Forest Disease Sudden Oak Death and Post-fire Forest Recovery.***). Chapter 4 includes the conclusions of the dissertation and potential future research.

Chapter 1: Integrating Multi-Sensor Remote Sensing and Species Distribution Modeling to Map the Spread of Emerging Forest Disease and Tree Mortality

Abstract

Forest ecosystems have been increasingly affected by a variety of disturbances, including emerging infectious diseases (EIDs), causing extensive tree mortality in the Western United States. Especially over the past decade, EID outbreaks occurred more frequently and severely in forest landscapes, which have killed large numbers of trees. While tree mortality is observable from remote sensing, its symptom may be associated with both disease and non-disease disturbances (e.g., wildfire and drought). Species distribution modeling is widely used to understand species spatial preferences for certain habitat conditions, which may constrain uncertain remote sensing approaches due to limited spatial and spectral resolution. In this study, we integrated multi-sensor remote sensing and species distribution modeling to map disease-caused tree mortality in a forested area of 80,000 ha from 2005 to 2016. We selected sudden oak death (caused by pathogen *P. ramorum*) as a case study of a rapidly spreading emerging infectious disease, which has killed millions of oak (*Quercus spp.*) and tanoak (*Lithocarpus densiflorus*) in California over the past decades. To balance the needs for fine-scale monitoring of disease distribution patterns and satisfactory coverage at broad scales, our method applied spectral unmixing to extract sub-pixel disease presence using yearly Landsat time series. The results were improved by employing the probability of disease infection generated from a species distribution model. We calibrated and validated the method with image samples from high-spatial-resolution NAIP (National Agriculture Imagery Program), and hyperspectral AVIRIS (Airborne Visible/Infrared Imaging

Spectrometer) sensors, Google Earth® imagery, and field observations. The findings reveal an annual sudden oak death infection rate of 7% from 2005 to 2016, with overall mapping accuracies ranging from 76% to 83%. The integration of multi-sensor remote sensing and species distribution modeling considerably reduced the overestimation of disease effects as compared to the use of remote sensing alone, leading to an average of 26% decrease in detecting disease-affected trees. Such integration strategy proved the effectiveness of mapping long-term, disease-caused tree mortality in forest landscapes that have experienced multiple disturbances.

1.1. Introduction

Forests play a pivotal role in regulating the energy and mass exchange between terrestrial ecosystems and the atmosphere (Likens et al., 1981). However, environmental disturbances, including those caused by emerging infectious diseases (EIDs) of plants, are beginning to impact the biodiversity, structure, and functioning of forest ecosystems in new ways (Anderegg et al., 2013). Especially over the past decade, EID outbreaks occurred more frequently and severely in forest landscapes, which have contributed to unprecedented tree mortality (Asner, 2013; Boyd et al., 2013; Wingfield et al., 2015; Chen and Meentemeyer, 2016).

Remote detection of EID-caused tree mortality can be an efficient and accurate method to scale up field measurements to the landscape scale (Chen et al., 2016; Hultquist et al., 2014; Kelly et al., 2004; Liu et al., 2007). Mapping pathogen-related disturbances allow stakeholders to prioritize management actions at particular locations of concern, often over large areas (e.g., Meentemeyer et al., 2015). Successful detection relies on the fact that infected trees show distinct spectral, spatial and/or temporal

symptoms, which may be related to declines in chlorophyll/water content in foliage, leaf discoloration, defoliation, or treefall gaps [see a review by Chen and Meentemeyer (2016)]. For example, blister rust (caused by pathogen *Cronartium ribicola*) can turn the needles of eastern white pines into yellow then rusty red (Hatala et al., 2010). Oak trees appear to be 'freeze-dried' because of sudden oak death, which is caused by pathogen *Phytophthora ramorum* (Kelly and Meentemeyer, 2002). Today, sudden oak death has reached epidemic levels in many forests of the Pacific U. S. Coast, killing large numbers of oak and tanoak trees. Similar to EID-caused tree mortality mapping, there is a plethora of literature on remote detection of tree mortality, caused by environmental disturbances of drought (Brodrick and Asner, 2017; Byer and Jin, 2017; Paz-Kagan et al., 2017), outbreaks of insects (Bright et al., 2012; Fassnacht et al., 2014; Meddens et al., 2013; Pasquarella et al., 2017; Rullan-Silva et al., 2013), invasive species (Ghulam et al., 2014; Rocchini et al., 2015; Skowronek et al., 2017), and wind (McDowell et al., 2018; Negrón-Juárez et al., 2014). However, studies have rarely investigated how to identify tree mortality relevant to specific causes if multiple disturbances jointly occur in the same region. This is particularly true for areas affected by EIDs. The outbreak of EIDs is typically related to chronic stress spanning years to decades, which possibly overlaps with discrete events, such as severe drought and wildfire, co-occurring in the same region. Damaged trees that are caused by different disturbance types may exhibit similar (i.e., subtle discrepancies in) spectral or spatial symptoms, challenging the use of popular remotely sensed datasets, such as Landsat and MODIS data. While recent high-spatial and high-spectral resolution imagery has demonstrated the potential to uncover the subtle discrepancies to improve disease mapping (e.g., Hatala et al., 2010; Meddens et al.,

2011; Vaughn et al., 2018), these data types remain costly and are scarce in spatial coverage hindering long-term monitoring of EID-caused tree mortality in any particular region of interest.

Species distribution modeling (SDM; a.k.a., environmental niche modeling) has been widely used in ecology and conservation biology to predict the statistical probability of species dispersal patterns over space and time (Elith and Leathwick, 2009). The performance of those modeling approaches depends on the abiotic conditions and the distribution of sampled observations, which are critical for effective model training and validation (Václavík and Meentemeyer, 2009). Despite its popularity, SDM may lead to high uncertainties and spurious results without reliable knowledge of the actual species (e.g., invasive pathogen) range, acquired typically through field surveys (Carneiro et al., 2016). This becomes a critical issue for estimation of EID outbreaks in forests, where the traditional inventory approaches are not logistically feasible to acquire a sufficient number of pathogen distribution samples.

To effectively map EID-caused tree mortality, bridging remote sensing and ecological SDM offers a potential solution. While such an integration strategy has demonstrated to be effective in recent studies of species modeling (e.g., Saatchi et al., 2008; He et al., 2015), remote sensing is typically used to generate land cover and other ecological variables (e.g., NDVI) serving as input of SDM. For EID-caused tree mortality mapping, would it possible to apply SDM to refine remote sensing generated maps? While remote sensing approaches are likely to overestimate disease effects due to high spectral/spatial similarities across the damaged trees by EID and non-EID disturbances, SDM can provide essential knowledge informing the likelihood that certain

disease disturbance may or may not occur at specific locations. This will ultimately reduce uncertainties in remote sensing-based estimation by providing an effective constraint to exclude the regions, where the studied EID has a low likelihood to occur. Integrating remote sensing and species distribution modeling particularly benefits long-term monitoring, where EIDs demonstrate a strong spatial progression pattern.

The main goal of our study was to develop a mapping method that can capture long-term, spatiotemporal patterns of EID-caused tree mortality in forest landscapes. The method integrated multi-senor remote sensing and SDM, and was developed to study sudden oak death, a rapidly spreading EID that has killed millions of trees in California and Oregon since being discovered during the mid-1990s (Rizzo et al., 2002).

1.2. Study area

Our study site (centered at: 36°16' N, 121°44' W) is located in the Big Sur, California ecoregion on the west coast of the United States. It covers an area of about 80,000 ha on the steepest coastal mountains with elevations reaching 1,600 m within 4.5 km of the coast (Fig. 1.1). This region has a Mediterranean-type climate with moderate temperatures, mean monthly temperatures at sea level range from 10–13 °C in the winter months to 16–18 °C in the summer (Davis et al., 2010). Major forest types include mixed oak woodlands consisting of coast live oak (*Quercus agrifolia*), Shreve's oak (*Quercus parvula var. shrevei*), California bay laurel (*Umbellularia californica*), and Pacific madrone (*Arbutus menziesii*), as well as mixed coniferous forests, which are composed primarily of ponderosa pine (*Pinus ponderosa*), sugar pine (*Pinus lambertiana*), Jeffrey pine (*Pinus jeffreyi*), coulter pine (*Pinus coulteri*), and Santa Lucia Fir (*Abies bracteata*). They give way to riverside corridors of redwood/tanoak (*Sequoia*

sempervirens / Notholithocarpus densiflorus) dominated forests at lower elevations (Davis et al., 2010). Current anthropogenic land use is still limited and consists primarily of isolated houses, roads, and trails, which were used primarily for recreation within the study domain.

Sudden oak death (caused by pathogen *P. ramorum*) was first associated with mortality of tanoak (*Lithocarpus densiflorus*) and oak (*Quercus spp.*) in the San Francisco Bay region during the mid-1990s (Rizzo et al., 2002). It was quickly introduced to California and Oregon forests mainly by infested nursery stock (Davidson, 2005; Ivors et al., 2006; Prospero et al., 2007). Following the introduction, sudden oak death reached epidemic levels in many coastal forests and has affected large, but unknown numbers of oak and tanoak trees (Rizzo et al., 2005). Due to the aggressive transmission of the pathogen, 14 states in the U.S. imposed strict regulations for plant materials imported from the west coast, including California and Oregon (Alexander, 2012). Globally, *P. ramorum* was either listed as a regulated species or specified in national forest legislations in 68 countries (Sansford et al., 2008; Hunter et al., 2018). Although sudden oak death is the main disturbance in Big Sur, two other agents – drought and fire, have also affected the forests as major disturbances. For example, the 2012-2015 severe drought in California has led to significant water losses in forest canopies resulting in high tree mortality (Asner et al., 2016). The 2008 Basin Complex Fire, which was ignited by a dry lightning storm burned 28,383 ha within our study area (Potter, 2016).

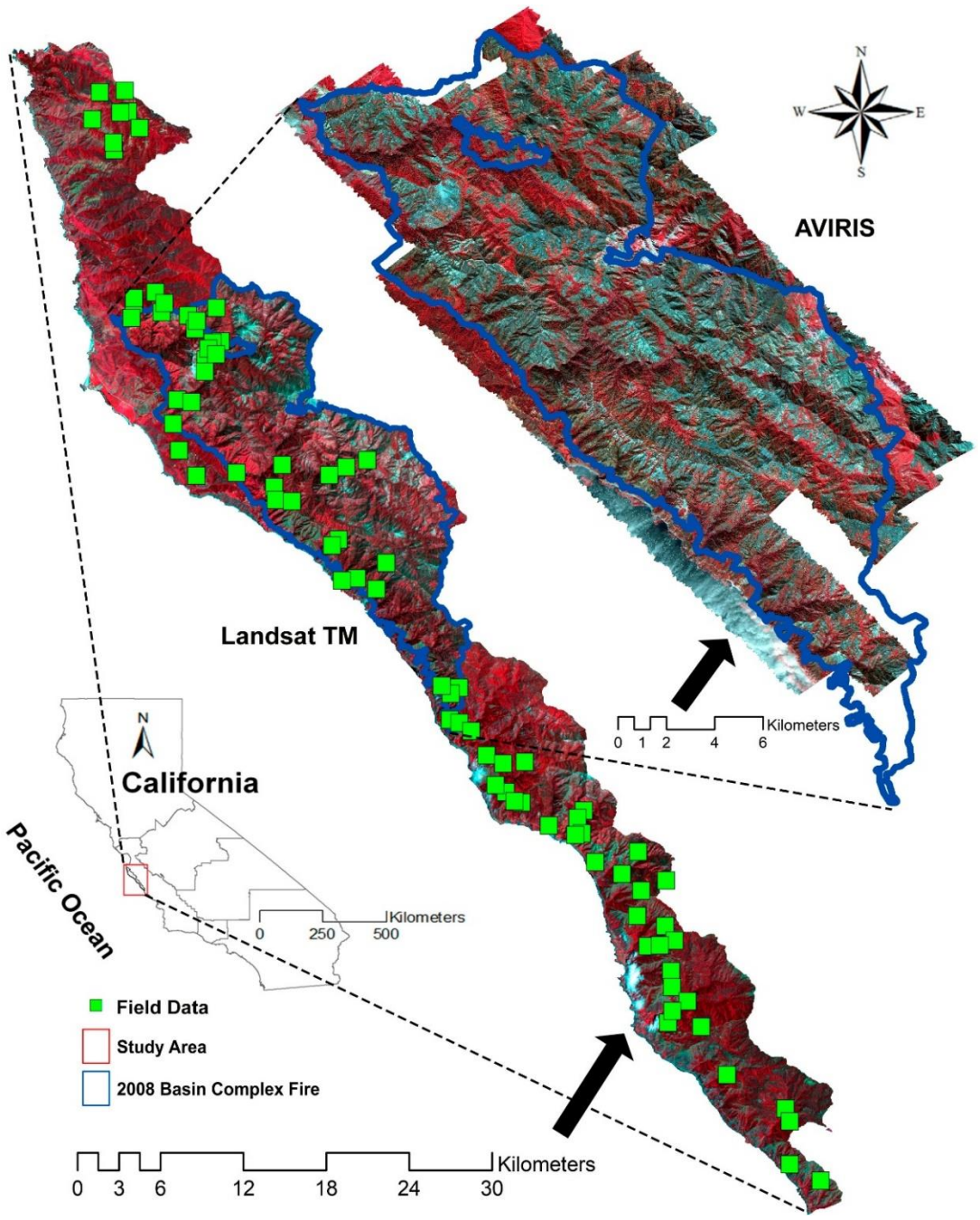

Fig. 1.1 Study area located in the Big Sur ecoregion on the western flank of the Santa Lucia Mountains in California. The Landsat TM (Thematic Mapper) image is from a false color composite using bands 4 (NIR), 3 (Red) and 2 (Green). The AVIRIS (Airborne Visible InfraRed Imaging Spectrometer) image is from a false color composite using bands 51 (NIR), 33 (Red), and 22 (Green).

1.3. Data and preprocessing

1.3.1. Reference data

This study has two groups of reference data: field data and remote sensing data from high-resolution Google Earth (Google, Mountain View, California) image samples and local aerial photos (NAIP, National Agriculture Imagery Program). Specifically, we have established 85 permanent field plots (50×50 m, 0.25 ha) since the summer of 2006 (Meentemeyer et al., 2008b). These plots were designed to follow a stratified random sampling scheme within the mixed oak woodland and redwood-tanoak (acting as the main host species of *P. ramorum*), and have been revisited yearly to monitor sudden oak death infection and its impact on forest structural change (e.g., tree density, tree height, and forest species types). A Panasonic SXBlue real-time differential GPS (Geneq, Montreal) was applied for collecting plot positions, with an average accuracy of 1.0 m or less.

To supplement the limited number of field-derived sudden oak death samples, we extracted diseased and healthy tree plots from Google Earth and aerial photos (i.e., NAIP) via image interpretation. We based our interpretation on the spatial, spectral and temporal symptoms of sudden oak death-caused tree mortality in the study area that are relatively unique as compared to the drought/fire-caused tree mortality. Early in 2002, Kelly and Meentemeyer (2002) discovered the ‘freeze-dried’ characteristic of oak trees as a result of sudden oak death infection, and then used such spectral trait to map the spatial distribution of the disease. Fig. 1.2 shows examples of isolated diseased trees that are surrounded by healthy trees in multi-temporal, high-resolution true color images. Fig. 1.2 demonstrates the symptom changes during the three stages of sudden oak death

progression (Meentemeyer et al., 2008a; Chen et al., 2015a): (i) early-stage (host trees retaining their dried foliage and fine twigs for one year or more), (ii) middle-stage (some older mortality with host trees losing fine crown fuels and surface fuels beginning to accumulate for 1-3 years), and (iii) late-stage (host trees being dead for over 4 years and causing gaps due to trees falling over). Hence, the diseased tree plots change their spatial representation over time, making it distinctive from the other disturbances in high-resolution imagery (Fig 1.2).

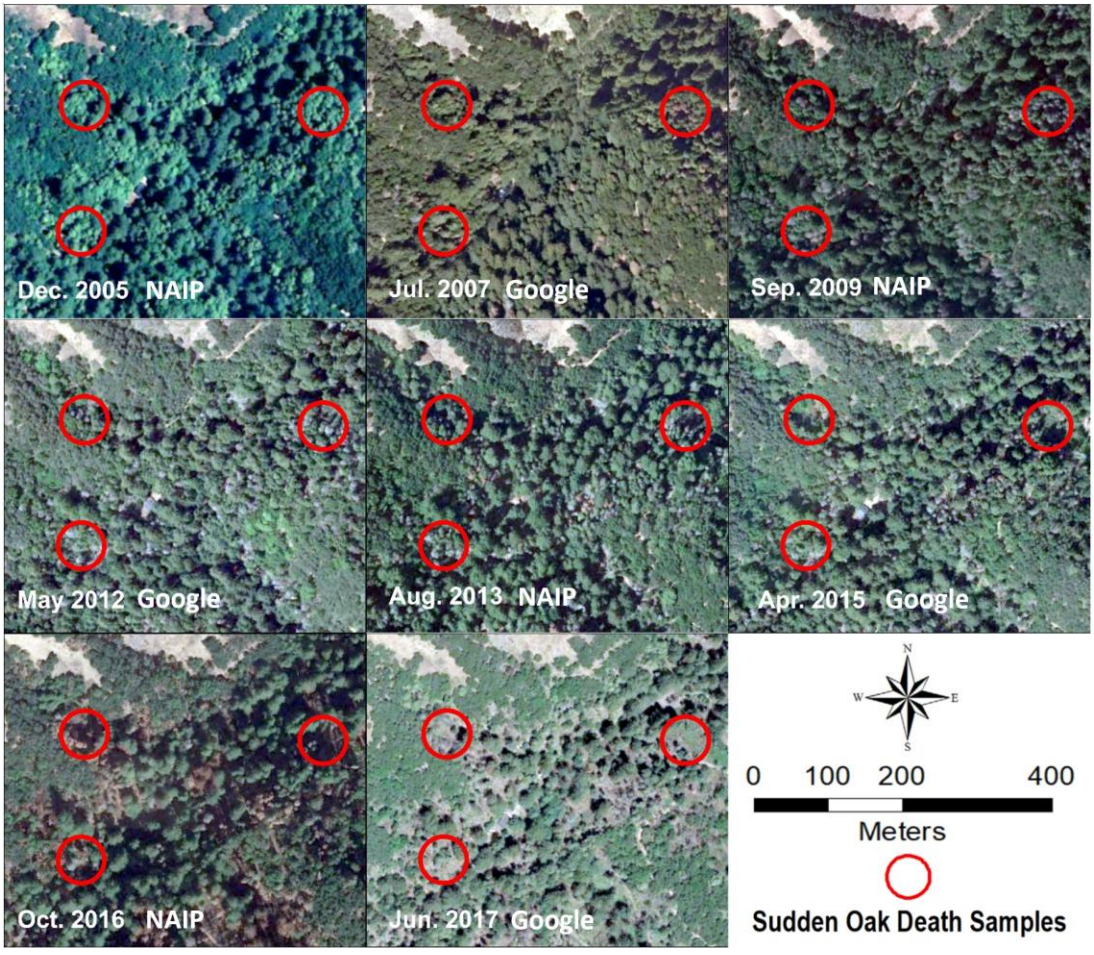

Fig. 1.2 Examples of isolated diseased trees being surrounded by healthy trees and symptom change over time in Google Earth and NAIP high-resolution images.

To quantify the disease's spectral, spatial and temporal patterns as observed in Google Earth and NAIP imagery, we employed two indices. First, tree foliage dramatically changes color from healthy green to brown over one or two years following sudden oak death infection (Liu et al., 2006), and then to gray indicating foliage desiccating and pigments breakdown, leading to 'freeze-dried' appearance (Kelly and Meentemeyer, 2002). We used Red-Green Index (RGI) to capture the variation in canopy color. RGI is a simple ratio between the red and the green band. It was originally developed for detecting mountain pine beetle infestation, which causes color change in pine tree canopies (Coops et al., 2006). Using field data as reference, we calculated RGI for sunlit green, sunlit brown and sunlit gray crowns respectively. As illustrated in Fig. 1.3, unhealthy trees (i.e., sunlit brown and sunlit gray) are distinguishable from the healthy trees (i.e., sunlit green) with RGI locating in different value ranges.

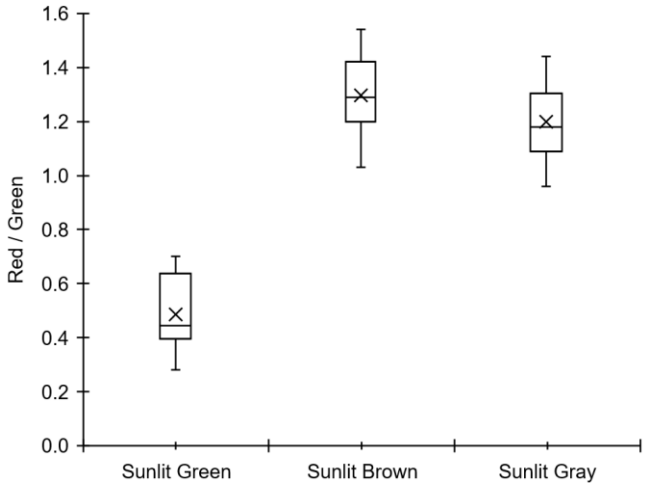

Fig. 1.3 Boxplots showing Red-Green Index (RGI) values (minimum, first quartile, median, mean, third quartile, and maximum) for sampled sunlit green, sunlit brown, and sunlit gray crowns.

Second, sudden oak death-caused tree mortality demonstrates isolated, patchy distribution patterns, which gradually increase the density and reduce distances to each other. (Meentemeyer et al., 2008a). To analyze such patterns, we employed mean proximity index (PRO_MN) to assess the degree of isolation and fragmentation of the corresponding patch type at landscape level over years (McGarigal, 2014; McGarigal and Marks, 1995). In our study, PROX_MN was used as an indicator of fragmentation for sudden oak death-caused tree mortality, with high values indicating low levels of fragmentation and low values indicating high levels of fragmentation (Turner et al. 2001).

$$\text{PROX\_MN} = \frac{\sum_{s=1}^{n} \frac{a_{ijs}}{h_{ijs}^2}}{n} \quad (1)$$

where PROX_MN represents the mean proximity index for focal patch ij, a_{ijs} is the area of patch ijs within a specified neighborhood of patch ij, h_{ijs} is the distance between patch ijs and patch ij, based on patch edge-to-edge distance and computed from cell center to cell center, and n is the total number of patches within the neighborhood. Here, PROX_MN was calculated within a neighborhood using 200 m as search radius. Our assumption is that if field data have suggested sudden oak death occurrence at that location, the neighboring trees with similar RGI values (same value range) were also affected by the disease. The neighborhood size was chosen based on our field experience in sudden oak death identification. Fig. 1.4 shows the trajectory of PROX_MN values over years. We did not find in the literature or in our study area that drought/fire-caused tree mortality demonstrates any specific spatial-temporal patterns over years. For

example, Fig. 1.5 shows the trajectory of PROX_MN values for gray/brown sample areas not affected by the disease, which even indicates a decreasing trend over time.

We used 70% of the field data to estimate the range of RGI values (0.96-1.54), and the range of PROX_MN values (10.20-2509.03) and the slopes of their trend lines (63.05-196.74). The remainder of the field data were used for accuracy assessment. We have achieved an overall accuracy of 92% and a Kappa statistic of 0.84 in sudden oak death extraction from NAIP and Google Earth imagery.

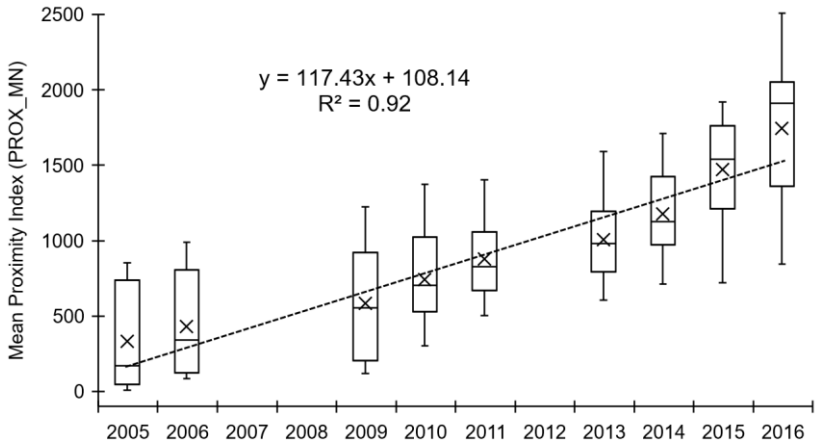

Fig. 1.4 Temporal trajectory of the mean proximity index (PROX_MN) for the dead trees affected by sudden oak death.

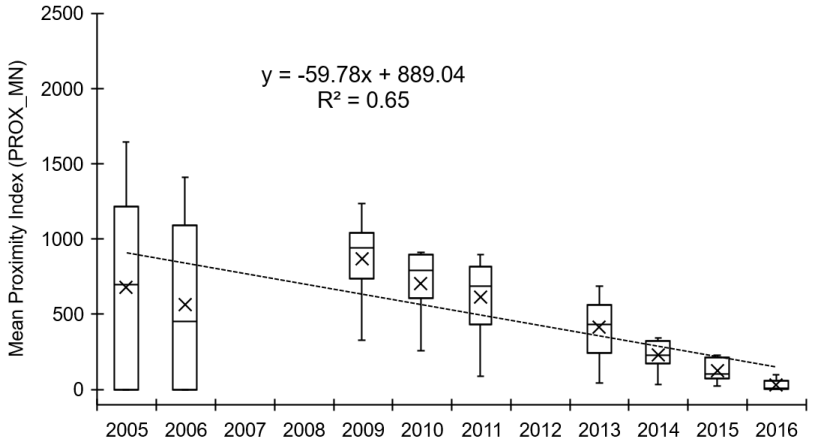

Fig. 1.5 Temporal trajectory of the mean proximity index (PROX_MN) for the dead trees not related to sudden oak death.

Because field plots have unbalanced number of healthy *versus* diseased tree plots due to sudden oak death progression, it may cause a bias in model training. We extracted various numbers of plots each year to balance the number of the two tree classes. We randomly allocated the photo interpretation-derived plots, but also created a buffer to avoid the neighborhood of field plots (100 m in size). The final reference dataset includes 40 diseased and 40 healthy tree plots every year during the 2005-2016 study window. We were aware of the positional errors in NAIP and Google Earth imagery (Potere, 2008; USDA, 2012). Because of the higher accuracy in NAIP data (6 m of true ground at a 95% confidence level, USDA, 2012), we relied more on NAIP to collect annual imagery (2005, 2009, 2010, 2013, 2014, and 2016), which were supplemented by Google Earth (2006, 2011, and 2015). We further compared our field plots (with GPS-measured accurate positions) with the targets identified on NAIP and Google Earth imagery. The errors were noticeably smaller than 30 m, which did not have a major effect on the modeling accuracy since our model was built at the 30 m resolution using Landsat data as the major input.

1.3.2. AVIRIS data

We collected AVIRIS (Airborne Visible/Infrared Imaging Spectrometer) data on September 24, 2008. AVIRIS is an airborne hyperspectral sensor developed and operated by NASA's Jet Propulsion Laboratory (JPL) flown on ER-2 and Twin Otter aircrafts mainly over the United States. The AVIRIS sensor consists of 224 contiguous spectral bands in the range of ~360 nm to ~2500 nm with an average bandwidth of 10 nm (Clark et al., 2002). The cloud-free AVIRIS spectral radiance image mosaic covered the northern part of our study area (27,925 ha), with a spatial resolution of 3 m. To mitigate the topographic effects in the mountainous regions, the topographic correction method recently developed by He et al. (2015) was applied on the basis of slope and aspect provided along with the AVIRIS flight data, which was processed using a 30 m resolution digital elevation model (DEM) derived from the data collected by Advanced Spaceborne Thermal Emission and Reflection Radiometer (ASTER) as part of the Global Digital Elevation Model Version 2 (GDEM V2) project (ASTER GDEM Validation Team, 2011). Finally, the AVIRIS image mosaic was converted to surface reflectance bands using the 5th version of MODerate resolution atmospheric TRANsmission (MODTRAN5) as described by Berk et al. (2006).

1.3.3. Landsat imagery

To retrieve the spatial and temporal patterns of sudden oak death progression annually from 2005 to 2016, we downloaded a total of eight Landsat-5 TM (Thematic Mapper) and five Landsat-8 OLI (Operational Land Imager) image scenes covering our study area (path: 43, row: 35) via the U.S. Geological Survey (USGS) Earth Resources Observation and Science (EROS) Center's Science Processing Architecture (ESPA)

interface (https://espa.cr.usgs.gov). We did not use Landsat data from 2012, due to Landsat 5's mechanical failures and Landsat 7's Scan Line Corrector (SLC) failure. Although there are wavelength differences between sensors, we used the six bands that have been consistently acquired by all the sensors, including blue, green, red, NIR, SWIR-1, and SWIR-2 (NASA, 2018). All the images were acquired in the growing season (April-June, Table 1.1). Because some of the areas were covered by clouds in 2006 and 2013, we generated a cloud-free mosaic for each of the two years through compositing two image scenes acquired in the same month. During the process, cloud pixels were simply replaced by the cloud-free pixels of the same locations. Because the images used for merging were from the same months over the same region, we visually interpreted the images and found low spectral variation over the same ground objects between different dates. The high quality radiometric correction completed by USGS also ensured the minimized impact of our merging process. In our study, we directly used the Landsat Surface Reflectance level-2 science products, which have been geometrically, radiometrically, and topographically corrected by USGS before being made available online. Please refer to Landsat 4-7 Surface Reflectance Product Guide (USGS, 2018a) and Landsat 8 surface reflectance product guide (USGS, 2018b) for details about Landsat surface reflectance products.

Table 1.1 Acquired dates for time-series Landsat imagery.

	2005	2006	2007	2008	2009	2010	2011	2013	2014	2015	2016
April							4th	16th +25th	28th	15th	17th
May		8th+15th		13th	16th	3rd					
June	6th		12th								

1.3.4. NAIP imagery

NAIP (Airborne Visible/Infrared Imaging Spectrometer) imagery was acquired in 2005 at a 1.0 m resolution (a.k.a., ground sample distance - GSD) with a horizontal accuracy that matches within six meters of photo-identifiable ground control points. It was a three-band (Red, Green and Blue, or RGB) image mosaic with high quality data covering a portion of our study area. The data were downloaded from the U.S. Department of Agriculture (USDA) Farm Service Agency with free access (https://datagateway.nrcs.usda.gov/). The data were geometrically and radiometrically corrected by USDA.

1.3.5. Environmental variables

We used two groups of environmental variables known to affect the transmission of *P. ramorum* (Meentemeyer et al., 2008a): climate (i.e., precipitation, temperature, and relative humility) and topographical variables [i.e., elevation, slope, solar insolation index (SII), and topographic wetness index (TWI)] (Table 1.2). For climate, we calculated each variable using the monthly mean data during the disease's general reproductive season from December to May prior to each state transition over a period of 10 years (2007 to 2016). We selected this time period mainly due to the proven correlation between pathogen progressions with local climatic conditions (Meentemeyer et al., 2008a). This time period was selected in order to model the response of disease to annual patterns of climate, not individual weather events (Sturrock et al., 2011). The employed climate data were part of a broader-scale database Daymet (https://daymet.ornl.gov), at a 1×1 km resolution over the conterminous United States (Thornton et al., 2018). For topographical conditions, we calculated four variables from a

30 m resolution DEM, derived from the ASTER's GDEM V2 product, including elevation, slope, SII, and TWI. We calculated SII for each 30 m cell as the potential mean solar radiation in the rainy season using the cosine of illumination angle on slope equation (Dubayah, 1994). We further calculated TWI as the natural log of the ratio between the upslope contributing drainage area and the slope gradient of a grid cell to quantify topographic control on hydrological processes (Moore et al., 1991).

Table 1.2 Description of the evaluated environmental factors.

Factor type	Factor name	Description
Climate	Precipitation	Monthly (December-May) mean precipitation of 10 years (2007 to 2016)
	Temperature	Monthly (December-May) mean maximum temperature of 10 years (2007 to 2016)
	RH	Monthly (December-May) mean relative humidity of 10 years (2007 to 2016)
Topography	Elevation	Elevation
	Slop	Slope
	TWI	Topographic wetness index
	SII	Solar insolation index

1.4. Methods

Our research framework has two major steps: (i) model development, and (ii) model application to multi-temporal disease distribution mapping. Generally, Step (i) was conducted for 2005, the beginning year of the studied time window 2005-2016 (see flowchart of step 1 in Fig. 1.6). To balance the needs for fine-scale monitoring of disease distribution and satisfactory coverage at broad scales, we applied spectral unmixing to extract sub-pixel disease presence in Landsat imagery, and derived an NPV (non-photosynthetic vegetation) fraction map to simulate tree mortality. The AVIRIS image mosaic was used to extract endmembers to facilitate spectral unmixing. We further

developed a species distribution model and subsequently a probability map for assessing the probability of sudden oak death infection. We employed the 2005 reference data and the NAIP image of the same year to generate a high-resolution disease map for calibrating and validating the species distribution model. The probability map was compared with the reference disease presence/absence for determining a probability threshold, by which disease distribution was mapped for 2005. In Step (ii), an NPV fraction and a probability map were generated for each of the succeeding years (2006-2016). The annual disease-caused tree mortality maps were derived by applying the probability threshold (Step i) to all the probability and the corresponding year of NPV fraction maps. Fig. 1.6 shows the main components in model development and application. Please refer to the following subsections for detail and explanation. The annual disease-caused tree mortality maps were derived by applying the probability threshold (Step i) to all the probability and the corresponding year of NPV fraction maps. The accuracy of the tree mortality maps was individually evaluated using the annual reference data (see Section 1.3.1).

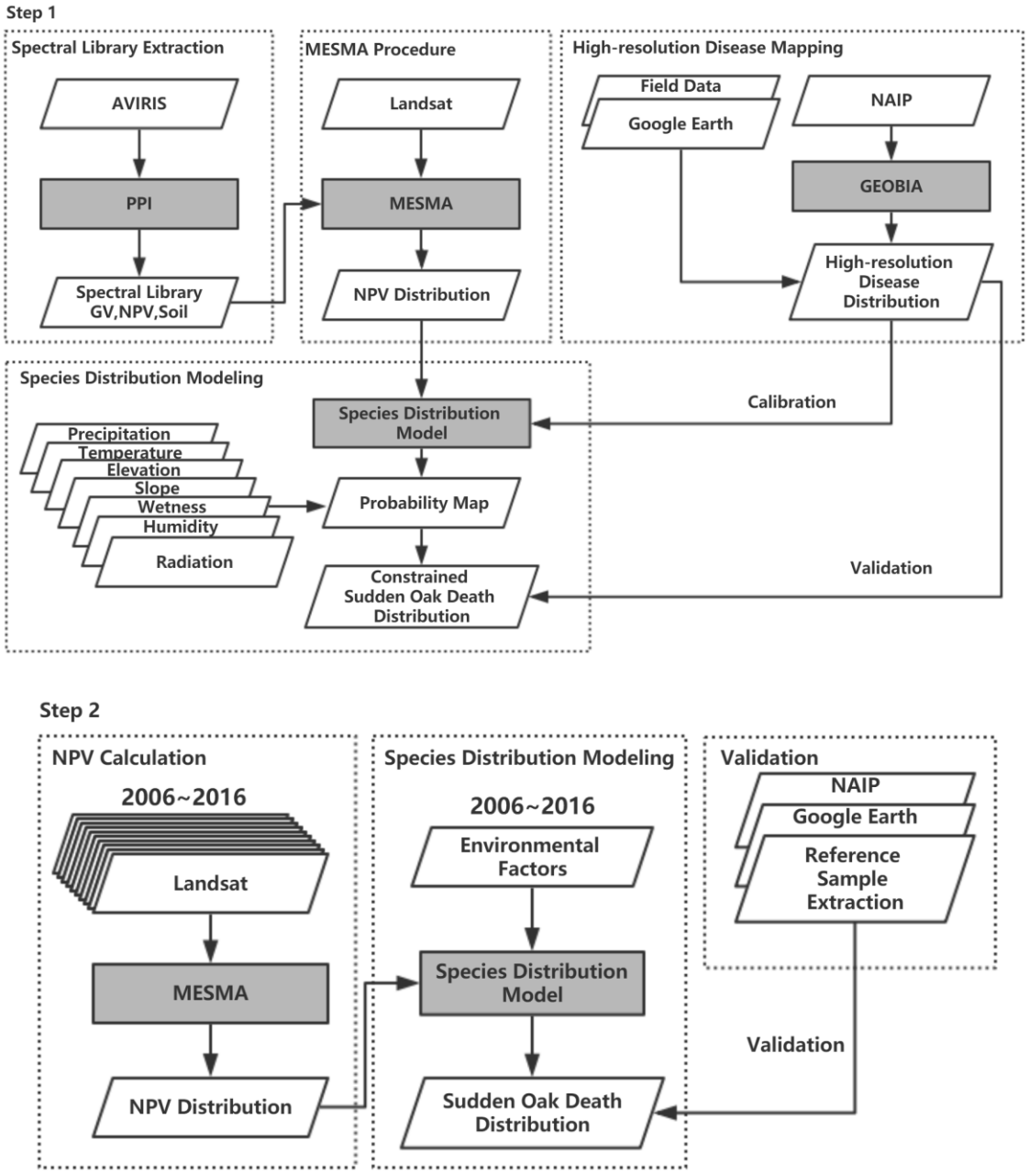

Fig. 1.6 Detailed working flow for model development (Step1) and annual disease-caused tree mortality mapping (Step 2).

1.4.1. Spectral library extraction

We constructed a spectral library to include the spectra of four endmembers in our study area: green vegetation (GV), non-photosynthetic vegetation (NPV), soil, and

shade. We intended to use GV to represent healthy trees. Here, we tried to build an NPV spectral library biased to sudden oak death, although we expected an overestimation of NPV-derived diseased trees because other disturbances (e.g., drought) may have resulted in similar spectra. Due to no pre-existing library including the spectral signatures from sudden oak death-impacted forests, we extracted image endmembers from the hyperspectral AVIRIS data acquired over the same region. Compared to field radiometry surveys, such method was cost-effective, allowing us to efficiently collect a large number of reflectance values associated with disease infection. Using the AVIRIS data, we applied the Pixel Purity Index (PPI) algorithm to identify a large number of potential endmember pixels with unique spectral signatures. The classic PPI is an iterative process, in which every pixel is repeatedly projected onto a random vector selected through the n-dimensional scatter plot (n=224 in our study); and pixels are considered pure if they constantly fall into the tails of the calculated histograms. The threshold for defining histogram tails affected the number of the endmember pixels identified by PPI. After an initial assessment, we used the threshold value 5 to extract 200 endmember candidate pixels.

To select the most appropriate endmembers for our study, we first applied sub-meter Google Earth WorldView-1 images (observation dates in the similar time window as that of AVIRIS data acquisition) as a reference to reduce the number of endmember pixels to 47: 17 (GV), 13 (NPV), 14 (soil), and 3 (shade). To further refine the result, we used the following three metrics.

1) Endmember Average RMSE (root mean squared error) (EAR): EAR was used to select the most representative endmember for each land cover class. It was calculated

for each endmember by averaging the RMSE of the set of models that used the endmember to unmix the spectra belonging to the same land cover class (Roberts et al., 2003).

$$\mathrm{EAR}_i = \frac{\sum_{j=1}^{N} \mathrm{RMSE}_{i,j}}{n-1} \tag{2}$$

where *i* is an endmember, *j* is the modeled spectrum, *N* is the number of endmembers, and *n* is the number of modeled spectrum. The term *n*-1 corrected for a zero RMSE resulting from an endmember itself. EAR was used to evaluate the ability of each endmember to model the spectra within its own class. Endmembers possessing a lower EAR model spectrum within their land cover class were better than endmembers with a higher EAR. The minimum EAR endmember should be the most representative of its modeled class.

2) Minimum Average Spectral Angle (MASA): MASA within a class was calculated as the average spectral angle between the reference spectrum (candidate model) and all other spectra within the same class. The best MASA candidate was selected as the one that produced the lowest average spectral angle (Dennison et al., 2004).

$$\mathrm{MASA}_i = \frac{\sum_{j=1}^{N} \theta_{i,j}}{n-1} \tag{3}$$

$$\theta = \cos^{-1} \frac{\sum_{\lambda=1}^{M} \rho_\lambda \rho'_\lambda}{L_\rho L_{\rho'}} \tag{4}$$

$$L_{\rho'} = \sqrt{\sum_{\lambda=1}^{M} \rho_\lambda^2} \tag{5}$$

where ρ_λ is the reflectance of an endmember, ρ'_λ is the reflectance of a modeled spectrum, L_ρ is the length of the endmember vector, and $L_{\rho'}$ is the length of the modeled spectrum vector. MASA was similar to EAR in that it was designed to select spectra with the best average fit within a class, while differing from EAR in that the measure of fit used was the spectra angle instead of RMSE.

3) Count-based Endmember Selection (CoB): CoB was used to select optimal endmembers as those members of a library that modeled the greatest number of spectra within their class, while assessing whether these candidate models met fraction, RMSE and residual constraints when unmixing any other spectrum in the library (Roberts et al., 2003). CoB used the MESMA concept to select endmembers based on the number of library spectra, determining the number of spectra modeled by an endmember within the endmember's class (InCoB) and outside of endmember's class (OutCoB). The optimum model had the highest InCoB and lowest OutCoB.

The processing used the tool – Visualization and Image Processing for Environmental Research (VIPER; Roberts et al., 2007), which generated the final spectral library (including 6 spectra for GV, 5 spectra for NPV, 6 spectra for soil, and 1 spectrum for shade) and the corresponding fractions.

1.4.2. MESMA procedure

Using the constructed spectral library, we applied spectral unmixing to decompose each of the Landsat pixels acquired in 2005 into three components: GV, NPV, and soil. Spectral unmixing was implemented by the classic Multiple Endmember Spectral Mixture Analysis (MESMA) algorithm, which considers spectral variability allowing the number and type of endmembers to vary on a per-pixel basis (Roberts et al.,

1998). The criteria used to determine the best-fit models included endmember fractions, maximum shade fraction, and RMSE. We chose the following thresholds: −0.05 and 1.05 for minimum and maximum allowable fraction values, respectively; 0.8 for maximum allowable shade fraction value; and 0.025 for maximum allowable RMSE. Those thresholds were initially determined from the literature (Roberts et al., 1998), and adjusted through our tests, in which we evaluated all the reasonable endmember combinations and selected the best-fit model. When multiple models met these criteria, the model with the lowest RMSE was chosen. Finally, shade normalization was performed to remove shade fraction, redistributing this fraction proportionally among all other non-shade endmembers (Roberts et al., 2007). We employed the VIPER package to complete the MESMA procedures (Roberts et al., 2007). Given the fact that our study focused on forests, we excluded the soil, and shrub/grass components from all NPV images (2005-2016) using the 2005 NAIP-derived classification result (see Section 1.4.3).

1.4.3. High-resolution disease mapping

We generated a high-resolution disease distribution map for 2005, the beginning year of the study time window. The map was for SDM calibration and validation (Section 1.4.4), mainly because the accuracy of SDM depends on the number and quality of species reference samples (Carneiro et al., 2016). In our study, field-measured data were limited, which may not provide a reliable knowledge of sudden oak death distribution. Here, we integrated the 1.0 m resolution NAIP image mosaic and the reference data acquired in 2005 to generate a high-resolution tree mortality map. This

map was later used to extract a large number of samples of sudden oak death distribution for reliable SDM calibration and validation (Section 1.4.4).

To generate the map, we applied a geographic object-based Image Analysis (GEOBIA) framework following Chen et al. (2012). Compared to the classic pixel-based approach, GEOBIA uses image-objects (i.e., pixel clusters) as the basic study units to reduce errors caused by spectral variation within each geographic object (e.g., individual trees containing sunlit and shaded crowns; Chen et al., 2015a). Our framework has two components: image segmentation and object-based classification, both of which were completed in the eCognition Developer 9.0 environment (Trimble, Sunnyvale, USA).

Image segmentation was conducted on the NAIP image mosaic using the eCognition's classic multiresolution segmentation algorithm. A crucial issue involved in segmentation is defining an appropriate Mean Object Size (MOS), or spatial scale of analysis. A large MOS may cause under-segmentation where an image-object contains more than one land-cover class. However, a very small MOS may introduce biases where an image-object may only contain sunlit or shaded canopies resulting from the complex sun-tree-sensor geometry. We followed the recommendations by Chen et al. (2017), and the value 30 for MOS was chosen to accurately capture relatively small, homogenous land-cover patches, where the majority of trees within image-objects were either dead or healthy. In addition to MOS, the default value of 0.1 was used for the shape parameter, while the compactness parameter was set at 0.8 to obtain relatively smooth forest object boundaries.

Object-based classification used the segmentation-derived image-objects, instead of pixels, as the basic mapping units. To extract spectral features for classification, we

followed Chen et al. (2017), who successfully used three groups of features – spectral (mean), texture (standard deviation), and geometry (compactness, length/width ratio, roundness, and shape index) – to map sudden oak death-caused tree mortality. Compared to many other causes of mortality, sudden oak death has resulted in uniquely spatial and spectral appearances in tree crowns (Section 1.3.1). We expected to use these features to capture the unique traits of diseased trees. Here, we categorized the image into three classes: (i) healthy forest, (ii) diseased forest, and (iii) others. This step was accomplished by applying the eCognition's nearest neighbor algorithm, a supervised classification approach. Half of the 2005 reference samples for each land-cover class were used for training, while the remaining samples in the same year were applied for validation.

1.4.4. Species distribution modeling (SDM)

We developed a generalized linear model (GLM) to analyze the degree to which ecological conditions influenced the probability of sudden oak death infection. GLM is an extension of ordinary multiple regression that allows for modeling non-normal response variables, which has been used for modeling disease risks (e.g. Meentemeyer et al., 2008a). Here, we modeled the infection probability of sudden oak death as a function of seven environmental variables (i.e., precipitation, relative humidity, temperature, elevation, slope, SII, and TWI) by following the recommendations of Meentemeyer et al. (2008a; 2008b), who studied sudden oak death in the same region. We used the logit link function in GLM, which is synonymous with logistic regression employing a maximum likelihood parameter optimization technique to model the log odds of a binary response variable (Franklin, 1995). The logit transformation of the probability (p_i) that a

susceptible plot *i* (equivalent of the area of a Landsat pixel) becomes invaded is described as:

$$\mathrm{Y}_{\mathrm{infection}} = \mathrm{logit}(p_i) = \log\frac{p_i}{1-p_i} = \beta_0 + \sum_{j=1}^{8}\beta_j x_j \quad (6)$$

where β_0 and β_i are the regression coefficients, and x_j is one of the eight environmental variables. Meentemeyer et al. (2008a) discovered a rapid decline of *P. ramorum* invasion probability as the distance to the previous year of infection (i.e., sources of inoculum) increases. Particularly when the distance is longer than 1 km, the probability that a susceptible plot may be invaded is very low. In this study, we applied a fixed dispersal kernel (1 km in Euclidean distance) to constrain the maximum infection distance for each year.

To reduce multicollinearity among the independent variables, the Pearson's linear correlation coefficients were calculated for all the variables. Then, we applied the variable reduction method as described in Chen et al. (2015b). That is, each independent variable was evaluated and retained under two rules: (1) its correlation with any other independent variable should be lower than 0.7; or (2) if its correlation with another one or several independent variables is higher than 0.7, the variable should have the highest correlation value with the dependent variable. After discarding redundant independent environmental variables/factors, we applied regression analysis and assessed model's adjusted R^2, RMSE (root mean square error) and AIC (Akaike information criterion) values in the statistical environment R package (R Core Team, 2017, Vienna, Austria). For model calibration, we extracted 300 sample points (150 diseased and 150 healthy samples to ensure a balanced representation of trees affected and not affected by sudden

oak death) from the previously generated high-resolution tree mortality map (Section 1.4.3). We used a stratified random sampling strategy to collect samples from diseased and healthy tree classes, respectively. To ensure the quality of the samples, we manually checked all the samples following the same image interpretation approach as described in the reference data section (Section 1.3.1). If the sample did not appear to be affected by the disease, we selected a new sample in its neighborhood.

We further compared the probability derived from the SDM (Eq. 6) with the NPV fraction (Section 1.4.2) at the sample locations. We used the reference disease presence/absence data to determine the best probability threshold, with results reaching the maximum kappa statistic value (Freeman and Moisen, 2008), i.e., a Landsat pixel area was deemed to be affected by sudden oak death if its probability value was higher than the threshold. We also applied the reference data to conduct an accuracy assessment using confusion matrix to calculate True Skill Statistic (TSS), a measure reflecting true ecological phenomena in presence-absence models (Allouche et al., 2006). Specifically, for the binary classification, the confusion matrix records the number of True Positive (TP), False Positive (FP), False Negative (FN) and True Negative (TN) cases predicted by the model (Table 1.3). Sensitivity is the probability that the model correctly classifies a presence (Eq. 7). Specificity is the probability that the model correctly classifies an absence (Eq. 8). TSS equals the difference between the sum of sensitivity and specificity and constant one (Eq. 9).

Table 1.3 A confusion matrix to evaluate the result of a presence-absence (binary) model.

User Class	Reference Class	
	Presence	Absence
Presence	True Positive (TP)	False Positive (FP)
Absence	False Negative (FN)	True Negative (TN)

$$\text{Sensitivity} = \frac{TP}{TP + FN} \tag{7}$$

$$\text{Specificity} = \frac{TN}{FP + TN} \tag{8}$$

$$TSS = \frac{TP}{TP + FN} + \frac{TN}{FP + TN} - 1 \tag{9}$$

1.4.5. Annual disease-caused tree mortality mapping

We applied the spectral unmixing MESMA model to each of the Landsat images from 2006 to 2016, which produced annual NPV fraction maps. Meanwhile, the SDM was employed to produce yearly probability maps of sudden oak death infection (see Step 2 in Fig. 1.6). We overlapped the two types of maps of the corresponding year. The probability threshold (Section 1.4.4) was used to determine whether an NPV-identified pixel was affected by sudden oak death or not. We considered that a 30-m pixel area is affected by the disease if a disease reference sample is found in the area. This is based on the nature of SDM, which only considers infection and non-infection for each pixel area. Consequently, a total of 10 maps were produced to show annual sudden oak death progression from 2006 to 2016. The final mapped results were assessed using the

reference data that were collected annually (see Section 1.3.1), with confusion matrices, coverall accuracies, and kappa statistics calculated for accuracy assessment.

1.5. Results

1.5.1. Endmembers and fraction images

The spectral reflectance for the extracted 6 GV, 5 NPV, and 6 soil endmembers are presented in Fig. 1.7. Overall, the GV endmembers revealed higher intra-class variation than the NPV and soil endmembers. This was mainly because trees in the study area were comprised of a variety of species types, including mixed oak woodlands and coniferous forests. Compared to healthy trees, dead trees and soil were relatively homogeneous in terms of spectral signatures. Especially for the dead trees, their spectral reflectance values were extremely low in the near-infrared portion of the spectrum (760–900 nm) and high in the shortwave infrared portion (1550–1750 nm), making NPV distinguishable from GV and soil. Uncertainties occurred mainly between some GV and soil endmembers. There were barren lands in the study area, although forest floor was often made up of soil, decaying logs/leaves, and grass/shrubs.

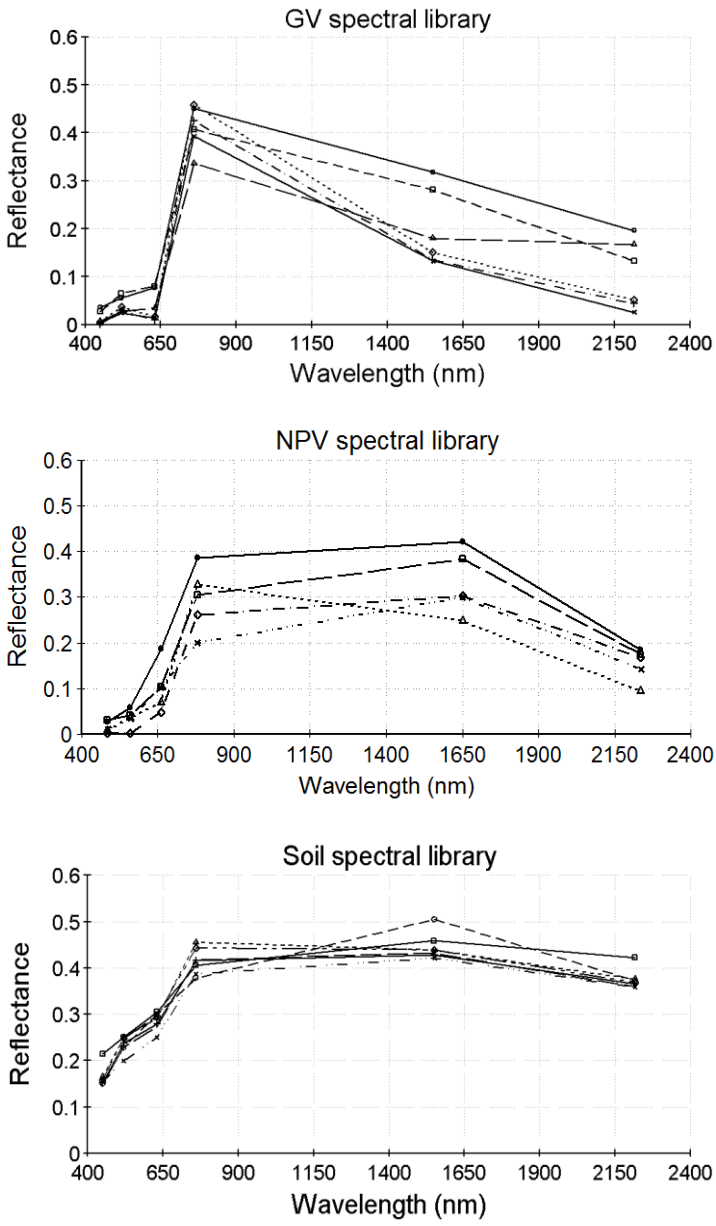

Fig. 1.7 The extracted spectra for green vegetation (GV), non-photosynthetic vegetation (NPV), and soil in our study area.

The fraction maps corresponding to the three components of GV, NPV and soil for year 2005 are shown in Fig. 1.8. Live trees covered much of the study in 2005, as evidenced by the high GV fraction values. High NPV values mainly occurred on the west coast, which is consistent with findings by Meentemeyer et al. (2008b), who used 0.33 m

resolution aerial photos to manually digitize sudden oak death-caused tree mortality over the same area.

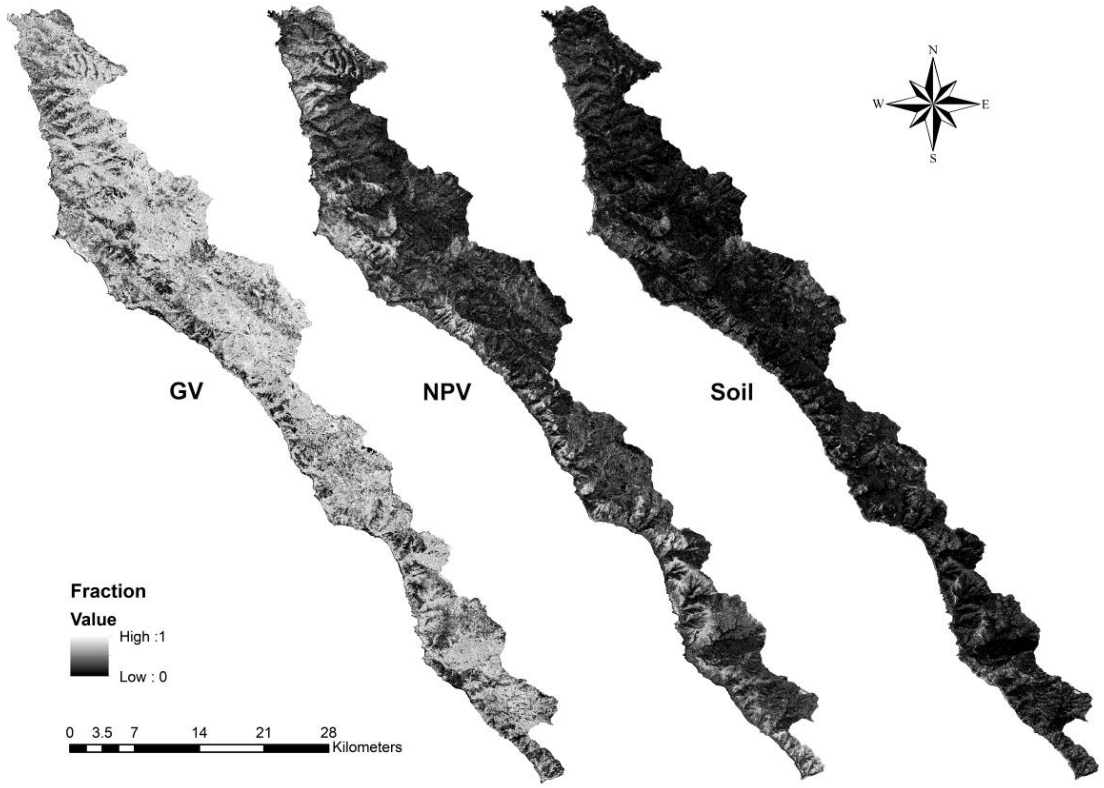

Fig. 1.8 Fraction maps of green vegetation (GV), non-photosynthetic vegetation (NPV), and soil for year 2005, where grey tones represent values from low (black) to high (light).

1.5.2. Fine-resolution tree mortality map

The overall accuracy of the classification result using the 2005 NAIP imagery and the object-based framework was 88.33%, with a Kappa statistic of 0.82. As presented in Table 1.4, others achieved better performance. Compared to the non-forest landscapes, forest horizontal and vertical structure was of higher complexity and heterogeneity, resulting in a higher spectral variation. Compared to the healthy forests, diseased forests were more difficult to map showing relatively lower user's and

producer's accuracies (Table 1.4). Uncertainties mainly occurred in the land-cover transitional zones, where dead trees were interspersed with their healthy counterparts or soil. Because sudden oak death had a non-random, highly-localized distribution pattern (Meentemeyer et al., 2011), some small patches of diseased trees were closely surrounded by healthy forests [see (a) in Fig. 1.9]. In addition, trees affected by the disease changed colors progressively over years, which made it difficult to accurately extract all the diseased trees. For example, some may be at the non-visible early stage of infection. In the transitional zones, we also observed a mixture of soil, and sparsely distributed vegetation within single image-objects [see (b) in Fig. 1.9]. The averaged reflectance from those objects was similar to that of a diseased forest object (Chen et al., 2017). Although the mapping was challenged by a small portion of transitional zones, the extracted 300 samples (Section 1.4.3) were all manually checked to ensure the quality for reliable SDM calibration and validation.

Table 1.4 Confusion matrix for the disease mapping result.

User Class	Reference Class				
	Healthy Forest	Diseased Forest	Others	Total	Producer's Accuracy (%)
Healthy Forest	35	4	1	40	87.50
Diseased Forest	3	34	2	39	87.17
Others	2	2	37	41	90.25
Total	40	40	40	120	
User's Accuracy (%)	87.50	85.00	92.50		

Overall accuracy = 88.33%; Kappa statistic = 0.82.

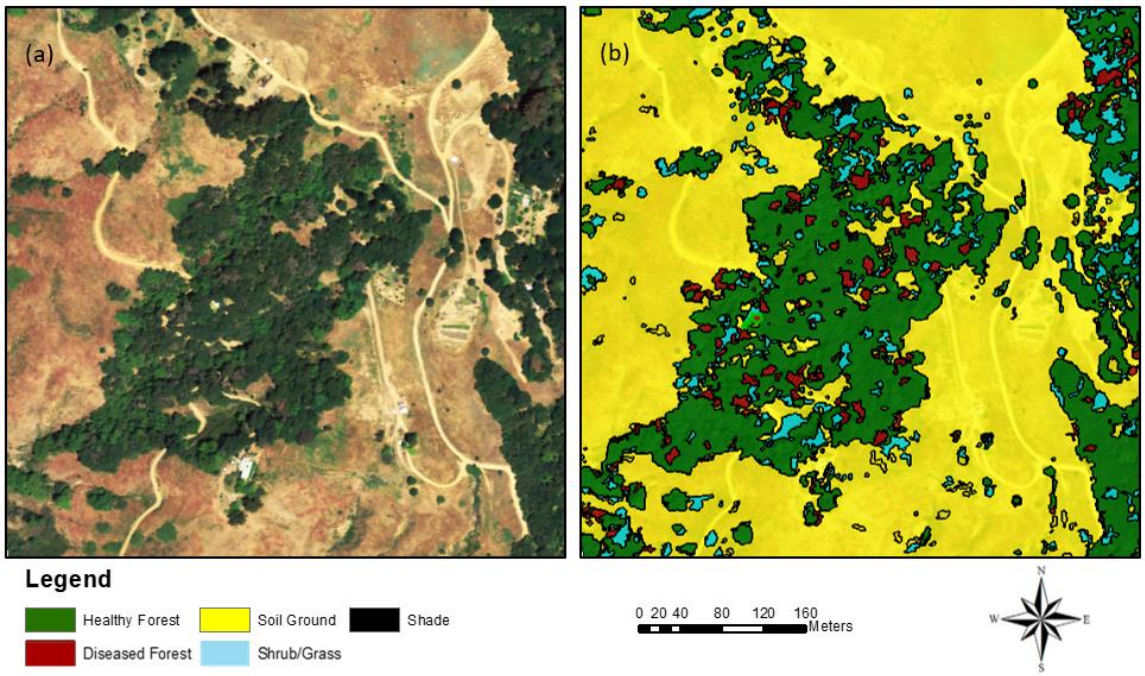

Fig. 1.9 (a) True color sample NAIP image in the Big Sur, CA study region, and (b) corresponding classification with image-object boundaries.

1.5.3. Species distribution modeling (SDM)

Three environmental variables were selected in the SDM, including precipitation, temperature, and elevation (Eq. 6). These variables together explained 36 percent of the variation (adjusted R^2: 0.36) of the probability of sudden oak death infection. The TSS value 0.78 for our SDM was considered satisfactory following the suggestion by Shirk et al., (2018), in which multiple SDM types (including ours) were comprehensively compared for modeling the spread of white pine blister rust in the Western U.S. Their acceptable TSS values were located in the range between 0.71 and 0.84. We found increased probability with the increase of maximum temperature, and precipitation; however, probability was negatively correlated with elevation. Our findings of significant variables are similar to those in an earlier study, where 2003-2005 field measurements were used in species distribution modeling for predicting the probability of sudden oak death invasion (Meentemeyer et al., 2008a; Meentemeyer et al., 2008b). Using calibration data further allowed us to determine the best probability threshold 0.62. Hence, a Landsat pixel was deemed sudden oak death-impacted if its probability value was equal to or higher than 0.62.

$$Y_{Infection} = -8.4606 + 0.0434 \times Precipitation + 0.3290 \times Temperature - 0.0046 \times Elevation \quad (10)$$

where $Y_{Infection}$ represents the logit transformation of the probability (p_i) that a susceptible plot becomes invaded (see equation 6)

1.5.4. Annual maps of disease-caused tree mortality

Following the application of the proposed mapping method, the long-term sudden oak death-caused tree mortality maps achieved overall accuracies between 0.7 and 0.9, with Kappa statistics ranging from ~0.5 to ~0.7 [see (a) in Fig. 1.10]. The mapping

accuracies for years 2005, 2013, 2014, and 2016 were higher than 80%, while relatively inferior performance (75%-80%) was obtained in years 2006, 2009, 2010, 2011 and 2015 [see (a) in Fig. 1.10].

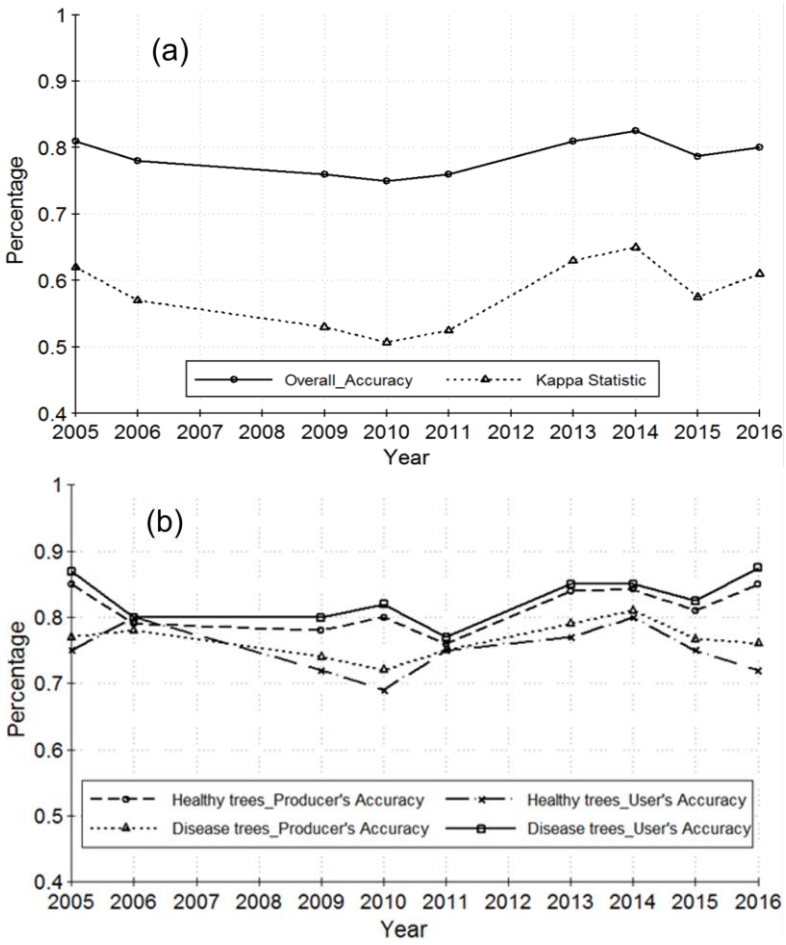

Fig. 1.10 Mapping accuracies (producer accuracy, user accuracy, overall accuracy, and Kappa statistic) in years 2005, 2006, 2009, 2010, 2011, 2013, 2014, 2015 and 2016. See methods of accuracy assessment in Section 1.4.5.

We applied the developed SDM to the entire study area and generated a probability map of sudden oak death infection (Fig. 1.11). When it was overlaid with field plots, we found that potential habitat suitability with high probability was significantly greater (p<0.05) in the invaded plots. All the 11 tree mortality maps (2015-

2016) are included in Fig. 1.12, which shows annual sudden oak death infection in the study area. Those maps illustrate a spatial progression pattern of disease mainly from the west coast to the northeast. The spatial coverage of sudden oak death-caused tree mortality rose rapidly from 1,584 ha in 2005 to 3,178 ha in 2016, a 2-time increase over a decade, at an annual infection rate of 7%. Such an aggressive progression pattern is consistent with the field findings discussed in the literature (e.g., Rizzo et al., 2005; Cunniffe et al., 2016).

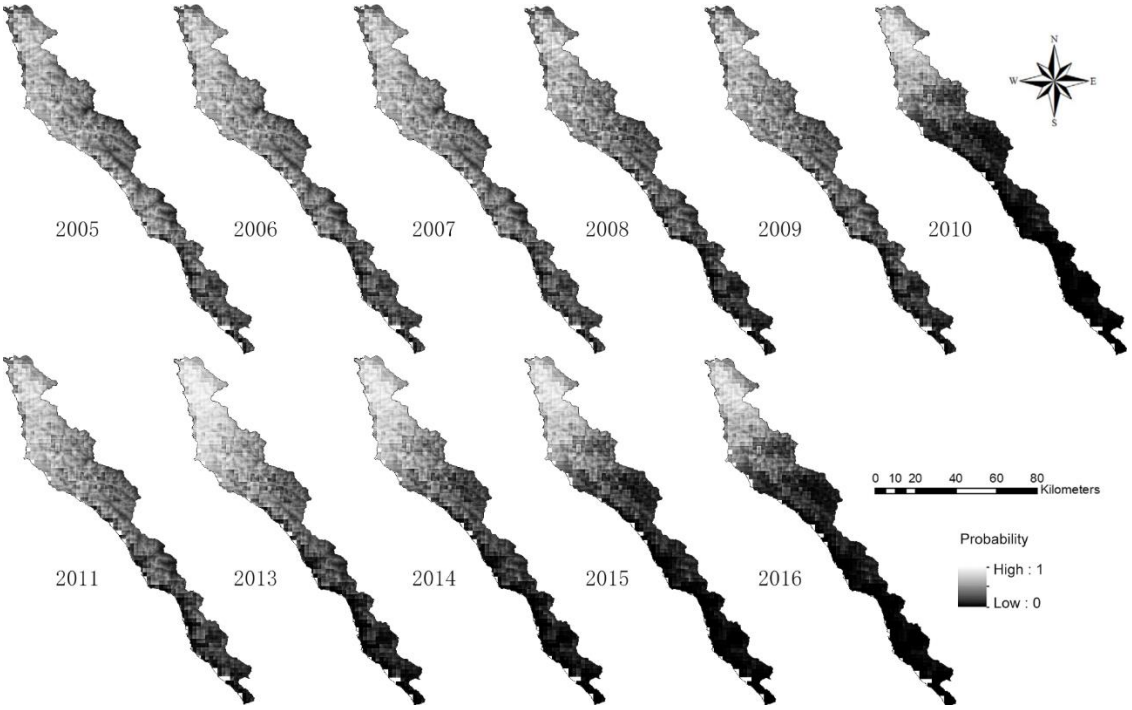

Fig. 1.11 Species distribution model derived probability map of sudden oak death infection from 2005 to 2016.

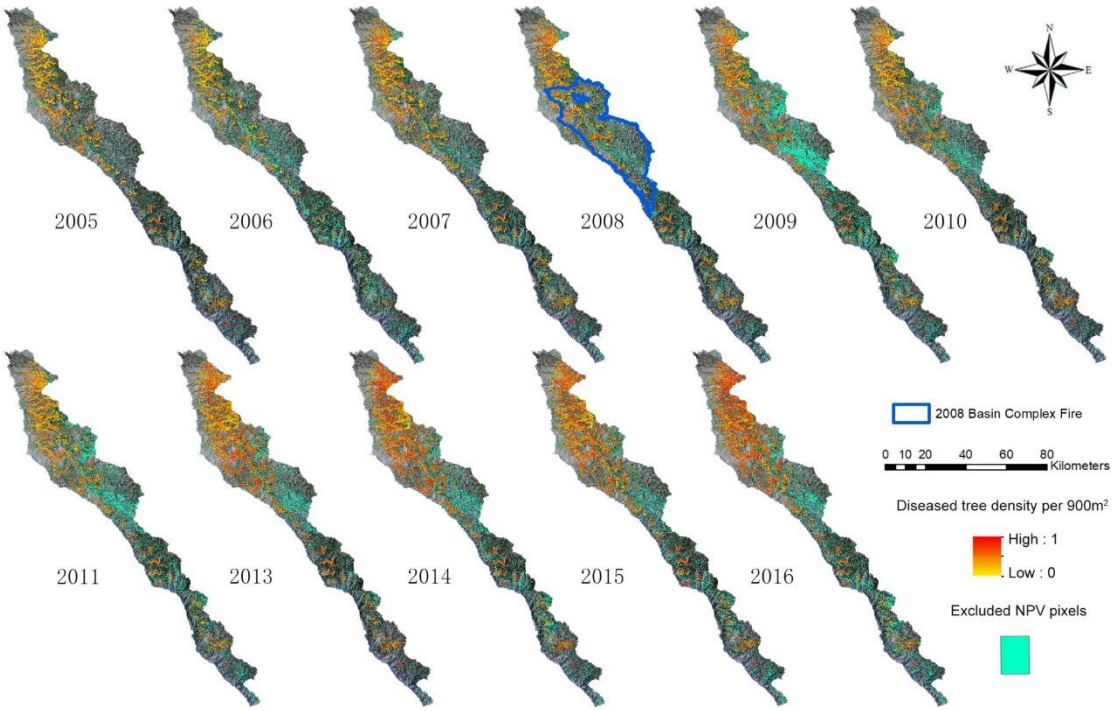

Fig. 1.12 Spatial distribution of the estimated density of sudden oak death-caused tree mortality per 900 m^2 from 2005 to 2016.

1.6. Discussion

1.6.1. Assessment of disease mapping using spectral unmixing

While plant disease-caused tree mortality has reached epidemic levels in forest landscapes, such as California's coastal forests (Chen and Meentemeyer, 2016), many diseases (including sudden oak death) demonstrate isolated, patchy progression patterns. In our study, spectral unmixing proved to be effective for extracting tree mortality at the Landsat sub-pixel level. Such an approach differs from the previous efforts of sudden oak death modeling, which solely relied on high-spatial-resolution imagery for small-area mapping (e.g., Kelly et al., 2007; Liu et al., 2006; Meentemeyer et al., 2008a). Through comparing MESMA-derived NPV fractions (Fig. 1.8) with the high-resolution sudden oak death map, we found a similar pattern of disease occurrence mainly on the west coast of the study area in 2005.

Although promising, spectral unmixing was found to overestimate disease-caused tree mortality. For example, Fig. 1.8 shows high-value NPV pixels in some of the southern and eastern parts of the region, which have yet to be heavily impacted by sudden oak death in 2005 according to field observations and high-spatial-resolution images. Similar overestimation patterns were found in the NPV results over the succeeding years. This was mainly due to the use of Landsat imagery that has a limited number of spectral bands, unable to accurately identify the spectral differences in some dead trees affected by sudden oak death *versus* other disturbances (e.g., extreme drought and wildfires). We also found relatively higher accuracies in the maps using the data collected more recently (e.g., years 2013, 2014, 2015 and 2016). Those data were from the Landsat-8 OLI sensor (as compared to the other data from Landsat 5 TM). The data

quality (signal to noise ratio) and radiometric quantization (12 bits) of Landsat 8 OLI is higher than those of previous Landsat instruments (e.g., 8 bits for TM), providing a significant improvement in the ability to detect land cover on the Earth's surface (Roy et al., 2014). The improved data quality of Landsat 8 OLI may have positively contributed to such phenomenon. When comparing the mapping accuracies between healthy and diseased trees, the results showed differences [see (b) in Fig. 1.10]. From 2005 to 2016, the producer's accuracies of healthy trees were consistently higher than that of diseased trees, and their user's accuracies were lower [see (b) in Fig. 1.10].

1.6.2. Effects of SDM on disease mapping

The developed SDM indicated that higher probabilities were correlated with the forests experiencing relatively warm and wet climatic conditions, and that were located at low elevations in the mountainous study area (Eq.10). Similar significant factors (e.g., precipitation, temperature, and elevation) were found in a previous study by Meentemeyer et al. (2008a), who applied an SDM to predict the invasion of sudden oak death pathogen *P. ramorum* using field plots only.

Compared to the MESMA-derived NPV results, the SDM consistently improved the estimation of sudden oak death-caused tree mortality over years (see Fig. 1.13 for a comparison), leading to an average of 26% decrease in detecting diseased forests. This was equivalent to an average of 818.4 ha each year, ranging from the minimum of 424.8 ha and the maximum of 1,187.1 ha. The difference between the NPV and the SDM-constrained results was partially explained by two major drought events that severely affected California's coastal ecosystems. For example, the overall rainfall levels in the central coast were about 50% of average over 2007-2009 (California Dept. Water

Resources, 2010). Starting from 2012, the region experienced severe drought again for five consecutive years (U.S. Geological Survey, 2017). Our field visits and aerial photo interpretation both discovered large areas of stressed and dead tree canopies in the areas unsuitable to be infected by sudden oak death.

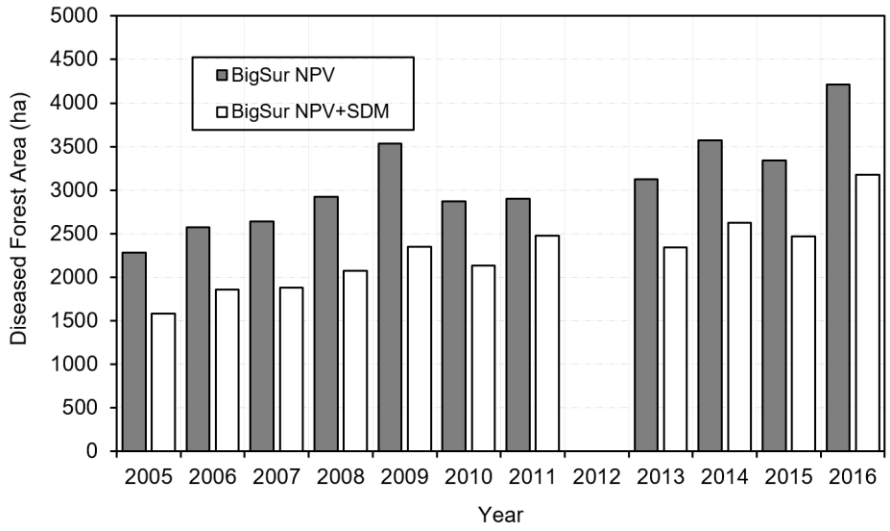

Fig. 1.13 Annual sudden oak death-impacted forest area from NPV versus NPV+SDM (species distribution model) for the entire study area.

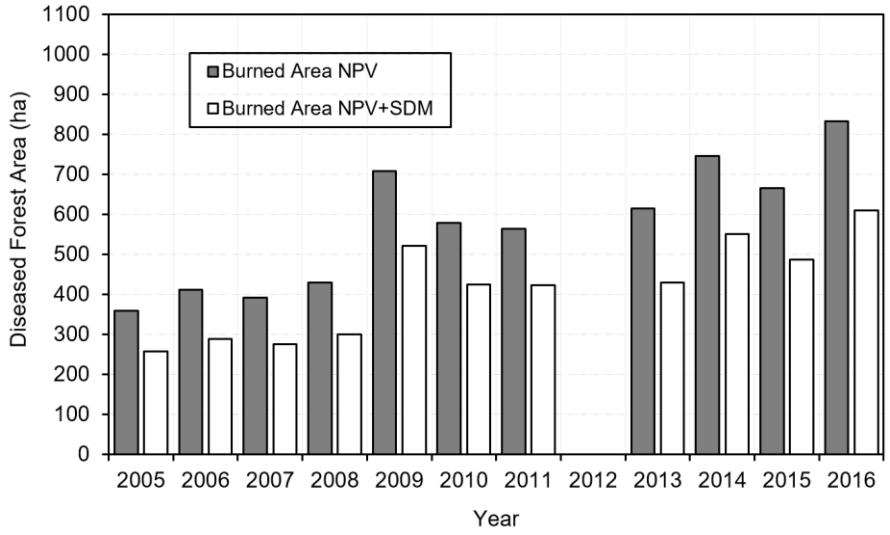

Fig. 1.14 Annual sudden oak death-impacted forest area from NPV versus NPV+ SDM (species distribution model) in part of the study area that was burned in 2008 (see Fig. 1.12 for the location and size of the burned area).

In summer 2008, the Basin Complex Fire that was ignited by a dry lightning storm burned the northern part of our study area (Fig. 1.12). Because some diseased trees revealed similar spectral reflectance as the burned trees owing to reduced foliage water content and damaged tree structure (Chen et al., 2017; He et al., 2019), the high spectral similarity and the relatively low Landsat spectral resolution did not provide sufficient information for MESMA to accurately extract diseased trees. Instead, MESMA treated some burned trees as being affected by sudden oak death, causing a major increase in the NPV result in 2009 (Fig. 1.13). In contrast, the SDM was able to mitigate the overestimation effect, making it valuable for generating reasonable sudden oak death progression maps in the regions affected by compound disturbances. However, the high-spectral similarities between burned (within five years following the fire occurrence) and diseased canopies definitely affect the effectiveness of SDM. Spectral similarities also

apply to the drought- and disease-killed trees, although studies have found less severe tree mortality caused by drought in coastal forests (including our study area) than their inland counterparts (Baguskas et al., 2014; Fischer et al., 2009). Nevertheless, it is possible that the presence of sudden oak death remains overestimated by our model. Acquiring detailed field measurements of tree mortality caused by both the disease and fire/drought offers a solution to better train our model and assess its performance in distinguishing between the two disturbance types. Another viable solution, as suggested by He et al. (2019), is using hyperspectral data with enhanced spectral signatures from the shortwave infrared portion of the spectrum. Because different types of disturbances may reveal varying progression patterns over time, high-resolution time series images have the potential to capture those patterns. However, data acquisition and processing costs are considerably higher than using time series data at the medium resolution.

1.7. Conclusion

We developed a new mapping method to capture the spatiotemporal patterns of diseased-caused tree mortality in a forested area for over a decade. The rationale of integrating remote sensing and SDM was based on the fact that remotely observed tree mortality may be associated with both disease and non-disease disturbances; such uncertainties can be reduced by understanding pathogen spatial preferences for certain habitat conditions (i.e., using SDM). The proposed method bridges remote sensing and ecological SDM in a way that has not been well studied. Here, we used sudden oak death (caused by pathogen *P. ramorum*) as a case study of a rapidly spreading EID. The results show that SDM considerably reduced the overestimation of sudden oak death-caused tree mortality observable from Landsat imagery. However, due to the lack of detailed field

observations (e.g., drought-caused tree mortality), we were unable to assess what percentage of the overestimation was from what specific causes, other than sudden oak death. Our interpretation that the overestimated tree mortality was mainly linked to drought/fire was based on the reported severe weather events in the region (Asner et al., 2016). Nevertheless, our study represents the best way linking multi-scale remote sensing observations to highlight areas that are probably not affected by sudden oak death so we can focus the disease management efforts in areas that need them. The final annual tree mortality maps show accuracies ranging from 75.5% to 82.5%. To balance data costs and the ability to map the pathogen's isolated, patchy distribution patterns, in this study we applied spectral unmixing to Landsat TM/OLI time series. Our model was calibrated and validated by disease reference data from high-resolution image samples (aerial NAIP and AVIRIS photos and Google Earth imagery) and field surveys. Coupling multi-sensor, multi-scale remote sensing (full-cover Landsat imagery and sampled high-resolution images) and SDM offer a timely and cost-effective means to map long-term forest disease progression at the regional scale.

Acknowledgments

This research was supported by the National Science Foundation (EF-0622770) as part of the joint NSF-NIH Ecology and Evolution of Infectious Disease program, the North Carolina Space Grant, and the University of North Carolina at Charlotte CLAS Junior Faculty Development Award. The authors also gratefully acknowledge financial support from the USDA Forest Service – Pacific Southwest Research Station, and the Gordon & Betty Moore Foundation. We thank numerous contributors who provided vital field and laboratory support, including J. Geng, K. Aram, M. Beh, A. Brauer, M. Chan,

C, DeLong, W. Dillon, K. Frangioso, A. Hohl, H. Mehl, A. Oguchi, E. Paddock, K. Pietrzak, M. Vaclavikova, J. Vieregge, L. Waks and A. Wickland.

References

Alexander, J., 2012. The past, present, and future of sudden oak death. Outlooks on Pest Manag. 23, 72–76.

Allouche, O., Tsoar, A., Kadmon, R., 2006. Assessing the accuracy of species distribution models: prevalence, kappa and the true skill statistic (TSS). J. Appl. Ecol. 43,1223–1232.

Anderegg, W.R.L., Kane, J.M., Anderegg, L.D.L., 2013. Consequences of widespread tree mortality triggered by drought and temperature stress. Nat. Clim. Chang. 3, 30–36.

Asner, G.P., 2013. Geography of forest disturbance. Proc. Natl. Acad. Sci. 110, 3711–3712.

Asner, G.P., Brodrick, P.G., Anderson, C.B., Vaughn, N., Knapp, D.E., Martin, R.E., 2016. Progressive forest canopy water loss during the 2012–2015 California drought. Proc. Natl. Acad. Sci. 113, 249–255.

ASTER GDEM Validation Team, 2011. ASTER Global Digital Elevation Model Version 2 – Summary of Validation Results. Available online at http://www.jspacesystems.or.jp/ersdac/GDEM/ver2Validation/Summary_GDEM2_validion_report_final.pdf. (last accessed on March 20, 2019).

Baguskas, S.A., Peterson, S.H., Bookhagen, B., Still, C.J., 2014. Evaluating spatial patterns of drought-induced tree mortality in a coastal California pine forest. For. Ecol. Manag. 315, 43–53.

Berk, A., Anderson, G.P., Acharya, P.K., Bernstein, L.S., Muratov, L., Lee, J., Fox, M., Adler-Golden, S.M., Chetwynd Jr., J.H., Hoke, M.L., Lockwood, R.B., Gardner,

J.A., Cooley, T.W., Borel, C.C., Lewis, P.E., Shettle, E.P., 2006. MODTRAN5: 2006 update. In: Proceedings of SPIE - The International Society for Optical Engineering, p. 62331F.

Boyd, I.L., Freer-Smith, P.H., Gilligan, C.A, Godfray, H.C.J., 2013. The consequence of tree pests and diseases for ecosystem services. Science 342, 1235773.

Bright, B. C., Hicke, J. A., Hudak, A. T., 2012. Estimating aboveground carbon stocks of a forest affected by mountain pine beetle in Idaho using lidar and multispectral imagery. Remote Sens. Environ. 124, 270–281.

Brodrick, P.G., Asner, G.P., 2017. Remotely sensed predictors of conifer tree mortality during severe drought. Environ. Res. Lett. 12, 115013.

Byer, S. Jin, Y., 2017. Detecting Drought-Induced Tree Mortality in Sierra Nevada Forests with Time Series of Satellite Data. Remote Sens. 9, 929.

California Department of Water Resources (CDWR), 2010. Governor's Drought Declaration, California Department of Water Resources.

Carneiro, L.R.D.A., Lima, A.P., Machado, R.B., Magnusson, W.E., 2016. Limitations to the use of species-distribution models for environmental-impact assessments in the Amazon. PLoS One 11, 1–17.

Chen, G., Hay, G.J., St-Onge, B., 2012. A GEOBIA framework to estimate forest parameters from lidar transects, Quickbird imagery and machine learning: A case study in Quebec, Canada. Int. J. Appl. Earth Obs. Geoinf. 15, 28–37.

Chen, G., He, Y., De Santis, A., Li, G., Cobb, R., Meentemeyer, R.K., 2017. Assessing the impact of emerging forest disease on wildfire using Landsat and KOMPSAT-2 data. Remote Sens. Environ. 195, 218–229.

Chen, G., Meentemeyer, R.K., 2016. Remote sensing of forest damage by diseases and insects. In: Weng, Q. (Ed.), Remote Sensing for Sustainability. CRC Press, Taylor & Francis Group, Boca Raton, Florida, pp. 145–162.

Chen, G., Metz, M.R., Rizzo, D.M., Dillon, W.W., Meentemeyer, R.K., 2015a. Object-based assessment of burn severity in diseased forests using high-spatial and high-spectral resolution MASTER airborne imagery. ISPRS J. Photogramm. Remote Sens. 102, 38–47.

Chen, G., Metz, M.R., Rizzo, D.M., Meentemeyer, R.K., 2015b. Mapping burn severity in a disease-impacted forest landscape using Landsat and MASTER imagery. Int. J. Appl. Earth Obs. Geoinf. 40, 91–99.

Clark, R. N., Swayze, G. A., Livo, K. E., Kokaly, R. F., King, T. V. V., Dalton, J. B., Vance, J.S., Rockwell, B.W., Hoefen, T. and McDougal, R.R., 2002. Surface reflectance calibration of terrestrial imaging spectroscopy data: A tutorial using AVIRIS. In R. O. Green (Ed.), Proceedings of the 10th JPL airborne science workshop: JPL Publication 02-1. Available online at http://speclab.cr.usgs.gov/PAPERS.calibration.tutorial (last accessed on March 20, 2019).

Coops, N.C., Johnson, M., Wulder, M.A., White, J.C., 2006. Assessment of QuickBird high spatial resolution imagery to detect red attack damage due to mountain pine beetle infestation. Remote Sens. Environ. 103, 67–80.

Cunniffe, N.J., Cobb, R.C., Meentemeyer, R.K., Rizzo, D.M., Gilligan, C.A., 2016. Modeling when, where, and how to manage a forest epidemic, motivated by sudden oak death in California. Proc. Natl. Acad. Sci. 113, 5640–5645.

Davidson, J.M., Wickland, A.C., Patterson, H.A., Falk, K.R. and Rizzo, D.M., 2005. Transmission of Phytophthora ramorum in mixed-evergreen forest in California. Phytopathology 95, 587–596.

Davis, F.W., Borchert, M., Meentemeyer, R.K., Flint, A., Rizzo, D.M., 2010. Pre-impact forest composition and ongoing tree mortality associated with sudden oak death in the Big Sur region; California. For. Ecol. Manage. 259, 2342–2354.

Dennison, P.E., Halligan, K.Q. and Roberts, D.A., 2004. A comparison of error metrics and constraints for multiple endmember spectral mixture analysis and spectral angle mapper. Remote Sens. Environ. 93, 359–367.

Dubayah, R. C. 1994. Modeling a solar radiation topoclimatology for the Rio Grande River Basin. J. Veg. Sci. 5, 627–640.

Elith, J., Leathwick, J.R., 2009. Species Distribution Models: Ecological Explanation and Prediction Across Space and Time. Annu. Rev. Ecol. Evol. Syst. 40, 677–697.

Fassnacht, F.E., Latifi, H., Ghosh, A., Joshi, P.K., Koch, B., 2014. Assessing the potential of

hyperspectral imagery to map bark beetle-induced tree mortality. Remote Sens. Environ. 140, 533–548.

Fischer, D.T., Still, C.J., Williams, A.P., 2009. Significance of summer fog and overcast for drought stress and ecological functioning of coastal California endemic plant species. J. Biogeogr. 36, 783–799.

Franklin, J.,1995. Predictive vegetation mapping: Geographic modelling of biospatial patterns in relation to environmental gradients. Prog. Phys. Geogr. 19, 474–499.

Freeman, E.A., Moisen, G.G., 2008. A comparison of the performance of threshold

criteria for binary classification in terms of predicted prevalence and kappa. Ecol. Model. 217, 48–58.

Ghulam, A., Porton, I., Freeman, K., 2014. Detecting subcanopy invasive plant species in tropical rainforest by integrating optical and microwave (InSAR/PolInSAR) remote sensing data, and a decision tree algorithm. ISPRS J. Photogramm. Remote Sens. 88, 174–192.

Hatala, J.A., Crabtree, R.L., Halligan, K.Q., Moorcroft, P.R., 2010. Landscape-scale patterns of forest pest and pathogen damage in the Greater Yellowstone Ecosystem. Remote Sens. Environ. 114, 375–384.

He, K.S., Bradley, B.A., Cord, A.F., Rocchini, D., Tuanmu, M.N., Schmidtlein, S., Turner, W., Wegmann, M., Pettorelli, N., 2015. Will remote sensing shape the next generation of species distribution models? Remote Sens. Ecol. Conserv. 1, 4–18

He, T., Liang, S., Wang, D., Shi, Q., Goulden, M.L., 2015. Estimation of high-resolution land surface net shortwave radiation from AVIRIS data: Algorithm development and preliminary results. Remote Sens. Environ. 167, 20–30.

He, Y., G. Chen, A. De Santis, D. A. Roberts, Y. Zhou, R. K. Meentemeyer., 2019. A disturbance weighting analysis model (DWAM) for mapping wildfire burn severity in the presence of forest disease. Remote Sens. Environ. 221, 108–121.

Hultquist, C., Chen, G., Zhao, K., 2014. A comparison of Gaussian process regression, random forests and support vector regression for burn severity assessment in diseased forests. Remote Sens. Lett. 5, 723–732.

Hunter, S., Williams, N., McDougal, R., Scott, P., Garbelotto, M., 2018. Evidence for rapid adaptive evolution of tolerance to chemical treatments in Phytophthora

species and its practical implications. PLoS One 13(12): e0208961.

Ivors, K., Garbelotto, M., Vries, I.D.E., Ruyter-Spira, C., Hekkert, B. Te, Rosenzweig, N., Bonants, P., 2006. Microsatellite markers identify three lineages of Phytophthora ramorum in US nurseries, yet single lineages in US forest and European nursery populations. Mol. Ecol. 15, 1493–1505.

Kelly, M., Guo, Q., Liu, D., Shaari, D., 2007. Modeling the risk for a new invasive forest disease in the United States: an evaluation of five environmental niche models. Comput. Environ. Urban Syst. 31, 689–710.

Kelly, M., Meentemeyer, R.K., 2002. Landscape dynamics of the spread of sudden oak death. Photogramm. Eng. Remote. Sens. 68, 1001–1009.

Kelly, M., Shaari, D., Guo, Q.H., Liu, D., 2004. A comparison of standard and hybrid classifier methods for mapping hardwood mortality in areas affected by "sudden oak death." Photogramm. Eng. Remote Sensing 70, 1229–1239.

Likens, G., Bormann, F., Johnson, N., 1981. Interactions between major biogeochemical cycles in terrestrial ecosystems. In: Likens, G. (Ed.) Some Perspectives of the Major Biogeochemical Cyclespp, pp. 93–112.

Liu, D., Kelly, M., Gong, P., 2006. A spatial-temporal approach to monitoring forest disease spread using multi-temporal high spatial resolution imagery. Remote Sens. Environ. 101, 167–180.

Liu, D., Kelly, M., Gong, P., Guo, Q., 2007. Characterizing spatial-temporal tree mortality patterns associated with a new forest disease. For. Ecol. Manage. 253, 220–231.

McDowell, N., Allen, C.D., Anderson-Teixeira, K., Brando, P., Brienen, R., Chambers,

J., Christoffersen, B., Davies, S., Doughty, C., Duque, A. and Espirito-Santo, F., 2018. Drivers and mechanisms of tree mortality in moist tropical forests. New Phytol. 219, 851–869.

McGarigal, K., 2014. FRAGSTATS Help. University of Massachusetts, Amherst, MA (209 pp.).

McGarigal, K., Marks, B.J., 1995. FRAGSTATS: Spatial Pattern Analysis Program for Quantifying Landscape Structure. U.S. Department of Agriculture Forest Service. Pacific Northwest Research Station, Portland, OR, p. 122. Report nr Gen. Tech. Re. PNW-GTR-351.

Meddens, A.J.H., Hicke, J.A., Vierling, L.A., 2011. Evaluating the potential of multispectral imagery to map multiple stages of tree mortality. Remote Sens. Environ. 115, 1632–1642.

Meddens, A. J. H., Hicke, J. A., Vierling, L. A., Hudak, A. T., 2013. Evaluating methods to detect bark beetle-caused tree mortality using single-date and multi-date Landsat imagery. Remote Sens. Environ. 132, 49–58.

Meentemeyer, R.K., Anacker, B.L., Mark, W., Rizzo, D.M., 2008a. Early detection of emerging forest disease using dispersal estimation and ecological niche modeling. Ecol. Appl. 18, 377–390.

Meentemeyer, R.K., Cunniffe, N.J., Cook, A.R., Filipe, J.A.N., Hunter, R.D., Rizzo, D.M., Gilligan, C.A., 2011. Epidemiological modeling of invasion in heterogeneous landscapes: spread of sudden oak death in California (1990–2030). Ecosphere 2, art17.

Meentemeyer, R.K., Dorning, M.A., Vogler, J.B., Schmidt, D., Garbelotto, M., 2015.

Citizen science helps predict risk of emerging infectious disease. Front. Ecol. Environ. 13, 189–194.

Meentemeyer, R.K., Rank, N.E., Shoemaker, D.A., Oneal, C.B., Wickland, A.C., Frangioso, K.M., Rizzo, D.M., 2008b. Impact of sudden oak death on tree mortality in the Big Sur ecoregion of California. Biol. Invasions 10, 1243–1255.

Moore, I.D., Grayson, R.B., Ladson, a R., 1991. Digital Terrain Modeling : A Review of Hydrological Geomorphological and Biological Applications. Hydrol. Process. 5, 3–30.

NASA, 2018. Landsat Science. https://landsat.gsfc.nasa.gov/landsat-data-continuity-mission/ (last accessed on March 20, 2019).

Negrón-Juárez, R.I., Holm, J.A., Marra, D.M., Rifai, S.W., Riley, W.J., Chambers, J.Q., Koven, C.D., Knox, R.G., McGroddy, M.E., Di Vittorio, A.V., Urquiza-Muñoz, J., 2018. Vulnerability of Amazon forests to storm-driven tree mortality. Environ. Res. Lett. 13, 054021.

Pasquarella, V.J., Bradley, B.A., Woodcock, C.E., 2017. Near-real-time monitoring of insect defoliation using Landsat time series. Forests 8, 275.

Paz-Kagan, T., Brodrick, P.G., Vaughn, N.R., Das, A.J., Stephenson, N.L., Nydick, K.R. and Asner, G.P., 2017. What mediates tree mortality during drought in the southern Sierra Nevada? Ecol. Appl. 27, 2443–2457.

Potere, D., 2008. Horizontal positional accuracy of Google Earth's high-resolution imagery archive. Sensors 8, 7973–7981.

Potter, C., 2016. Landscape Patterns of Burn Severity in the Soberanes Fire of 2016. J. Geogr. Nat. Disast. S6:005, doi: 10.4172/2167–0587.S6-005.

Prospero, S., Hansen, E.M., Grünwald, N.J., Winton, L.M., 2007. Population dynamics of the sudden oak death pathogen Phytophthora ramorum in Oregon from 2001 to 2004. Mol. Ecol. 16, 2958–2973.

R Core Team, 2017. R: A Language and Environment for Statistical Computing. R Foundation for Statistical Computing, Vienna, Austria URL. https://www.r-project.org/ (last accessed on March 20, 2019).

Rizzo, D.M., Garbelotto, M., Davidson, J.M., Slaughter, G.W., Koike, S.T., 2002. Phytophthora ramorum as the cause of extensive mortality of Quercus spp. and Lithocarpus densiflorus in California. Plant Dis. 86, 205–214.

Rizzo, D.M., Garbelotto, M., Hansen, E.M., 2005. Phytophthora ramorum: integrative research and management of an emerging pathogen in California and Oregon forests. Annu. Rev. Phytopathol. 43, 309–35.

Roberts, D.A., Dennison, P.E., Gardner, M.E., Hetzel, Y., Ustin, S.L., Lee, C.T., 2003. Evaluation of the potential of Hyperion for fire danger assessment by comparison to the airborne visible/infrared imaging spectrometer. IEEE Trans. Geosci. Remote Sens. 41, 1297–1310.

Roberts, D.A., Gardner, M., Church, R., Ustin, S., Scheer, G., Green, R.O., 1998. Mapping chaparral in the Santa Monica Mountains using multiple endmember spectral mixture models. Remote Sens. Environ. 65, 267–279.

Roberts, D.A., Halligan, K., Dennison, P., 2007. VIPER Tools User Manual. V1.5.

Rocchini, D., Andreo, V., Förster, M., Garzon-Lopez, C.X., Gutierrez, A.P., Gillespie, T.W., Hauffe, H.C., He, K.S., Kleinschmit, B., Mairota, P., Marcantonio, M., 2015. Potential of remote sensing to predict species invasions: A modelling

perspective. Prog. Phys. Geogr. 39, 283–309.

Roy, D.P., Wulder, M.A., Loveland, T.R., Woodcock, C.E., Allen, R.G., Anderson, M.C., Helder, D., Irons, J.R., Johnson, D.M., Kennedy, R.E., Scambos, T.A., Schaaf, C.B., Schott, J.R., Sheng, Y., Vermote, E.F., Belward, A.S., Bindschadler, R., Cohen, W.B., Gao, F., Hipple, J.D., Hostert, P., Huntington, J., Justice, C.O., Kilic, A., Kovalskyy, V., Lee, Z.P., Lymburner, L., Masek, J.G., McCorkel, J., Shuai, Y., Trezza, R., Vogelmann, J., Wynne, R.H., Zhu, Z., 2014. Landsat-8: science and product vision for terrestrial global change research. Remote Sens. Environ. 145, 154–172.

Rullan-Silva, C.D., Olthoff, A.E., de la Mata, J.A.D., Pajares-Alonso, J.A., 2013. Remote monitoring of forest insect defoliation-a review. Forest Syst. 22, 377–391.

Saatchi, S., Buermann, W., ter Steege, H., Mori, S., & Smith, T. B., 2008. Modeling distribution of Amazonian tree species and diversity using remote sensing measurements. Remote Sens. Environ. 112, 2000–2017.

Sansford, C.E., Inman, A.J., Baker, R., Brasier, C., Frankel, S., de Gruyter, J., Husson, C., Kehlenbeck, H., Kessel, G., Moralejo, E., Steeghs, M., Webber, J., Werres, S., 2008. Report on the Risk of Entry, Establishment, Spread and Socio-economic Loss and Environmental Impact and the Appropriate Level of Management for Phytophthora ramorum for the EU. Deliverable Report 28. EU Sixth Framework Project RAPRA.

Shirk, A. J., Lopez-Sanchez, C. A., Toney, C., Cushman, S. A., Wehenkel, C. A., Leal-Sáenz, A., Waring, K. M., 2018. Southwestern white pine (Pinus strobiformis) species distribution models project a large range shift and contraction due to

regional climatic changes. For. Ecol. Manage., 411, 176–186.

Skowronek, S., Ewald, M., Isermann, M., Van De Kerchove, R., Lenoir, J., Aerts, R., Warrie, J., Hattab, T., Honnay, O., Schmidtlein, S., Rocchini, D., 2017. Mapping an invasive bryophyte species using hyperspectral remote sensing data. Biol. Invasions 19, 239–254.

Sturrock, R.N., Frankel, S.J., Brown, A. V., Hennon, P.E., Kliejunas, J.T., Lewis, K.J., Worrall, J.J., Woods, A.J., 2011. Climate change and forest diseases. Plant Pathol. 60, 133–149.

Thornton, M.M., Thornton, P.E., Wei, Y., Mayer, B.W., Cook, R.B., VoseR, S., 2018. Daymet: Monthly Climate Summaries on a 1-km Grid for North America, Version 3. ORNL DAAC, Oak Ridge, Tennessee, USA.

Turner, M. G., Gardner, R. H., O'Neill, R. V., 2001. Landscape ecology in theory and practice: Pattern and process. Springer

USDA, 2012. National Agriculture Imagery Program (NAIP) Orthoimagery. Available online: https://www.fsa.usda.gov/Internet/FSA_File/naip_2012_infosheet.pdf (last accessed on March 20, 2019).

U.S. Geological Survey. 2017. California Drought. U.S. Geological Survey, California Water Science Center.

U.S. Geological Survey. 2018a. Landsat 4-7 Surface Reflectrance (LEDAPS) Product.

U.S. Geological Survey. 2018b. Landsat 8 Surface Reflectrance Code (LaSRC) Product.

Václavík, T., Meentemeyer, R.K., 2009. Invasive species distribution modeling (iSDM): Are absence data and dispersal constraints needed to predict actual distributions?

Ecol. Modell. 220, 3248–3258.

Vaughn, N.R., Asner, G.P., Brodrick, P.G., Martin, R.E., Heckler, J.W., Knapp, D.E., Hughes, R.F., 2018. An Approach for High-Resolution Mapping of Hawaiian Metrosideros Forest Mortality Using Laser-Guided Imaging Spectroscopy. Remote Sens. 10, 502.

Wingfield, M.J., Brockerhoff, E.G., Wingfield, B.D., Slippers, B., 2015. Planted forest health: the need for a global strategy. Science 349, 832–836.

Chapter 2: A Disturbance Weighting Analysis Model (DWAM) for Mapping Wildfire Burn Severity in the Presence of Forest Disease

Abstract

Forest ecosystems are subject to recurring fires as one of their most significant disturbances. Accurate mapping of burn severity is crucial for post-fire land management and vegetation regeneration monitoring. Remote-sensing-based monitoring of burn severity faces new challenges when forests experience both fire and non-fire disturbances, which may change the biophysical and biochemical properties of trees in similar ways. In this study, we develop a Disturbance Weighting Analysis Model (DWAM) for accurately mapping burn severity in a forest landscape that is jointly affected by wildfire and an emerging infectious disease – sudden oak death. Our approach treats burn severity in each basic mapping unit (e.g., 30 m grid from a post-fire Landsat image) as a linear combination of burn severity of trees affected (diseased) and not affected by the disease (healthy), weighted by their areal fractions in the unit. DWAM is calibrated using two types of inputs: i) look-up tables (LUTs) linking burn severity and post-fire spectra for diseased and healthy trees, derived from field observations, hyperspectral sensors [e.g., Airborne Visible InfraRed Imaging Spectrometer (AVIRIS)], and radiative transfer models; and ii) pre-fire fractional maps of diseased and healthy trees, derived by decomposing a pre-fire Landsat image using Multiple Endmember Spectral Mixture Analysis (MESMA). Considering the presence of tree disease in DWAM improved the overall map accuracy by 42%. The superior performance is consistent across all three stages of disease progression. Our approach

demonstrates the potential for improved mapping of forest burn severity by reducing the confounding effects of other biotic disturbances.

2.1. Introduction

Forest fires directly transform living and dead organic matter to charred or blackened residues in the short term (Kokaly et al., 2007; Lewis et al., 2007) and over the long term they affect the structure, function, and spatial patterns of ecological succession (Turner et al., 1998; Metz et al., 2013; Chen et al., 2015b). Building accurate knowledge of the spatial distribution of fire extent and particularly *burn severity* is crucial in planning and executing post-fire land management activities (Keeley, 2009; Quintano et al., 2017). Over the past decade, the term burn severity has gained popularity to represent the degree of environmental change (typically the loss of organic matter on the soil surface) caused by a fire (Key and Benson, 2006; Keeley, 2009). Both short-term (e.g., about within one year following the fire) and long-term (e.g. up to ten years) impacts of fire on local environment have been assessed to understand the direct loss of vegetation by combustion and longer term recovery, respectively (Key and Benson, 2005; Lentile et al., 2006; Roy et al., 2006). To date, there have been numerous studies about burn severity estimation across forest biomes worldwide (e.g., Díaz-Delgado and Pons, 2001; French et al., 2008; Hall et al., 2008; Miller et al., 2009). Due to rapid environmental change and intensive human interventions, burn severity mapping is increasingly challenged by compound disturbances in forest ecosystems; with increasing frequency forest landscapes are being impacted by emerging infectious diseases or other forms of disturbance prior to fire occurrence (Bright et al., 2013; Hultquist et al., 2014; van Mantgem et al., 2013). Because pre-fire disturbances also cause the loss of organic

matter, estimating burn severity may introduce high uncertainties without properly considering the compound effects of multiple disturbances (Chen et al., 2017).

Remote sensing is effective to assess fire effects on forest ecosystems at local, regional and continental scales (e.g., Chen et al., 2018; Hudak and Brockett, 2004; Lentile et al., 2006; Quintano et al., 2013; Veraverbeke et al., 2012). It is especially suitable for monitoring large and topographically complex landscapes that are logistically unfeasible with traditional field surveys (Chuvieco et al., 2007; Chen et al., 2015a). Remote sensing models to estimate burn severity are typically categorized into two groups: empirical and physical models. Specifically, classic empirical models rely on statistical regression (e.g., linear regression) or machine learning (e.g., random forests) to link sample field measurements of burn severity with remotely sensed data, e.g., spectral bands and indices (band combinations), such as Normalized Burn Ratio (NBR; López-García and Caselles, 1991), differenced Normalized Burn Ratio (dNBR; Key and Benson, 2006), and relative differenced Normalized Burn Ratio (RdNBR; Miller and Thode, 2007). Such models are relatively easy to implement and interpret. However, their performance depends highly on the reliability and sufficiency of field samples and is site-specific, which reduce their generality across complex geographic conditions (De Santis and Chuvieco, 2007). More recently, researchers took advantage of spectral mixing analysis to retrieve forest burn severity at the sub-pixel level from medium- or coarse-resolution, and even high-resolution imagery. For instance, the classic Multiple Endmember Spectral Mixing Analysis (MESMA; Roberts et al., 1998) has been used to derive non-photosynthetic vegetation fraction (NPV) or char fractions, which serve as an explanatory factor to estimate burn effects in forests (e.g., Fernandez-

Manso et al., 2016; Meng et al., 2017, Quintano et al., 2017). While the spectra used in MESMA are typically from image sampling, they can also come from a radiative transfer model, as was true in Painter et al. (1998, 2003) and Sonnentag et al. (2007). Physical models attempt to address such limitation by simulating the physical interactions between radiation and burned canopies. A typical example is the use of radiative transfer models. Chuvieco et al. (2006) were the first to apply radiative transfer models, i.e., PROSPECT (Jacquemoud and Baret, 1990) and Kuusk (Kuusk, 2001) reflectance models, for burn severity estimation. De Santis et al. (2009) successfully simulated the spectra of burned canopies at 30 m resolution by integrating the leaf-level PROSPECT with the canopy-level GeoSail (Verhoef and Bach, 2003) models.

Despite the popularity of remote-sensing-based burn severity estimation, none of the present models explicitly account for the effects of pre-fire disturbances on map performance. Because both fire and non-fire disturbances (i.e., compound disturbances) may change the biophysical or biochemical properties of trees in similar ways (e.g., damaging tree structure or reducing foliage water content; Hultquist et al., 2014), pre- and post-fire spectral differences for the trees affected by non-fire disturbances are possibly different from their healthy counterparts. Uncertainties are further introduced if such non-fire disturbances affect forests at multiple stages showing various symptoms, leading to a weak relationship between spectral reflectance and burn severity. The negative impact of forest disease on burn severity estimation was recently confirmed by Chen et al. (2017), who employed PROSPECT and GeoSail to map burn severity in a forest that had been affected by an emerging infectious disease – sudden oak death –

prior to fire occurrence. Their results revealed a significant overestimation of burn effects by ignoring tree damage caused by the disease.

The main goal of this study is to develop a remote-sensing-based model to map burn severity in forest landscapes, aiming to reduce the effects of tree damage caused by pre-fire disturbances. Here, we used sudden oak death as an example of a pre-fire disturbance that has caused widespread tree mortality in the Big Sur, California ecoregion before the studied Basin Complex Fire occurred in 2008 (Chen et al., 2015a). In model development, it is assumed that the final burn effect for a basic mapping unit (e.g., 30 m grid) is a linear combination of burn severity of two tree classes (i.e., trees affected and not affected by the disease), weighted by their areal fractions. To achieve the research goal, we also asked two specific questions in model development and assessment: (i) whether (and if yes, how much) the estimation of forest burn severity can be improved by incorporating pre-fire, disease-caused tree mortality? And (ii) how differently does the new model perform at the early, middle, and late stage of disease progression?

2.2. Study area

Our study site (centered at 36°16' N, 121°44' W) is located in the Big Sur ecoregion on the western flank of Santa Lucia Mountain of California with a total area of 28,383 ha (Fig. 2.1). The area has a Mediterranean-type climate and a rugged landscape dissected by steep slopes and drainages with elevations ranging from sea level to 1,571m within 5 km of the coast (Meentemeyer et al., 2008). The area is dominated by a range of tree species: (i) mixed coniferous forest, composing of ponderosa pine (*Pinus ponderosa*), sugar pine (*Pinus lambertiana*), Jeffrey pine (*Pinus jeffreyii*), coulter pine

(*Pinus coulteri*), and Santa Lucia fir (*Abies bracteata*), which are located on upper elevation slopes and rocky ridges; and (ii) mixed oak woodland consisting of coast live oak (*Quercus agrifolia*), Shreve's oak (*Q. parvula*), bay laurel (*Umbellularia californica*), and madrone (*Arbutus menziesii*), which were found on moister slopes, giving way to riparian corridors of redwood-tanoak forest at lower elevations. Since the mid-1990s, an invasive pathogen *Phytophthora ramorum* causing the disease – sudden oak death – has led to extensive tree mortality in the study area mainly found in two plant communities – mixed oak and redwood-tanoak forests (Rizzo et al., 2005). The disease involves a multi-year progress especially under a suitable temperature and rainfall conditions, girdling a tree over years or making the tree more susceptible to attack by other pathogens or insects (Chen et al., 2015b). In 2008, a wildfire – the Basin Complex Fire – was ignited by a dry lightning storm in late June and burned over 65,942 ha of federal, state and private lands. The total cost of containment action was around $77.2 million mainly due to the sheer size of the fires, the ruggedness of the terrain and the extremely dry conditions (USDA Forest Service, 2008). The Basin Complex Fire affected forest landscapes, which had and had not been damaged by sudden oak death.

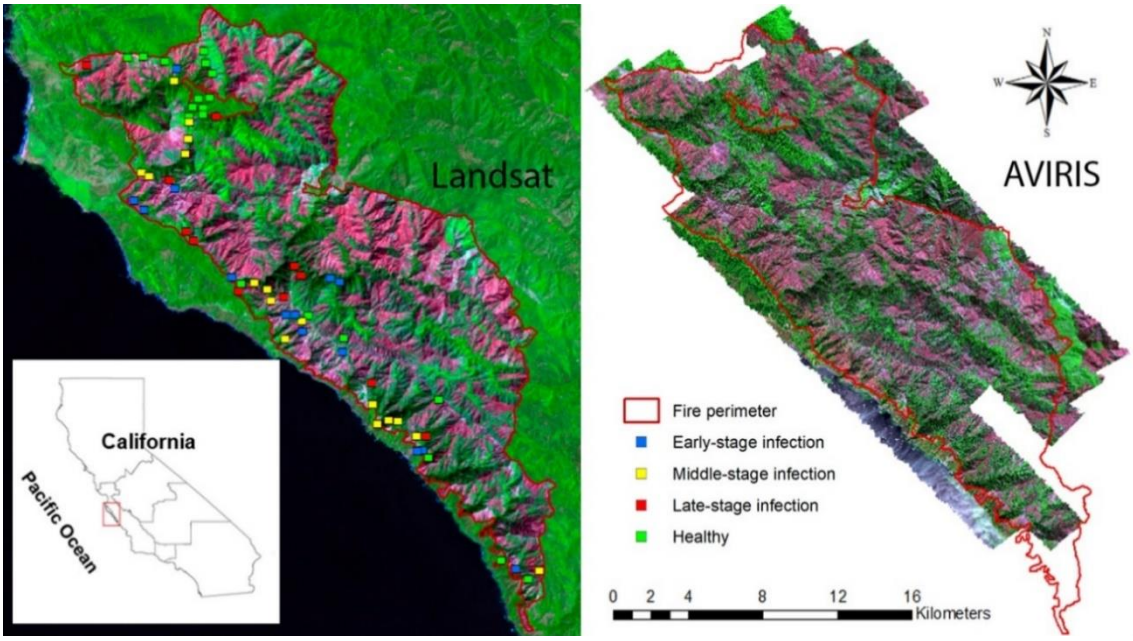

Fig. 2.1 Study area located in the Big Sur ecoregion on the western flank of the Santa Lucia Mountains in California. The Airborne Visible InfraRed Imaging Spectrometer (AVIRIS) image is from a color composite using bands 195 (red), 52 (green) and 31 (blue). The Landsat TM image is from a color composite using bands 7 (red), 4 (green) and 3 (blue).

2.3. Data and pre-processing

2.3.1. Field data

A solid network of long-term sudden oak death monitoring plots (500 m^2 each) in Big Sur was established in years 2006 and 2007 to understand the responses of forest communities (e.g., host mortality) to the invasion of sudden oak death (Meentemeyer et al., 2008). The plots were distributed in a stratified-random manner among two dominant tree types-redwood and mixed-evergreen within the study area. A Panasonic SXBlue real-time differential GPS (Geneq, Montreal) was applied for collecting plot positions, with an average accuracy of 1 m or less. A total of 61 plots were revisited after the

wildfire in September and October 2008. Among these plots, 42 had been affected by sudden oak death, and 19 had not. The affected plots evenly covered the three stages of disease progression from early, middle, to late stages.

Burn severity at the plot level was recorded using the Composite Burn Index (CBI; Key and Benson, 2005) for five forest strata: (1) substrate layer, measured as changes to coarse woody debris, soil, duff, and leaf litter; (2) herb layer, changes or responses of vegetation less than 1 m; (3) shrub layer, changes in vegetation higher than 1 m but less than 5 m; (4) intermediate-sized tree layer, any trees higher than 5 m but standing under the dominant trees; and (5) dominant tree layer (Metz et al., 2011). In this study, all the CBI values were converted to geometrically structured CBI (GeoCBI) values (maximum: 2.83, minimum: 0.56, average: 2.00, and standard deviation: 0.42). Proposed by De Santis and Chuvieco (2009), GeoCBI (ranging from 0.0-3.0) simulates burn severity with a 'top-down' view, to be consistent with remote sensing observations. GeoCBI accounts for the contribution of each forest stratum using its Fraction Cover (FCOV) as the weighting factor (see Eq. 1).

$$\text{GeoCBI} = \frac{\sum_{m_1}^{m_n}(CBI_m * FCOV_m)}{\sum_{m_1}^{m_n} FCOV_m} \quad (1)$$

where *FCOV* is calculated and characterized as the percentage of vegetation coverage with respect to the total size of the plot area, m is the identification of each stratum, and n is the number of strata.

2.3.2. AVIRIS imagery

The AVIRIS image mosaic (from seven transects) at the 3 m resolution was acquired on September 24, 2008, immediately following the containment of the

Basin Complex Fire for rapid assessment. AVIRIS is an imaging spectrometer that measures 224 contiguous spectral bands in the range of ~360 nm to ~2500 nm with an average bandwidth of 10 nm (Green et al., 1998). The images were geometrically corrected, radiometrically calibrated, and were made available at the JPL's website (http://aviris.jpl.nasa.gov). Atmospheric correction was performed using the Fast Line-of-sight Atmospheric Analysis of Spectral Hypercubes (FLAASH) module, which is available in the ENVI software package (ITT Visual Information Solutions, Colorado, USA). FLAASH uses the physics-based radiative transfer model MODTRAN 5 to perform atmospheric correction, which needs flight and sensor metadata (i.e., sensor type, scene center latitude/longitude, average ground elevation, sensor altitude, and flight date and time), as well as assumed or measured atmospheric parameters (i.e., atmosphere model, aerosol model, and atmosphere water vapor) to generate apparent surface reflectance spectra from radiance data (Berk et al., 2006). In our study, flight and sensor metadata are available with the image. To simulate atmospheric conditions, Mid-Latitude Summer (MLS) was selected as an atmosphere model (Matthew et al., 2002), as AVIRIS data were acquired in September (temperature around 21°C) at the latitude 36°N. Also because our study area is not strongly affected by urban or industrial sources, the rural aerosol model was selected (Shettle and Fenn, 1979). In order to compute apparent surface reflectance using radiative transfer equations in MODTRAN 5, the column water vapor amount for each pixel was determined using the 1135 nm water vapor absorption feature (Kruse, 2004). To mitigate topographic effects as the study area is a mountainous region, a Terrain Agular Bin method (TAB; Wen et al., 2014) was applied to correct for topographic effects using a 30 m resolution digital elevation model (DEM) derived from

the data collected by Advanced Spaceborne Thermal Emission and Reflection Radiometer (ASTER) as part of the Global Digital Elevation Model Version 2 (GDEM V2) project (ASTER GDEM Validation Team, 2011).

2.3.3. Landsat imagery

Two cloud-free Landsat-5 Thematic Mapper (TM) scenes (path 43, row 35) were acquired on May 13, 2008, and September 2, 2008, from the USGS Landsat Surface Reflectance High-Level Data Products (Schmidt et al., 2013) to represent pre- and post-fire forest conditions in the study area. The images have solar zenith angles of 26.6° and 36.2°, and solar azimuth angles of 124.7° and 135.9°, respectively. The data were downloaded via the U.S. Geological Survey Landsat data portal and had been geometrically, radiometrically, and topographically corrected before being made available online. In this study, we used six TM bands (1-5, and 7).

2.4. Methods

Our Disturbance Weighting Analysis Model (DWAM) includes three major steps (Fig. 2.2): (i) development of GeoCBI-spectrum look-up tables (LUTs), (ii) pre-fire fractional mapping, and (iii) burn severity mapping. To facilitate the succeeding model description and discussion, we defined the trees not affected by sudden oak death as '*healthy trees*', and those affected as '*diseased trees*', regardless of the burn effects. The overall methodological flow is briefly described in this paragraph. In step (i), we developed two LUTs linking burn severity as measured by GeoCBI with spectra for healthy and diseased trees, respectively. To do so, we used two spectral libraries: one was developed by De Santis and Chuvieco (2009), and the other one was derived from the post-fire AVIRIS data. In step (ii), we mapped fractional cover of healthy and

diseased trees prior to fire occurrence, which was completed by applying the spectral unmixing MESMA model to the pre-fire Landsat TM image. The AVIRIS data acquired outside of the fire scar was used to construct a spectral library consisting of healthy trees, diseased trees, and soil. In step (iii), we estimated burn severity (in 30 m grids) as a linear combination of burn severity of healthy and diseased trees, weighted by their areal fractions in each grid.

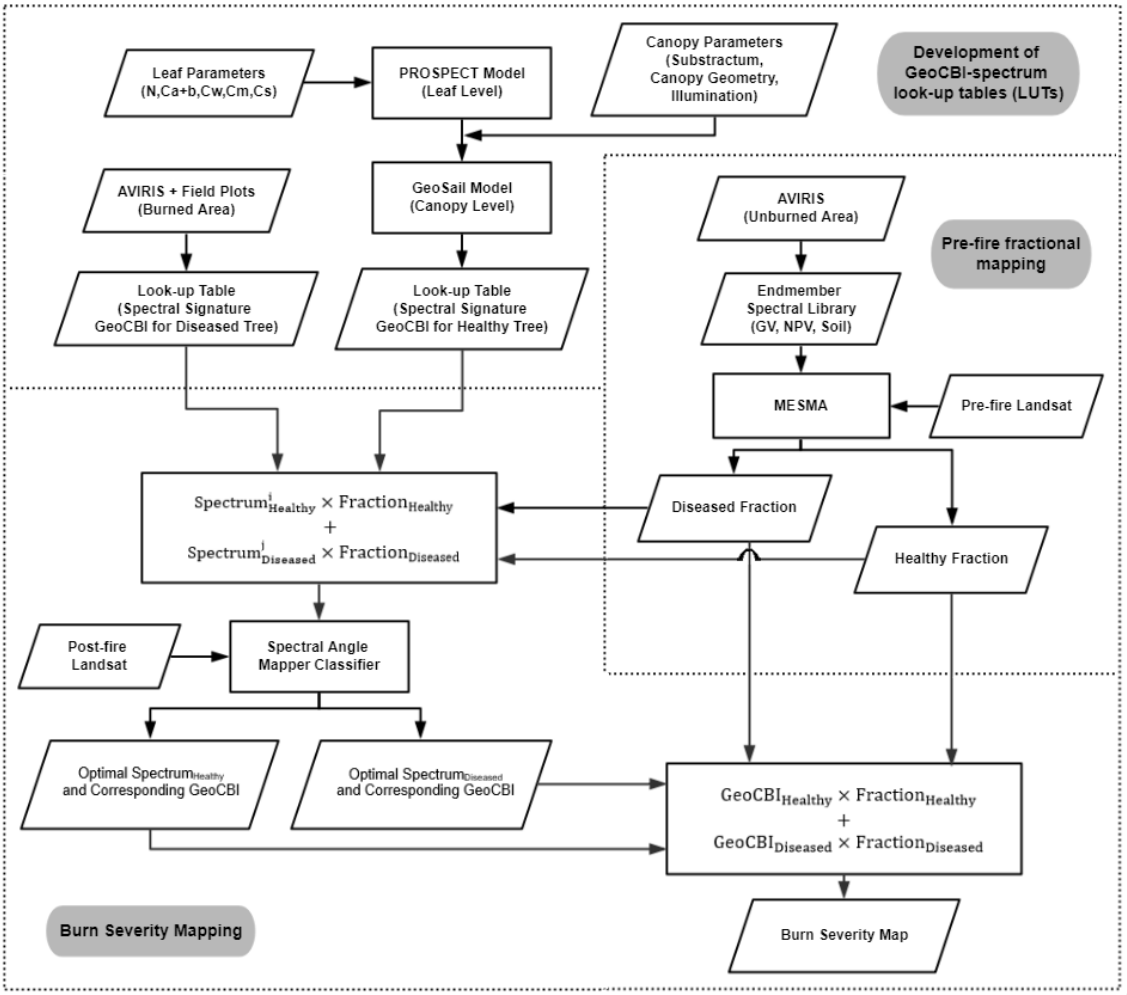

Fig. 2.2 Methodological workflow used in this study.

Finally, we evaluated DWAM performance using field-measured GeoCBI data. In order to further understand the effects of disease progression on DWAM performance,

we mapped disease infection at the early, middle, and late stages, and analyzed the relationship between infection stages and model performance. For the purpose of comparison, we also assessed burn severity with the traditional spectral-index-based approach, e.g., NBR, dNBR and RdNBR, which used both pre- and post-fire imagery.

2.4.1. Development of GeoCBI-spectrum LUTs

2.4.1.1. LUT for healthy trees

A spectral library for healthy trees was derived from a research project by De Santis and Chuvieco (2009), who studied forest burn severity in the Mediterranean ecosystem, where our study area is also located. Here, we did not use data from our study mainly due to the fact that only 11 healthy plots were covered by the AVIRIS image, preventing the extraction of meaningful LUT relating spectra and GeoCBI. The spectral library was developed using two radiative transfer models PROSPECT (Jacquemoud and Baret, 1990) and GeoSail (Verhoef and Bach, 2003) in two steps: (i) at the leaf level, the PROSPECT model was used to simulate spectra for brown (damaged by fire) and green (undamaged) leaves, where the input values included leaf structural parameter, chlorophyll a+b, equivalent water thickness, dry matter content, and brown pigments content (De Santis et al., 2009). (ii) The output of the PROSPECT model, together with a series of canopy parameters (substratum type, geometry, and illumination) (De Santis et al., 2009), was used as inputs for parameterizing the GeoSail model, scaling up the spectral library from the leaf to the canopy level. A LUT was built to link 30 reference spectra with burn severity GeoCBI values from 0 to 3 (De Santis et al., 2009). To facilitate the application of the LUT to Landsat TM bands, each of the spectra in the LUT was convolved to the Landsat spectral resolution, using a Gaussian model with a

full width at half maximum (FWHM) appropriate for the TM band spacing (Mutanga et al., 2015).

2.4.1.2. LUT for diseased trees

We built a LUT for diseased trees by taking advantage of the AVIRIS data acquired in our study area. We overlaid field-measured plots on the AVIRIS image and extracted GeoCBI values from the plots and the corresponding spectra from the image. This information was used to create a LUT linking 39 spectra with 39 GeoCBI values in diseased forests. Among a total of 42 plots identified to be affected by sudden oak death in the field, three plots were removed because they were not covered by the AVIRIS image. Subsequently, the spectra in the LUT were convolved to the Landsat TM spectral resolution following the same method as described in Section 2.4.1.1.

2.4.2. Pre-fire fractional mapping

2.4.2.1. Spectral library

We constructed a spectral library for pre-fire fractional mapping. Here, we applied AVIRIS data to identify endmembers for green vegetation (GV) and non-photosynthetic vegetation (NPV), representing healthy and diseased trees, respectively. Because the AVIRIS sensor was flown after fire occurrence, endmember extraction was conducted in the areas outside the fire scar. Specifically, we applied the Pixel Purity Index (PPI; Boardman et al., 1995) algorithm to identify a pool of potential endmember pixels in the AVIRIS image. PPI is an iterative process, in which every pixel is repeatedly projected onto a random vector selected through the n-dimensional scatter plot (n=224 in our study), and pixels are considered pure if they consistently fall into the

tails of the calculated histograms. After the initial assessment, the number of endmembers was further reduced using the three techniques proposed by Roberts et al. (2003), Dennison and Roberts (2003), and Dennison et al. (2004): Count based Endmember Selection (CoB), Endmember Average RMSE (EAR), and Minimum Average Spectral Angle (MASA). To do so, we selected the endmembers that modeled the greatest number of endmembers within their classes using CoB. When EAR was considered, we chose endmembers that yielded the lowest RMSE within each class. In addition, we identified the endmembers with the lowest average spectral angle when MASA was taken into account. The final endmembers were selected to satisfy all of the three criteria: highest COB, lowest EAR and lowest MASA. Using the Visualization and Image Processing for Environmental Research (VIPER) Tools package (Roberts et al., 2007), we developed a spectral library, including 6 spectra for GV, 5 spectra for NPV, 6 spectra for soil, and 1 spectrum for shade. Finally, all the AVIRIS spectra were convolved to the Landsat TM spectral resolution.

2.4.2.2. Fractional mapping

Using the endmember spectral library and the MESMA model, we decomposed each pixel in the pre-fire Landsat image into GV (healthy tree), NPV (diseased tree), soil, and shade fractions. The parameters for calibrating MESMA included minimum and maximum allowable fraction values for each class, maximum shade fraction, and RMSE. In this project, we chose −0.05 and 1.05 for minimum and maximum allowable fraction values, respectively, 0.8 for maximum allowable shade fraction value, and 0.025 for maximum allowable RMSE, following the recommendations by Dennison and Roberts (2003). Here, the minimum and maximum possible values were allowed to be slightly

less than 0 or slightly greater than 1, because the precision of sub-pixel fraction estimation is typically limited by the Modular Transfer Function (MTF) of Landsat sensor; and the spectral signal for a given pixel is partially influenced by the land cover of surrounding pixels (Forster, 1985; Townshend et al., 2000). While multiple models met the above-mentioned criteria, the model with the lowest RMSE was selected. Then, the MESMA derived three types of fractional (GV, NPV, and soil) maps. Finally, three relative abundance images of non-shade endmembers with values ranging from 0 to 1 were obtained. We employed VIPER to complete the MESMA procedures (Roberts et al., 2007).

2.4.3. Burn severity mapping

Burn severity mapping was carried out using the post-fire Landsat TM image based on an assumption that burn severity in each pixel (covered by a mixture of healthy and diseased trees) is a linear combination of burn severity for two tree classes – healthy and diseased trees, weighted by their areal fractions. To determine the burn severity value for each class, it is also assumed that the spectral reflectance of each burned pixel is the linear combination of reflectance spectra of burned canopies from healthy and diseased trees, weighted by their areal fractions (Eq. 2).

$$Reflectance_{i,j} = Spectrum^{i}_{\text{Healthy}} \times F_{\text{Healthy}} + Spectrum^{j}_{\text{Diseased}} \times F_{\text{Diseased}} \quad (2)$$

where $spectrum^{i}_{\text{Healthy}}$ represents the *i*th spectrum (range: 1 to 30) from the reference spectra in the healthy tree LUT (Section 2.4.1.1), F_{Healthy} is the pre-fire fraction of healthy trees in the pixel area (Section 2.4.2), $spectrum^{j}_{\text{Diseased}}$ represents the *j*th spectrum (range: 1 to 39) from the reference spectra in the diseased tree LUT (Section

2.4.1.2), and F_{Diseased} is the pre-fire fraction of diseased trees in the pixel area (Section 2.4.2).

To determine the two optimal spectra (one for healthy trees and one for diseased trees), we evaluated all 1170 spectral combinations (30×39). Each of the calculated reflectance spectra from Eq. 2 was compared with the reflectance of the corresponding Landsat pixel (at the same location) using the Spectral Angle Mapper algorithm (SAM; Kruse et al., 1993). Here, SAM measures the similarity (i.e., angle) between the calculated and the observed spectral reflectance across Landsat TM bands. SAM has proven effective in forest burn severity assessment due to its simplicity and insensitivity to differences in illumination (De Santis et al., 2009). The optimal spectra were chosen when the simulated reflectance reached the highest similarity with the observed reflectance, among all the tested spectral combinations. Consequently, the corresponding GeoCBI values were derived from the two LUTs. The estimated burn severity for each pixel area is the linear combination of burn severity of healthy and diseased trees, weighted by their areal fractions (Eq. 3). This is based on an assumption that the actual burn severity from a burned plot should be aggregated using the same proportions of healthy and diseased trees.

$$Burn\ severity = GeoCBI_{\text{Healthy}} \times F_{\text{Healthy}} + GeoCBI_{\text{Diseased}} \times F_{\text{Diseased}} \quad (3)$$

where $GeoCBI_{\text{Healthy}}$ represents burn severity of healthy trees, $GeoCBI_{\text{Diseased}}$ represents burn severity of diseased trees, F_{Healthy} is the fraction of healthy trees within each pixel, and F_{Diseased} is the fraction of diseased trees within each pixel.

For model calibration and validation, Leave-One-Out-Cross-Validation (LOOCV) was applied due to the limited number of field-measured diseased plots (39 plots). Specifically, for each round of evaluation, one observation was left out for model performance evaluation (computing RMSE), while the remainder was used for building the diseased tree LUT.

2.4.4. Infection stage mapping

Depending on the invasion stages of sudden oak death, an infected forest landscape may show three major symptoms (Meentemeyer et al., 2008; Chen et al., 2015a): (i) early-stage (host trees retaining their dried foliage and fine twigs for one year or more), (ii) middle-stage (some older mortality with host trees losing fine crown fuels and surface fuels beginning to accumulate for 1-3 years), and (iii) late-stage (host trees being dead for over 4 years and causing gaps due to trees falling over). To understand the infection stages in the studied forest landscape at the time of fire occurrence, we employed the sudden oak death-caused tree mortality maps from a previous project (He et al., 2019). In that project, MESMA was used to extract NPV fractions from Landsat TM annual time series. The results were refined using Species Distribution Modeling (SDM) that simulated the statistical probability of sudden oak death dispersal patterns over space and time, leading to annual map accuracies from 74.24% to 82.50%. In our study, we referenced the annual disease maps and divided the diseased trees into three infection stages following three criteria: (1) all of the trees that had been killed in or prior to 2005 were identified as the late stage; (2) the infection that occurred in 2006 and 2007 was identified as the middle stage; and (3) the newly detected infection in 2008 was identified as the early stage. The mapping result was validated using field-measured data,

with overall accuracy, producer's accuracy, user's accuracy, and kappa statistic reported in this study.

2.4.5. Burn severity assessment with NBR, dNBR and RdNBR

For the purpose of comparison, we calculated popular remote sensing spectral indices (i.e., NBR, dNBR and RdNBR) for burn severity estimation. Particularly, dNBR and RdNBR take into consideration the pre- and post-fire spectral reflectance, which are also used in DWAM. To do so, we applied the following equations to calculate these indices (López-García and Caselles, 1991; Key and Benson, 2006; Miller and Thode, 2007).

$$\mathrm{NBR} = \frac{\mathrm{B_4} - \mathrm{B_7}}{\mathrm{B_4} + \mathrm{B_7}} \tag{4}$$

$$\mathrm{dNBR} = \mathrm{NBR_{Pre-fire}} - \mathrm{NBR_{Post-fire}} \tag{5}$$

$$\mathrm{RdNBR} = \frac{\mathrm{NBR_{Pre-fire}} - \mathrm{NBR_{Post-fire}}}{\sqrt{\mathrm{ABS}(\mathrm{NBR_{Pre-fire}}/1000)}} \tag{6}$$

where B_4 and B_7 are the spectral reflectance of band 4 (near-infrared, NIR) and band 7 (short wave infrared, SWIR) of Landsat TM, respectively. Then, we developed linear regression models linking individual spectral indices with GeoCBI, with R^2 and RMSE reported.

2.5. Results

2.5.1. Spectral libraries

The average spectral reflectance for burned trees (a – healthy; b – diseased) is presented in Fig. 2.3. We also divided burn severity into five main intervals, i.e., GeoCBI ∈ [0, 1.0), [1.0, 1.5), [1.5, 2.0), [2.0, 2.5], and (2.5, 3.0]. In most cases, the reflectance

curves show similar patterns for both diseased and healthy trees (Fig. 2.3), where wildfire reduces forest spectral reflectance with the increase of burn severity from the visible to the near-infrared portion of the spectrum. However, burn severity leads to a higher variation of spectral reflectance in healthy trees than in diseased trees, particularly when GeoCBI values are larger than 1.0 (Fig. 2.3). In the shortwave infrared portion of the spectrum, the patterns are different. For diseased trees, varying levels of burn severity result in noticeable differences in reflectance curves. However, for healthy trees, the spectral reflectance corresponding to two medium-high burn severity intervals (GeoCBI $\in$ [1.5, 2.0), [2.0, 2.5]) show similar reflectance. In the same shortwave infrared portion, we further found a stronger effect of medium-low burn severity [GeoCBI $\in$ [1.0, 1.5)] on diseased trees than healthy trees, resulting in lower spectral reflectance.

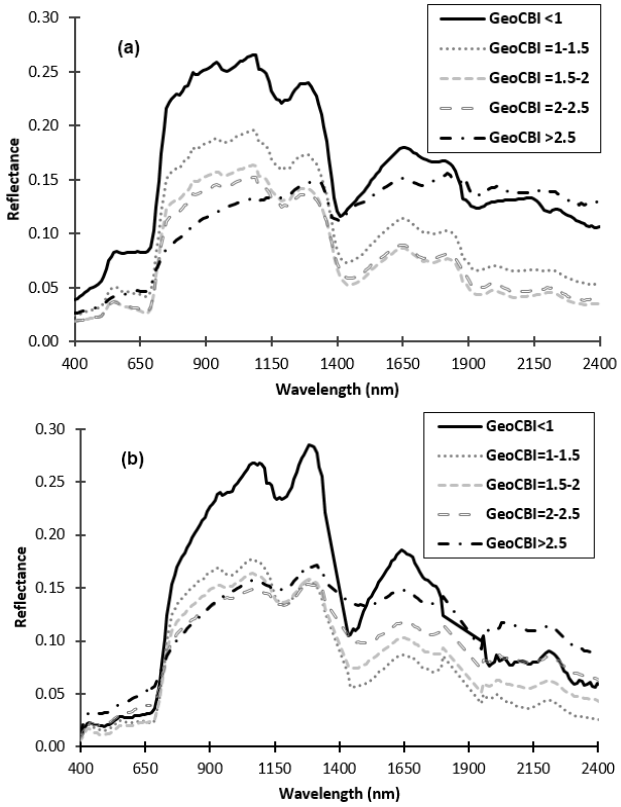

Fig. 2.3 Average spectral reflectance corresponding to the main intervals of GeoCBI for (a) healthy and (b) diseased trees. Healthy tree spectra were derived from De Santis and Chuvieco (2009).

To facilitate calculating pre-fire fractions for healthy and diseased trees, we extracted 6 GV, 5 NPV, and 6 soil endmembers (see methods in Section 2.4.2.1), with their spectra shown in Fig. 2.4. We found a high intra-class spectral variability among GV endmembers, possibly due to the high variety of tree species types (e.g., mixed oak woodlands and mixed coniferous forests) in the study area. In contrast, the spectral signatures from disease-affected trees (i.e., NPV reflectance) and soil are relatively homogeneous.

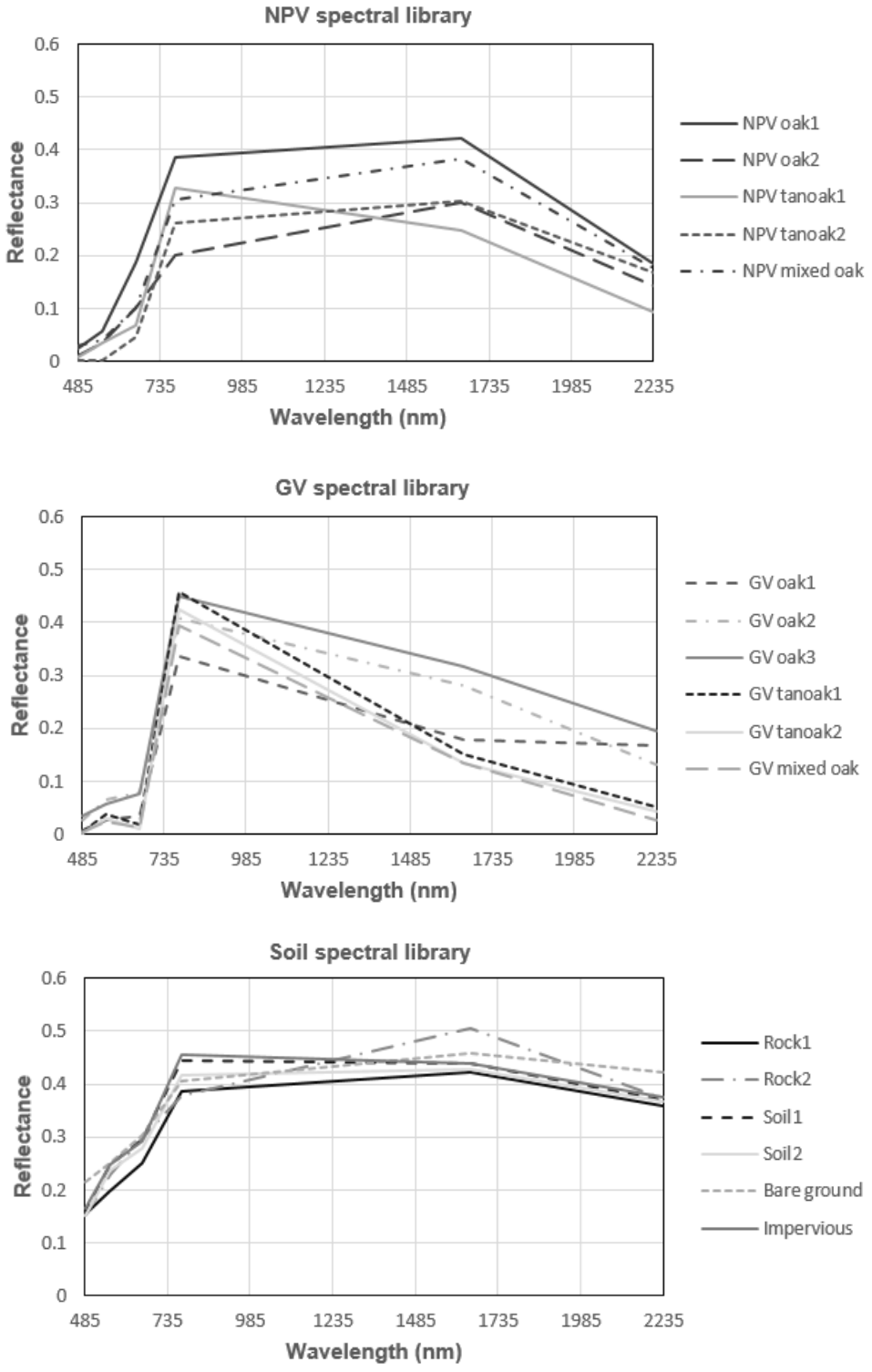

Fig. 2.4 The extracted endmember spectra for green vegetation (GV), non-photosynthetic vegetation (NPV), and soil.

2.5.2. Fraction maps

The shade normalized fraction maps corresponding to the three endmembers – GV, NPV, and soil are illustrated in Fig. 2.5, where light colors represent high fractions and dark colors show low fractions. High values in the NPV fraction map mainly distribute along the west coast, which is consistent with the findings by Chen et al., (2017), who used one-meter resolution KOMPSAT-2 satellite data to map sudden oak death-caused tree mortality over the same area. However, a small portion of high-value pixels was observed to spread all over the region, suggesting an overestimation of disease occurrence by only using NPV as the proxy of disease-caused tree mortality.

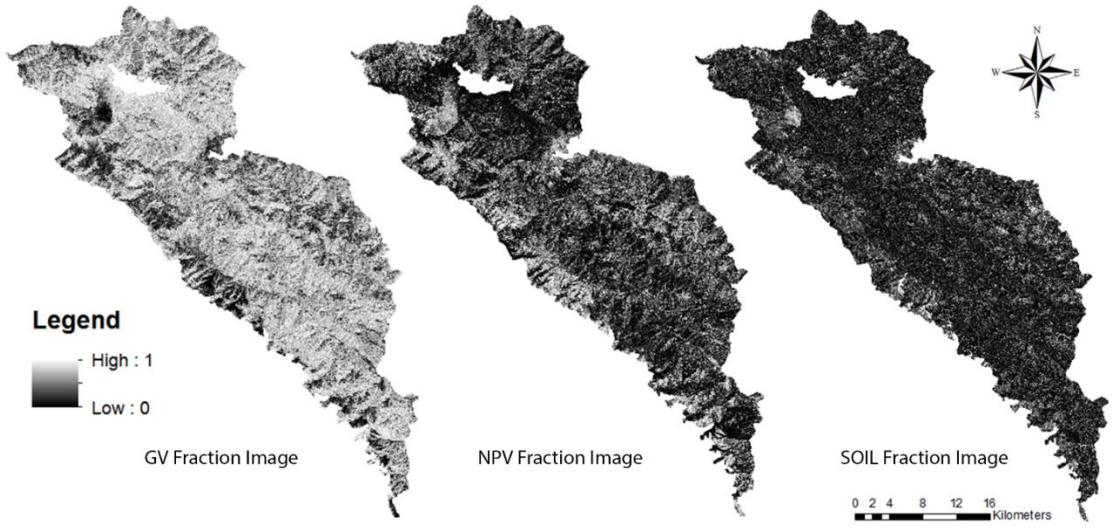

Fig. 2.5 Fraction maps of green vegetation (GV), non-photosynthetic vegetation (NPV), and soil derived from the pre-fire Landsat image, where values range from low (black tone) to high (light tone).

2.5.3. Burn severity maps

We generated two types of burn severity maps. For the first one, we assumed that all the trees were in the similar, healthy conditions prior to fire occurrence (i.e., the

fractions of disease-affected trees were assigned value ‘0’ in DWAM). For the second one, we considered the disease effects using the proposed model DWAM. For simplicity purposes, the resulting burn severity maps were named as non-DWAM map (not considering disease) and DWAM map (considering disease). Both maps are dominated by moderate ($1.5 \leqslant$ GeoCBI <2.5) to severe burns ($2.5 \leqslant$ GeoCBI $\leqslant 3.0$). While severe burns dominate the non-DWAM map with a spatial coverage of 78.9% (Fig. 2.6a), they only account for 27.3% in the DWAM map (Fig. 2.6b), in which moderate burns dominate (66.6%).

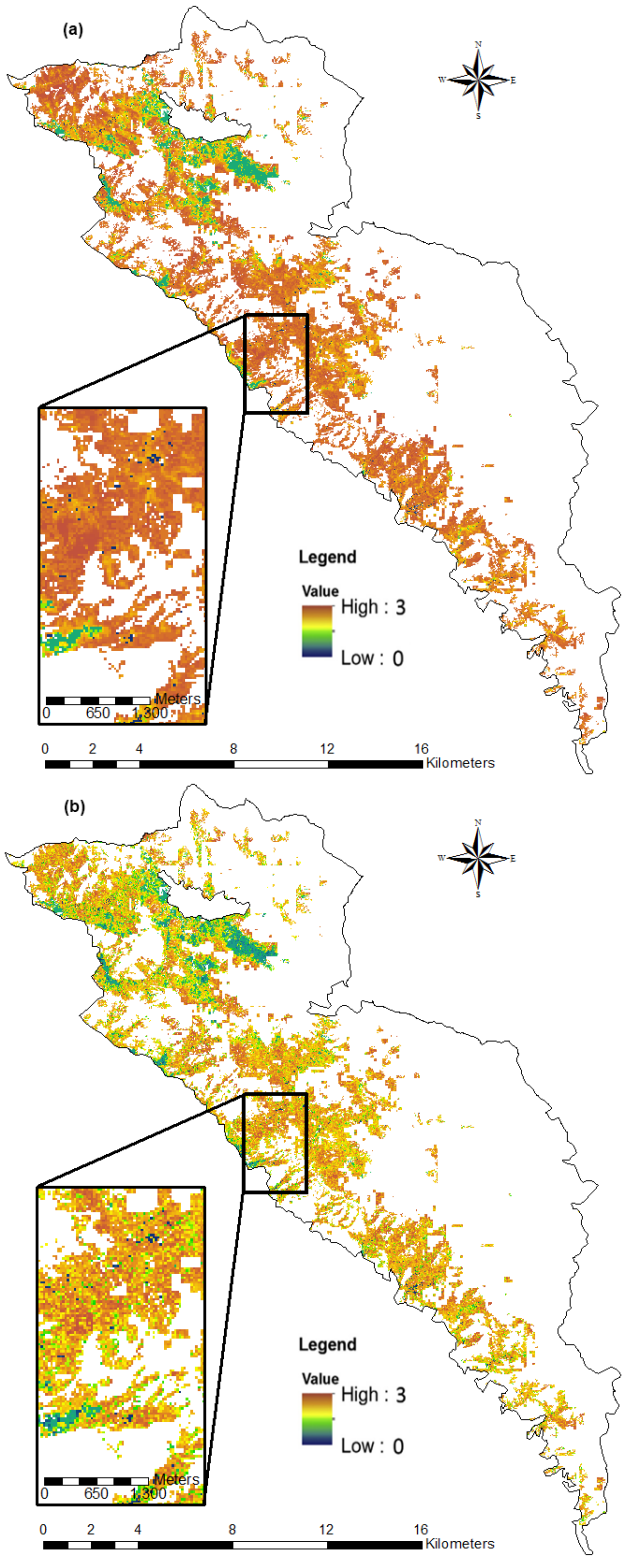

Fig. 2.6 Burn severity maps (a) without considering the effects of sudden oak death, and (b) considering the disease effects using DWAM.

We further compared field-measured and estimated GeoCBI values using two scatter plots in Fig. 2.7. Similar to the findings as illustrated in Fig. 2.6, ignoring the effects of disease on burn severity modeling caused an evident overestimation with a relatively large error (RMSE=0.62; Fig. 2.7(2)). Using the proposed model, we were able to reduce the error (RMSE) to 0.36, a 42% decrease (Fig., 2.7(1)). We also found that the proposed DWAM can reduce the overestimation of burn severity in both moderately and severely burned plots (Fig. 2.6).

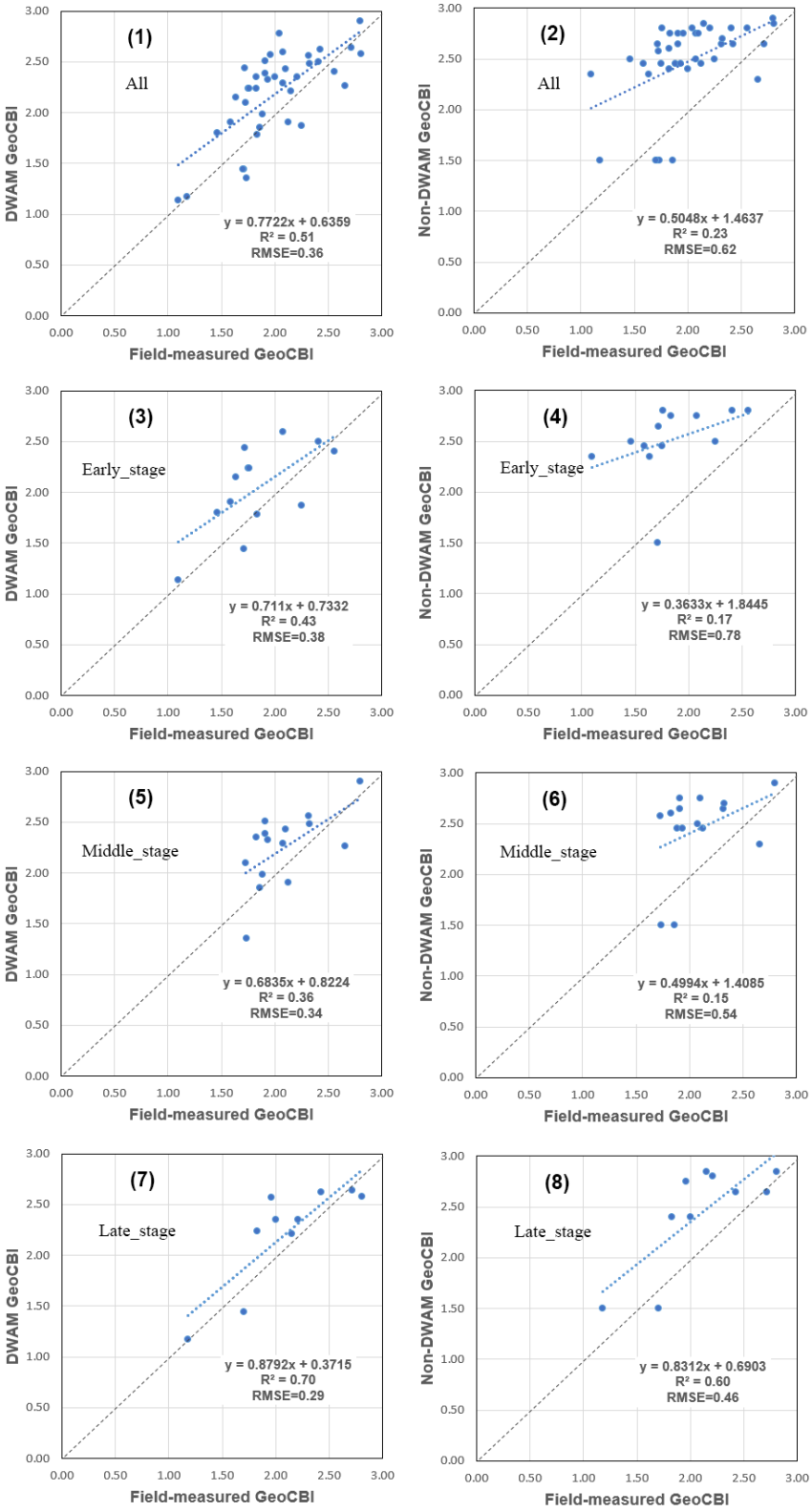
(1)
All
y = 0.7722x + 0.6359
R² = 0.51
RMSE=0.36
DWAM GeoCBI
Field-measured GeoCBI
(2)
All
y = 0.5048x + 1.4637
R² = 0.23
RMSE=0.62
Non-DWAM GeoCBI
Field-measured GeoCBI
(3)
Early_stage
y = 0.711x + 0.7332
R² = 0.43
RMSE=0.38
DWAM GeoCBI
Field-measured GeoCBI
(4)
Early_stage
y = 0.3633x + 1.8445
R² = 0.17
RMSE=0.78
Non-DWAM GeoCBI
Field-measured GeoCBI
(5)
Middle_stage
y = 0.6835x + 0.8224
R² = 0.36
RMSE=0.34
DWAM GeoCBI
Field-measured GeoCBI
(6)
Middle_stage
y = 0.4994x + 1.4085
R² = 0.15
RMSE=0.54
Non-DWAM GeoCBI
Field-measured GeoCBI
(7)
Late_stage
y = 0.8792x + 0.3715
R² = 0.70
RMSE=0.29
DWAM GeoCBI
Field-measured GeoCBI
(8)
Late_stage
y = 0.8312x + 0.6903
R² = 0.60
RMSE=0.46
Non-DWAM GeoCBI
Field-measured GeoCBI

Fig. 2.7 Comparisons between field-measured and estimated GeoCBI (2,4,6,8) without considering the effects of sudden oak death, and (1,3,5,7) considering the disease effects using DWAM across all the infected plots, and the plots at the early-, middle-, and late-stage infection, respectively.

Table 2.1 provides summary statistics (area, percentage, minimum, maximum, mean, median and standard deviation) of the estimated burn severity at three levels (low, moderate and high) using non-DWAM and DWAM. Overall, DWAM considers that the majority of the area was subject to moderate burn severity, while the area is considered to be heavily burned with non-DWAM.

Table 2.1 Summary statistics of the estimated burn severity using non-DWAM and DWAM.

Burn severity		Area (ha)	Percentage (%)	Minimum	Maximum	Mean	Median	Standard deviation
Non-DWAM	Low	60.5	0.7	0.00	1.00	0.74	1.00	0.33
	Moderate	1720.8	20.4	1.50	2.45	2.07	2.30	0.39
	High	6691.5	78.9	2.50	3.00	2.71	2.75	0.11
DWAM	Low	509.6	6.1	0.00	1.49	1.31	1.40	0.23
	Moderate	5627.7	66.6	1.50	2.49	2.21	2.27	0.22
	High	2314.1	27.3	2.50	2.99	2.62	2.60	0.09

2.5.4. Infection stage map

The overall accuracy of mapping the stages of sudden oak death infection is 69.84%, with a Kappa coefficient of 0.58. As presented in Table 2.2, the producer's accuracies of diseased forest across the three progression stages are high (early-stage: 81.81%, middle-stage: 81.25%, late-stage: 85.71%), while the corresponding user's accuracies are relatively lower (early-stage: 64.28%, middle-stage: 76.47%, late-stage: 54.54%). This indicates a slight overestimation of disease infection. Trees may have

been affected by both sudden oak death and other disturbances (e.g., drought and strong wind). Especially at the late stage, tree gaps may be filled with trunks, branches, leaves and/or low-level, live vegetation (e.g., shrubs). The symptom of infestation was not as apparent as that at the early-middle stages (see a review by Chen and Meetemeyer, 2016), increasing uncertainties in disease mapping. Although the disease progression map contains errors, it did not affect burn severity modeling in our study and serves as valuable baseline data for assessing the performance of our model across stages of disease progression.

Table 2.2 Confusion matrix for the infection stage mapping result.

User Class	Reference Class					
	Healthy Forest	Early-stage	Middle-stage	Late-stage	Total	Producer's Accuracy (%)
Healthy Forest	16	5	3	3	27	59.25
Early-stage	2	9	0	0	11	81.81
Middle-stage	1	0	13	2	16	81.25
Late-stage	0	0	1	6	7	85.71
Total	19	14	17	11	61	
User's Accuracy (%)	84.21	64.28	76.47	54.54		

Overall accuracy = 69.84%; Kappa statistic = 0.58

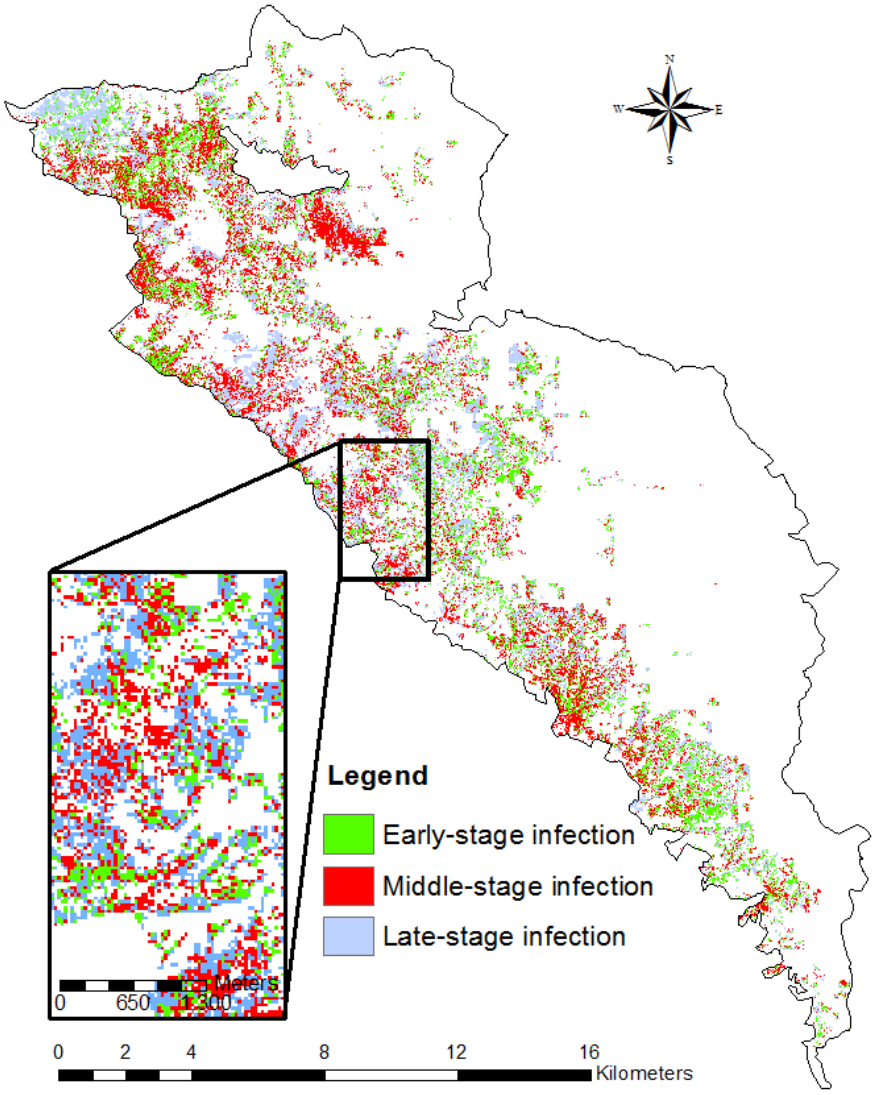

Fig. 2.8 Forest disease infection map showing early-, middle-, and late-stage disease progression.

2.5.5. Performance of NBR, dNBR and RdNBR

We compared field-measured GeoCBI values with those estimated by NBR, dNBR, and RdNBR using scatter plots in Fig. 2.9. In most cases (except the middle-stage infestation), dNBR and RdNBR that account for the spectral difference between pre- and post-fire conditions reveal better fitting performance and smaller errors than NBR that uses only post-fire data across stages of disease progression. The performance of dNBR

and RdNBR are comparable. While dNBR shows a better agreement (higher R^2 and smaller RMSE) with GeoCBI at the early stage of infestation, RdNBR offers a relatively better solution in burn severity estimation at the middle and late stages (Fig. 2.9).

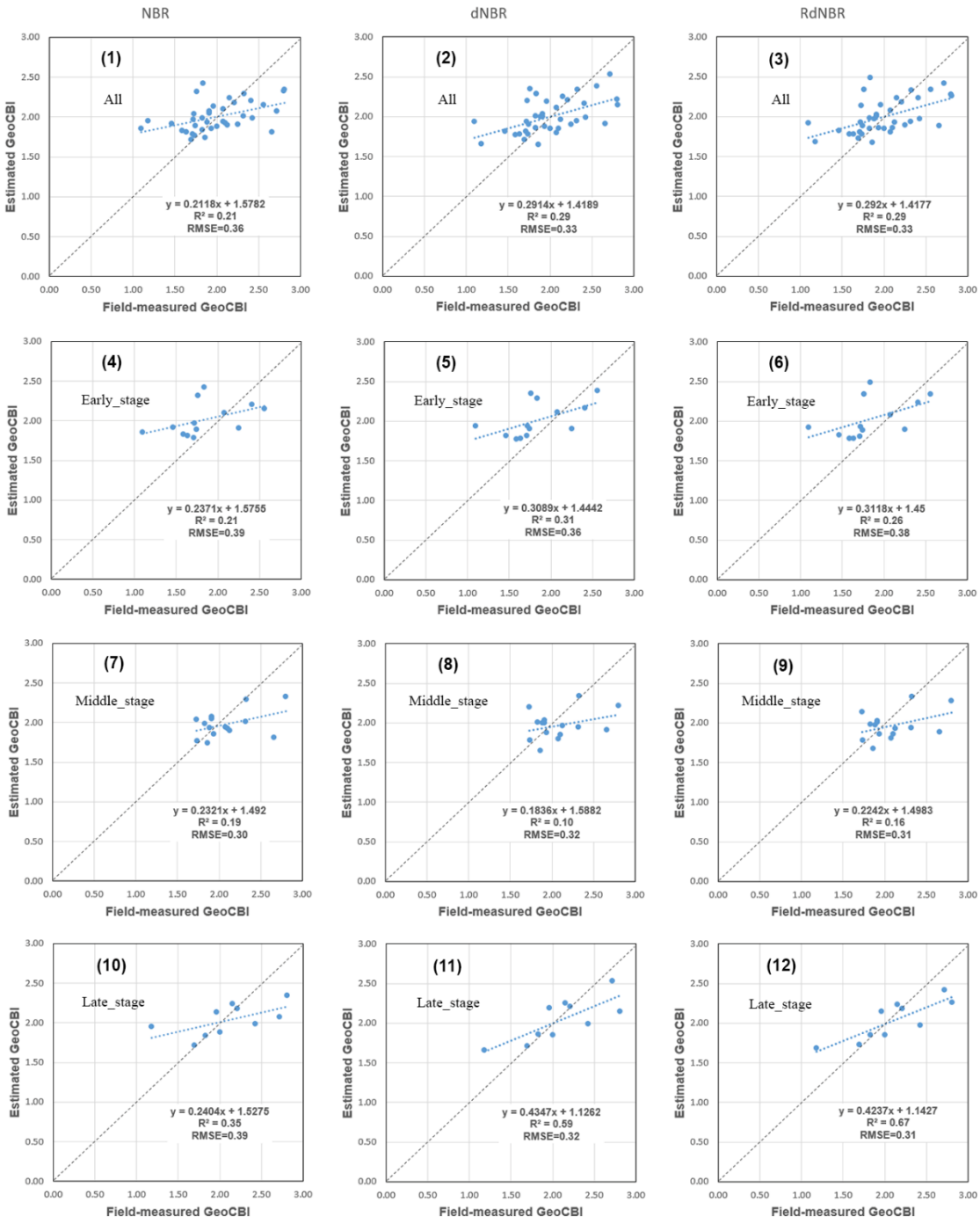

Fig. 2.9 Comparisons between field-measured GeoCBI and NBR-, dNBR-, RdNBR-based GeoCBI across all the disease infected plots, and the plots at the early-, middle-, and late-stage infection, respectively.

2.6. Discussion

2.6.1. Assessment of burn severity mapping

The evaluation of DWAM and non-DWAM maps (Fig. 2.7) suggests an overestimation of burn severity if pre-fire disease disturbances are not considered in modeling. In fact, the comparison between the two maps is equivalent to the comparison between our model and the physical simulation model proposed by De Santis et al. (2009). This is because when disease fractions are treated as zeros, DWAM only relies on the spectral library and LUT developed for healthy trees, using the same inputs and procedure as those in De Santis's radiative transfer modeling framework (De Santis et al., 2009). Their framework has proven effective in areas that did not contain intensive disease disturbances (e.g., De Santis et al., 2010). However, in our study site, the high spectral similarity between diseased and burned tree patches (Hultquist et al., 2014) can possibly confuse the development of one single, accurate LUT linking burn severity and spectra, because a portion of diseased trees (burned or not) may be treated as being affected (or more severely affected) by fire. This is evidenced in Table 2.1, where the non-DWAM map contains 78.9% of severe burns (GeoCBI $\in$ [2.5, 3.0]); but the same level of burn severity only accounts for 27.3% in the DWAM map that has a higher estimation accuracy. Further because forest landscapes typically show various symptoms corresponding to different stages of disease progression (Meentemeyer et al., 2008), the relationship between spectra and burn severity becomes complicated as such relationship may vary from one disease-affected area to another. It is therefore meaningful and effective, as demonstrated in our study, to develop separate spectral libraries and LUTs for healthy and diseased trees in burn severity estimation.

Spectral mixture analysis (SMA) has been recently introduced in burn severity estimation (e.g., Veraverbeke et al., 2014; Quintano et al., 2017). So far, the main strategy is decomposing post-fire optical imagery (typically using MESMA) to extract NPV or char fractions at the sub-pixel level, which are statistically linked to burn severity. Although DWAM also utilizes SMA and MESMA, our model differs from the others by incorporating fractions of two broad tree classes (diseased and healthy trees) from pre-fire imagery. The fractions are used to identify the optimal spectrum for each of the two tree classes, and consequently, burn severity is estimated using the GeoCBI-spectrum LUTs. While this strategy is not as straightforward as directly extracting NPV or char fractions (e.g., Quintano et al., 2017), we circumvent the challenge of potentially obtaining large errors in post-fire image decomposition, because the disturbed trees by sudden oak death and fire demonstrate similarities in spectral reflectance (Hultquist et al., 2014).

Our model takes advantage of both pre- and post-fire Landsat imagery to quantify disease effects. This strategy is similar to several empirical approaches in the way that differentiates pre- and post-fire spectral indices, e.g., dNBR (Key and Benson, 2006) and RdNBR (Miller and Thode, 2007). While these spectral indices are able to capture the spectral variation caused by pre-fire disturbances, it becomes problematic to establish a robust statistical relationship between burn severity and the extracted spectral differences. For trees not affected by sudden oak death, the difference between pre- and post-fire spectral reflectance has been found to be positively correlated with burn severity, although such relationship may not be significant in diseased tree patches (Chen et al., 2015b). Based on the calculation of dNBR and RdNBR in this study, we found that

DWAM explained 51 percent of the variance in all the data, while each of the dNBR- and RdNBR-based models explained 29 percent (Fig 2.7 versus Fig. 2.9). It is also true for the three stages of disease progression, suggesting that DWAM can better capitalize on the pre- and post-fire imagery to fit the data than using the spectral-index-based approach in our study area. As Metz et al. (2011) and Chen et al. (2017) pointed out, sudden oak death-caused increases in surface fuels may reduce a tree's resistance to fire and in turn lead to high burn severity. This suggests that with the occurrence of sudden oak death, the pre- and post-fire spectral differences for diseased trees are possibly smaller than those of their healthy counterparts, possibly underestimating burn severity (Fig. 2.9). Uncertainties are further introduced by various symptoms of tree mortality corresponding to multiple stages of infection, leading to a weak statistical relationship between spectral indices and burn severity. This is particularly true for the early or middle stage of infestation, where the pre- and post-fire spectral similarity is higher than that at the late stage. Finally, the spectral-index-based approach is empirically-based, which typically requires new field data for model training at a new site or human interventions for determining the thresholds of burn severity classes (Eidenshink et al., 2007). Field data in our model are mainly used for developing GeoCBI-spectrum LUTs. Our model has the potential to be directly used in an area having similar tree species types and disturbances, i.e., similar LUTs, as ours. However, the spectral-index-based approach is more mature and has been widely used at regional to national scales, such as the United States' MTBS (Monitoring Trends in Burn Severity) program (https://www.mtbs.gov). Thorough evaluations on DWAM are expected before our model is applicable to large areas.

2.6.2. Performance of burn severity mapping across stages of disease progression

The results from DWAM and non-DWAM maps were both found to be stage-dependent (Table 2.3 and 2.4). Compared to the other two stages, the late stage contains more trees that suffered from severe burns (Table 2.3). Despite the errors in mapping stages of sudden oak death infection, at all stages, the non-DWAM map shows a consistent bias with the highest proportion of severely burned landscape (80.9% for the early stage, 72% for the middle stage, and 87.4% for the late stage; Table 2.3). In contrast, DWAM can reduce the overestimation of burn severity at all the three stages, resulting in a landscape dominated by moderate burns (Table 2.4). Particularly at the early and middle stages, a large portion of the study area, which is considered as highly burned in the non-DWAM map, is dominated by moderate burns in the DWAM map. This suggests that DWAM is more likely to show a superior performance in the areas where trees still retain fine twigs and large branches, i.e., trees were recently affected by the disease. This is in an agreement with our field experience and can be explained by the fact that diseased trees were mistreated as burned trees as a result of similar changes in biophysical or biochemical properties. Overall, forest responses to disturbances at various stages (e.g., disease progression) can introduce different levels of uncertainties in remote assessment of burn severity. Better understanding the spectrum-disturbance relationship, such as constructing a stage-based spectral library, may further improve the performance of burn severity mapping. However, such type of effort also leads to increased workloads and high costs in data acquisition.

Table 2.3 Summary statistics of the burn severity in forests across three types of forests: early-, middle-, and late-stage disease progression in the non-DWAM map.

Burn severity Non-DWAM		Area (ha)	Percentage (%)	Minimum	Maximum	Mean	Median	Standard deviation
Early Stage	Low	16.8	1.1	0.00	1.00	0.71	1.00	0.34
	Moderate	279.7	18.0	1.50	2.45	2.11	2.30	0.38
	High	1256.5	80.9	2.50	3.00	2.70	2.70	0.10
Middle stage	Low	15.3	0.7	0.00	1.00	0.75	1.00	0.32
	Moderate	588.3	27.3	1.50	2.45	1.97	2.0	0.41
	High	1552.5	72.0	2.50	3.00	2.71	2.75	0.11
Late stage	Low	5.6	0.3	0.00	1.00	0.61	0.50	0.37
	Moderate	256.4	12.3	1.50	2.45	2.04	2.20	0.39
	High	1820.5	87.4	2.50	3.00	2.76	2.80	0.10

Table 2.4 Summary statistics of the burn severity in forests across three types of forests: early-, middle-, and late-stage disease progression in the DWAM map.

Burn severity DWAM		Area (ha)	Percentage (%)	Minimum	Maximum	Mean	Median	Standard deviation
Early Stage	Low	84.3	5.4	0.00	1.49	1.25	0.39	0.29
	Moderate	1056.4	68.0	1.50	2.49	2.23	2.28	0.21
	High	412.9	26.6	2.50	3.00	2.60	2.58	0.08
Middle stage	Low	231.1	10.7	0.00	1.49	0.34	1.40	0.18
	Moderate	1408.3	65.3	1.50	2.49	2.19	2.25	0.23
	High	517.5	24.0	2.50	3.00	2.62	2.60	0.09
Late stage	Low	82.0	3.9	0.00	1.49	1.34	1.42	0.22
	Moderate	1232.1	59.2	1.50	2.49	2.22	2.27	0.21
	High	768.0	36.9	2.50	3.00	2.63	2.62	0.09

2.7. Conclusions

Forest ecosystems are facing a variety of disturbances including fires and emerging infectious diseases. Especially when both fire and non-fire disturbances coexist, high uncertainties are introduced to the remote assessment of burn severity. In

this study, we developed a new model DWAM to accurately estimate burn severity by incorporating the effects of pre-fire, disease-caused tree mortality. Our burn severity estimation has an average error of 0.36, a 42% improvement as compared to the result without consideration of disease effects. We have further compared DWAM with popular spectral-index-based approaches using dNBR and RdNBR for the purpose of assessing the generalization capacity of DWAM. Our model's improvements were observed at all three stages of disease progression. While being developed at one study site, DWAM demonstrates several strengths making it potentially suitable for burn severity mapping in other regions. First, we have carefully selected a California study area for model development. The site features a representative Mediterranean climate and has been widely studied for forest disturbances, including disease and fire. Second, the model was developed to study the general fire-disease effect. The assumptions, input data and three model components are not tied to local environment of specific requirements. Third, DWAM has the potential to be calibrated in areas affected by another type of disease/insect disturbance, e.g., mountain pine beetle (Assal et al., 2014). The structure of DWAM remains the same. Field observations, hyperspectral imagery, and/or radiative transfer models can be used to build spectral libraries and LUTs for capturing the relationship between post-fire spectra and burn severity. However, we also note that the generalization potential of DWAM needs to be thoroughly evaluated at independent sites to ensure that the model is applicable to large-scale burn severity mapping.

Acknowledgments

This research was supported by the National Science Foundation (EF-0622770) as part of the joint NSF-NIH Ecology and Evolution of Infectious Disease program, the North Carolina Space Grant, and the University of North Carolina at Charlotte CLAS Junior Faculty Development Award. The authors also gratefully acknowledge financial support from the USDA Forest Service – Pacific Southwest Research Station, the Gordon & Betty Moore Foundation. We thank numerous contributors who provided vital field and laboratory support, including K. Aram, M. Beh, A. Brauer, M. Chan, R. Cobb, C, DeLong, W. Dillon, K. Frangioso, J. Geng, A. Hohl, H. Mehl, A. Oguchi, E. Paddock, K. Pietrzak, M. Vaclavikova, J. Vieregge, L. Waks and A. Wickland.

References

Assal, T. J., Sibold, J., Reich, R., 2014. Modeling a Historical Mountain Pine Beetle Outbreak Using Landsat MSS and Multiple Lines of Evidence. Remote Sens. Environ. 155, 275–288.

ASTER GDEM Validation Team, 2011. ASTER Global Digital Elevation Model Version 2 – Summary of Validation Results. Available online at http://www.jspacesystems.or.jp/ersdac/GDEM/ver2Validation/Summary_GDEM2_validation_report_final.pdf

Berk, A., Anderson, G.P., Acharya, P.K., Bernstein, L.S., Muratov, L., Lee, J., Fox, M., Adler-Golden, S.M., Chetwynd Jr., J.H., Hoke, M.L., Lockwood, R.B., Gardner, J.A., Cooley, T.W., Borel, C.C., Lewis, P.E., Shettle, E.P., 2006. MODTRAN5: 2006 update. In: Proceedings of SPIE - The International Society for Optical Engineering, p. 62331F.

Boardman, J.W., Kruse, F.A., Green, R.O., 1995. Mapping target signatures via partial unmixing of AVIRIS data. In: Summaries, Fifth JPL Airborne Earth Science Workshop. Jet Propulsion Laboratory, Pasadena, CA, pp. 23–26.

Bright, B.C., Hicke, J.A., Meddens, A.J.H., 2013. Effects of bark beetle-caused tree mortality on biogeochemical and biogeophysical MODIS products. J. Geophys. Res. Biogeosciences 118, 974–982.

Chen, G., He, Y., De Santis, A., Li, G., Cobb, R., Meentemeyer, R.K., 2017. Assessing the impact of emerging forest disease on wildfire using Landsat and KOMPSAT-2 data. Remote Sens. Environ. 195, 218–229.

Chen, G., Meentemeyer, R.K., 2016. Remote sensing of forest damage by diseases and

insects. In: Weng, Q. (Ed.), Remote Sensing for Sustainability. CRC Press, Taylor & Francis Group, Boca Raton, Florida, pp. 145–162.

Chen, G., Metz, M.R., Rizzo, D.M., Dillon, W.W., Meentemeyer, R.K., 2015a. Object-based assessment of burn severity in diseased forests using high-spatial and high-spectral resolution MASTER airborne imagery. ISPRS J. Photogramm. Remote Sens. 102, 38–47.

Chen, G., Metz, M.R., Rizzo, D.M., Meentemeyer, R.K., 2015b. Mapping burn severity in a disease-impacted forest landscape using Landsat and MASTER imagery. Int. J. Appl. Earth Obs. Geoinf. 40, 91–99.

Chen, G., Weng, Q., Hay, G.J. and He, Y., 2018. Geographic object-based image analysis (GEOBIA): emerging trends and future opportunities. GIScience Remote Sens. 55, 159-182.

Chuvieco, E., De Santis, A., Riaño, D., Halligan, K., 2007. Simulation Approaches for Burn Severity Estimation Using Remotely Sensed Images. J. Assoc. Fire Ecol. 3, 129–150.

Chuvieco, E., Riaño, D., Danson, F. M., & Martin, P., 2006. Use of a radiative transfer model to simulate the postfire spectral response to burn severity. Journal of Geophysical Research: Biogeosciences 111(G4), 1–15.

Dennison, P.E., Halligan, K.Q., Roberts, D.A., 2004. A comparison of error metrics and constraints for multiple endmember spectral mixture analysis and spectral angle mapper. Remote Sens. Environ. 93, 359–367.

Dennison, P.E., Roberts, D.A., 2003. Endmember selection for multiple endmember spectral mixture analysis using endmember average RMSE. Remote Sens. Environ.

87, 123–135.

De Santis, A., Asner, G.P., Vaughan, P.J., Knapp, D.E., 2010. Mapping burn severity and burning efficiency in California using simulation models and Landsat imagery. Remote Sens. Environ. 114, 1535–1545.

De Santis, A., Chuvieco, E., 2007. Burn severity estimation from remotely sensed data: performance of simulation versus empirical models. Remote Sens. Environ. 108, 422−435.

De Santis, A., Chuvieco, E., 2009. GeoCBI: a modified version of the composite burn index for the initial assessment of the short-term burn severity from remotely sensed data. Remote Sens. Environ. 113, 554–562.

De Santis, A., Chuvieco, E., Vaughan, P. J., 2009. Short-term assessment of burn severity using the inversion of PROSPECT and GeoSail models. Remote Sens. Environ. 113, 126−136.

Díaz-Delgado, R., Pons, X., 2001. Spatial patterns of forest fires in Catalonia (NE of Spain) along the period 1975-1995 analysis of vegetation recovery after fire. For. Ecol. Manage. 147, 67–74.

Eidenshink, J., Schwind, B., Brewer, K., Zhu, Z.-L., Quayle, B., Howard, S., 2007. A Project for Monitoring Trends in Burn Severity. Fire Ecology 3, 3–21.

ENVI, 2009. Atmospheric Correction Module: QUAC and FLAASH User's Guide, in Atmospheric Correction Module Version 4.7, Boulder, CO: ITT Visual Information Solutions, 2009. https://www.exelisvis.com/portals/0/pdfs/envi/Flaash_Module.pdf.

Fernandez-Manso, A., Quintano, C., Roberts, D.A., 2016. Burn severity influence on post-fire vegetation cover resilience from Landsat MESMA fraction images time

series in Mediterranean forest ecosystems. Remote Sens. Environ. 184, 112–123.

Forster, B., 1985. An examination of some problems and solutions in monitoring urban areas from satellite platforms. Int. J. Remote Sens. 6, 139–151.

French, N., Kasischke, E., Hall, R., Murphy, K., Verbyla, D., Hoy, E., Allen, J., 2008. Using Landsat data to assess fire and burn severity in the North American boreal forest region: an overview and summary of results. Int. J. Wildl. Fire 17, 443–462.

Green, R.O., Eastwood, M.L., Sarture, C.M., Chrien, T.G., Aronsson, M., Chippendale, B.J., Faust, J.A., Pavri, B.E., Chovit, C.J., Solis, M.S., Olah, M.R., Williams, O., 1998. Imaging spectroscopy and the airborne visible infrared imaging spectrometer (AVIRIS). Remote Sens. Environ. 65, 227–248

Hall, R.J., Freeburn, J.T., De Groot, W.J., Pritchard, J.M., Lynham, T.J., Landry, R., 2008. Remote sensing of burn severity: Experience from western Canada boreal fires. Int. J. Wildl. Fire 17, 476–489.

He, Y., Chen, G., Potter, C., Meentemeyer, R.K., 2019. Integrating multi-sensor remote sensing and species distribution modeling to map the spread of emerging forest disease and tree mortality. Remote Sens. Environ. 231, 111238.

Hudak, A. T., Brockett, B.H., 2004. Mapping fire scars in a southern African savannah using Landsat imagery. Int. J. Remote Sens. 25, 3231–3243.

Hultquist, C., Chen, G., Zhao, K., 2014. A comparison of Gaussian process regression, random forests and support vector regression for burn severity assessment in diseased forests. Remote Sens. Lett. 5, 723–732.

Jacquemoud, S., Baret, F., 1990. PROSPECT: A model of leaf optical properties spectra. Remote Sens. Environ. 34, 75–91.

Keeley, J.E., 2009. Fire intensity, fire severity and burn severity: A brief review and suggested usage. Int. J. Wildl. Fire 18, 116–126.

Key, C.H., Benson, N.C., 2005. Landscape assessment: ground measure of severity, the Composite Burn Index and remote sensing of severity, the Normalized Burn Ratio. In: FIREMON: Fire Effects Monitoring and Inventory System (D.C. Lutes, R.E. Keane, J.F. Caratti, C.H. Key, N.C. Benson and L.J. Gangi, Eds.), USDA Forest Service, Rocky Mountain Research Station, Gen. Tech. Rep. RMRS-GTR-164, Ogden, UT, pp. CD:LA1–LA51.

Key, C.H., Benson, N.C., 2006. Landscape assessment (LA) sampling and analysis methods. In: USDA Forest Service General Technical Report, RMRS-GTR-164-CD.

Kokaly, R.F., Rockwell, B.W., Haire, S.L., King, T.V.V., 2007. Characterization of post-fire surface cover, soils, and burn severity at the Cerro Grande Fire, New Mexico, using hyperspectral and multispectral remote sensing. Remote Sens. Environ. 106, 305–325.

Kruse, F.A., 2004. Comparison of ATREM, ACORN, and FLAASH Atmospheric Corrections Using low-Altitude AVIRIS Data of Boulder. CO. Jpl Airborne Geoscience Workshop.

Kruse, F.A., Lefkoff, A.B., Boardman, J.W., Heidebrecht, K.B., Shapiro, A.T., Barloon, P.J., Goetz, A.F.H., 1993. The spectral image processing system (SIPS)-interactive visualization and analysis of imaging spectrometer data. Remote Sens. Environ. 44, 145–163.

Kuusk, A., 2001. A two-layer canopy reflectance model, J. Quant. Spec- trosc. Radiat.

Transfer 71, 1–9.

Lentile, L.B., Holden, Z.A., Smith, A.M.S., Falkowski, M.J., Hudak, A.T., Morgan, P., Lewis, S.A., Gessler, P.E., Benson, N.C., 2006. Remote sensing techniques to assess active fire characteristics and post-fire effects. Int. J. Wildl. Fire 15, 319–345.

Lewis, S., Lentile, L., Hudak, A., Robichaud, P., Morgan, P., Bobbitt, M., 2007. Mapping ground cover using hyperspectral remote sensing after the 2003 Simi and Old wildfires in Southern California. Fire Ecology 3, 109–128.

López-García, M.J., Caselles, V., 1991. Mapping burns and natural reforestation using thematic mapper data. Geocarto Int. 1, 31–37.

Matthew, M.W., Adler-Golden, S.M., Berk, A., Felde, G., Anderson, G.P., Gorodetzky, D., Paswaters, S., Shippert, M., 2002. Atmospheric correction of spectral imagery: evaluation of the FLAASH algorithm with AVIRIS data. In: Proceedings of the 31st Applied Imagery Pattern Recognition Workshop. pp. 157–163.

Meentemeyer, R.K., Rank, N.E., Shoemaker, D.A., Oneal, C.B., Wickland, A.C., Frangioso, K.M., Rizzo, D.M., 2008. Impact of sudden oak death on tree mortality in the Big Sur ecoregion of California. Biol. Invasions 10, 1243–1255.

Meng, R., Wu, J., Schwager, K.L., Zhao, F., Dennison, P.E., Cook, B.D., Brewster, K., Green, T.M., Serbin, S.P., 2017. Using high spatial resolution satellite imagery to map forest burn severity across spatial scales in a Pine Barrens ecosystem. Remote Sens. Environ. 191, 95–109.

Metz, M.R., Frangioso, K.M., Meentemeyer, R.K., Rizzo, D.M., 2011. Interacting disturbances: Wildfire severity affected by stage of forest disease invasion. Ecol.

Appl. 21, 313–320.

Metz, M.R., Varner, J., Frangioso, K., 2013. Unexpected redwood mortality from synergies between wildfire and an emerging infectious disease. Ecology 94, 2152–2159.

Miller, J.D., Safford, H.D., Crimmins, M., Thode, A.E., 2009. Quantitative evidence for increasing forest fire severity in the Sierra Nevada and southern Cascade Mountains, California and Nevada, USA. Ecosystems 12, 16–32.

Miller, J.D., Thode, A.E., 2007. Quantifying burn severity in a heterogeneous landscape with a relative version of the delta normalized burn ratio (dNBR). Remote Sens. Environ. 109, 66–80.

Mutanga, O., Adam E., Adjorlolo C., Abdel-Rahman E.M., 2015. Evaluating the Robustness of Models Developed from Field Spectral Data in Predicting African Grass Foliar Nitrogen Concentration Using Worldview-2 Image as an Independent Test Dataset. Int. J. Appl. Earth Obs. Geoinf. 34, 178–187.

Painter, T. H., Dozier, J., Roberts, D. A., Davis, R. E., Green, R. O., 2003. Retrieval of subpixel snow-covered area and grain size from imaging spectrometer data. Remote Sens. Environ. 85, 64–77.

Painter, T. H., Roberts, D. A., Green, R. O., Dozier, J., 1998. The effect of grain size on spectral mixture analysis of snow-covered area from AVIRIS data. Remote Sens. Environ. 65, 320–332.

Quintano, C., Fernandez-Manso, A., Roberts, D.A., 2017. Burn severity mapping from Landsat MESMA fraction images and Land Surface Temperature. Remote Sens. Environ. 190, 83–95.

Quintano, C., Fernández-Manso, A., Roberts, D.A., 2013. Multiple Endmember Spectral Mixture Analysis (MESMA) to map burn severity levels from Landsat images in Mediterranean countries. Remote Sens. Environ. 136, 76–88.

Sonnentag, O., Chen, J. M., Roberts, D. A., Talbot, J., Halligan, K. Q., Govind, A., 2007. Mapping tree and shrub leaf area indices in an ombrotrophic peatland through multiple endmember spectral unmixing. Remote Sens. Environ. 109, 342–360.

Rizzo, D.M., Garbelotto, M., Hansen, E.M., 2005. Phytophthora ramorum: integrative research and management of an emerging pathogen in California and Oregon forests. Annu. Rev. Phytopathol. 43, 309–35.

Roberts, D.A., Dennison, P.E., Gardner, M.E., Hetzel, Y., Ustin, S.L., Lee, C.T., 2003. Evaluation of the potential of Hyperion for fire danger assessment by comparison to the airborne visible/infrared imaging spectrometer. IEEE Trans. Geosci. Remote Sens. 41, 1297–1310.

Roberts, D.A., Halligan, K., Dennison, P., 2007. VIPER Tools User Manual. V1.5.

Roberts, D.A., Gardner, M., Church, R., Ustin, S., Scheer, G., Green, R.O., 1998. Mapping chaparral in the Santa Monica Mountains using multiple endmember spectral mixture models. Remote Sens. Environ. 65, 267–279.

Roy, D. P., Boschetti, L., Trigg, S. N., 2006. Remote Sensing of Fire Severity: Assessing the Performance of the Normalized Burn Ratio. IEEE Geoscience and Remote Sensing Letters 3, 112–116.

Schmidt, G., Jenkerson, C., Masek, J., Vermote, E., Gao, F., 2013. Landsat ecosystem disturbance adaptive processing system (LEDAPS) algorithm description. U.S. Geological Survey Open-File Report 2013-1057. U.S. Geological Survey, Reston,

VA, p. 27 U.S. Geological Survey: Reston, VA. Available online: https://pubs.usgs.gov/of/2013/1057/

Shettle, E.P., Fenn, R.W., 1979. Models for the Aerosols of the Lower Atmosphere and the Effects of Humidity Variations on their Optical Properties. Environmental Research Papers Air Force Geophys. Lab., Bedford, Mass p. 94.

Townshend, J.R.G., Huang, C., Kalluri, S.N. V., Defries, R.S., Liang, S., Yang, K., 2000. Beware of per-pixel characterization of land cover. Int. J. Remote Sens. 21, 839–843.

Turner, M.G., Baker, W.L., Peterson, C.J., Peet, R.K., 1998. Factors Influencing Succession: Lessons from Large, Infrequent Natural Disturbances. Ecosystems 1, 511–523.

USDA Forest Service., 2008. Executive Summary: Basin Complex Fire/Indians Fire BAER Initial Assessment (16 pp.).

van Mantgem, P.J., Nesmith, J.C.B., Keifer, M., Knapp, E.E., Flint, A., Flint, L., 2013. Climatic stress increases forest fire severity across the western United States. Ecol. Lett. 16, 1151–1156.

Veraverbeke, S., Hook, S., Hulley, G., 2012. An alternative spectral index for rapid fire severity assessments. Remote Sens. Environ. 123, 72–80.

Veraverbeke, S., Stavros, E. N., Hook, S. J., 2014. Assessing fire severity using imaging spectroscopy data from the Airborne Visible/Infrared Imaging Spectrometer (AVIRIS) and comparison with multispectral capabilities. Remote Sens. Environ. 154, 153–163.

Verhoef, W., Bach, H., 2003. Simulation of hyperspectral and directional radiance

images using coupled biophysical and atmospheric radiative transfer models. Remote Sens. Environ. 87, 23–41.

Wen, J.G., Zhao, X.J., Liu, Q., Tang, Y., Dou, B.C., 2014. An improved land-surface albedo algorithm with DEM in rugged terrain. IEEE Geosci. Remote Sens. Lett. 11, 883–887.

Chapter 3: Effects of Wildfire on the Spread of Forest Disease Sudden Oak Death and Post-fire Forest Recovery

Abstract

While individual forest disturbances (wildfire and disease) are well studied, how disturbances interact with each other and change the spatial patterns of forest landscape are rarely quantified. In this study, we aim to analyze the role of wildfire in changing the spread pattern of Sudden Oak Death (SOD) in the Big Sur ecoregion of California. We used remote-sensing-derived products of post-fire burn severity and disease progression maps as the baseline data. We further analyzed the statistical relationship between burn severity and SOD progression for the burned and the unburned areas. Our findings reveal a significant role of wildfire in the spread of SOD. The rate of disease spread was negatively correlated with burn severity in burned forests, while it was found to be positively correlated with distance to fire boundaries outside of fire scars. Due to the synergistic effects of wildfire and SOD, the spatial patterns of the studied forest landscapes (edge density and isolation of healthy tree patches) were significantly altered even after eight years of fire occurrence when compared to the pre-fire status. Our study advances our understanding of the spatial interactions of forest disturbances, which can inform best management practices to improve forest resilience to those disturbances.

3.1. Introduction

Forest ecosystems are affected by environmental disturbances (e.g., emerging infectious disease and wildfire) at an unprecedented pace across spatial and temporal scales (Asner, 2013; Buma and Wessman, 2011). Understanding forest responses to

various disturbance regimes is pivotal to the short-/long-term projection of ecosystem dynamics, promoting informed decisions in sustainable forest resources management (Buma and Wessman, 2011; Daniel et al., 2017). Over the past decades, there have been a plethora of studies aiming to understand the effects of individual disturbances, such as disease- or insect-caused tree mortality (Dillon and Meentemeyer, 2019; Janousek et al., 2019; Pasquarella et al., 2017; Skowronek et al., 2017; Václavík and Meentemeyer, 2012), and post-fire burn severity (De Santis et al. 2009; He et al., 2019; Meng et al., 2017; Quintano et al., 2017). More recently, a growing number of studies have confirmed a novel trend of increasing intensities and frequencies of forest disturbances, which may interact with each other and jointly affect forest landscape dynamics in manners no one has anticipated (Jenkins et al., 2014; Simler et al., 2018; Turner, 2010).

To reduce forest vulnerability and improve best management practices, researchers have begun to examine how major disturbances interact and subsequently change tree mortality and their regeneration patterns, with an emphasis on two disturbance types – wildfire and disease/insect outbreak (Simler et al., 2018). One important research question that has yet to be fully answered is whether and how wildfire changes the spatial spread of forest disease or insect infestations. Depending on its severity, wildfire directly damages or removes the disease-/insect-infected host trees, which affects the survival of pathogens or insects in the fire (Beh et al., 2012). Recent studies also discovered that fire-stressed or moderately injured trees that were previously healthy are more susceptible than the unburned counterparts to insect attacks in the western United States (Jenkins et al., 2014; Powell et al., 2012). With new trees recover from the fire, disease or insect outbreaks likely re-occur in the forest (White et al. 1996).

Beh et al. (2012) found that although the occurrence of the plant disease Sudden Oak Death was reduced by wildfire, the disease-causing pathogen persisted in soil and some unburned vegetation. Similarly, Davis et al. (2012) discovered that the thick bark of pine trees can protest for bark beetles during wildfire. During the forest recovery stage, pathogen or insect intensity tends to increase under appropriate climate conditions and re-attack the forest, disturbing or altering its regeneration trajectory. While stand-replacing fires were found to reduce beetle mortality by limiting the abundance and distribution of host trees, forest resilience to interacting disturbances may also depend on landscape connectivity (Loehman et al., 2017), and dominant species composition (Sánchez-Pinillos et al., 2019). Consequently, forest structure and function exhibit high uncertainties during forest recovery (Bonan, 2008; Buma and Wessman, 2011; Canelles et al., 2019; Chambers et al., 2014; Coates et al., 2016; Gornish and Ambrozio dos Santos, 2016). While the aforementioned literature has provided preliminary knowledge about the effects of wildfire on disease or insect outbreak, most of the studies have relied on sparsely distributed samples collected from the field. This limits our capacity to analyze the spread patterns of disease or insect infestations, which is crucial for locating susceptible trees and promoting effective forest management (Beh et al., 2014; Kane et al., 2017).

Remote sensing offers a feasible solution to efficiently and repetitively monitor the impacts of forest disturbances in a synoptic view (Chen and Meentemeyer, 2016; Keeley, 2009; Hatala et al., 2010). It is especially suitable for understanding the spatially explicit patterns of forest mortality and disturbance progression (Chen et al., 2017). The estimation of disease- or insect-caused tree mortality using remotely sensed data makes

use of the spectral responses of damaged trees, such as altered spectral and spatial characteristics, which are distinct from their healthy counterparts (Lentile et al., 2006; Wulder et al., 2006; Keeley, 2009). The outbreak of forest disease/insect is typically chronic stress spanning years to decades. Satellite image time series has recently gained popularity to quantify spatiotemporal trajectories of infestations at the landscape level (e.g., Coops et al., 2010; Meigs et al., 2015). Fire effects on forests (i.e., burn severity) are typically mapped through comparing the pre- and post-fire spectral responses from the burned trees. Both statistical (e.g., linear regression and random forests; Hultquist et al., 2014) and physical models (e.g., radiative transfer model by integrating PROSPECT and GeoSail; De Santis et al., 2009) are viable solutions to burn severity estimation. While remote sensing data and products have demonstrated considerable benefits in forest management and research, their capacity to analyze interacting disturbances has been rarely evaluated (Chen and Meentemeyer, 2016).

The main goal of this study is to analyze the role of wildfire in changing the spread patterns of a forest disease Sudden Oak Death in the Big Sur, California ecoregion. Sudden Oak Death is a forest disease caused by the plant pathogen *Phytophthora ramorum*, which has led to substantial mortality of oak (*Quercus* spp.) and tanoak (*Notholithocarpus densiflorus*) trees since the mid-1990s (Rizzo et al., 2005). Extreme wildfire events co-occurred with the outbreak of Sudden Oak Death during the past decade, which offers an ideal opportunity to study the role of wildfire in changing the disease spread patterns. By taking advantage of remote-sensing-derived burn severity and Sudden Oak Death estimates, we asked two specific questions in this study: (i) Did wildfire significantly affect the spread rate of Sudden Oak Death? (ii) Following the

wildfire, whether and (if yes) how did Sudden Oak Death change forest fragmentation patterns during tree recovery?

3.2. Materials and methods

3.2.1. Study area

Our study was conducted in a forest ecosystem that has been affected by both wildfire and Sudden Oak Death. The study site (centered at 36°16' N, 121°44' W) is in the Big Sur ecoregion on the western flank of Santa Lucia Mountain of California with a total area of 80, 000 ha (Fig. 3.1). The area has a Mediterranean-type climate, experiencing two main seasons – cool wet season (November-April) and hot dry season (May-October), and a rugged landscape dissected by steep slopes and drainages with elevations ranging from sea level to 1,571 m within 5 km of the coast (Meentemeyer et al., 2008b). The environmentally complex region supports a diversity of plant communities, where the area is dominated by a range of tree species: (i) mixed coniferous forest, composing of ponderosa pine (*Pinus ponderosa*), sugar pine (*Pinus lambertiana*), Jeffrey pine (*Pinus jeffreyii*), coulter pine (*Pinus coulteri*), and Santa Lucia fir (*Abies bracteata*), which are located on upper elevation slopes and rocky ridges; and (ii) mixed oak woodland consisting of coast live oak (*Quercus agrifolia*), Shreve's oak (*Q. parvula*), bay laurel (*Umbellularia californica*), and madrone (*Arbutus menziesii*), which were found on moister slopes, giving way to riparian corridors of redwood-tanoak forest at lower elevations.

Since the mid-1990s, an invasive pathogen *Phytophthora ramorum* causing the disease – Sudden Oak Death – has led to extensive tree mortality in the study area mainly found in two plant communities – mixed oak and redwood-tanoak forests (Rizzo

et al., 2005). The disease involves a multi-year progress especially under suitable temperature and rainfall conditions, girdling a tree over years or making the tree more susceptible to attack by other pathogens or insects (Chen et al., 2015). In 2008, a wildfire – Basin Complex Fire – was ignited from a dry lightning storm in late June and burned over 28, 383 ha of federal, state and private lands. The fire divided our study area into burned (within the fire boundary) and unburned (outside the fire scar) areas (Fig. 3.1). The total cost of containment action was around $77.2 million mainly due to the sheer size of the fires, the ruggedness of the terrain and the extremely dry conditions (USDA Forest Service, 2008).

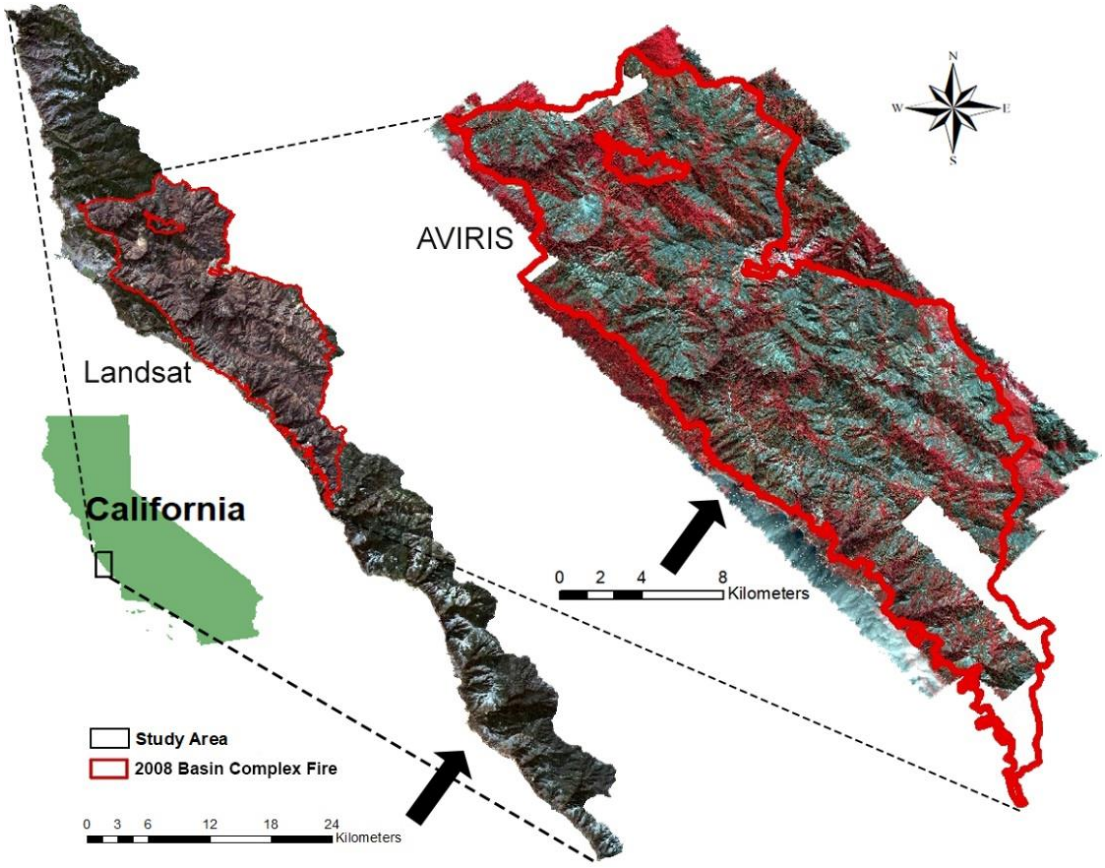

Fig. 3.1 Study area located in the Big Sur ecoregion on the western flank of the Santa Lucia Mountains in California. The extent of the 2008 Basin Complex Fire in the region

is outlined in red.The Landsat TM imagery was from a color composite using bands 3 (red), 2 (green) and 1 (blue). The AVIRIS (Airborne Visible InfraRed Imaging Spectrometer) image is from a color composite using bands 51 (NIR), 33 (Red), and 22 (Green).

3.2.2. Disease progression maps

We acquired disease-caused tree mortality maps annually (2005-2016) from a regional mapping project described by He et al. (2019b). The maps were created at the 30 m resolution based on a novel algorithm integrating remote sensing and species distribution modeling. Specifically, (i) spectral mixture analysis (Roberts et al., 1998) was first applied to the satellite Landsat time series (Wulder et al., 2012) for extracting disease-killed host candidates featuring isolated, patchy-distribution patterns. (ii) The uncertainties in the candidates were reduced by species distribution modeling which informed the likelihood of Sudden Oak Death's occurrence at specific locations. The maps demonstrate an annual disease infection rate of 7% from 2005 to 2016, with overall mapping accuracies ranging from 76% to 83%. The results indicate the spatial pattern of disease transmission from the west coast to the east (Fig. 3.2). Here, we did not use maps from 2009 to 2012 in our study, because of the high uncertainties in extracting diseased trees from the burned trees.

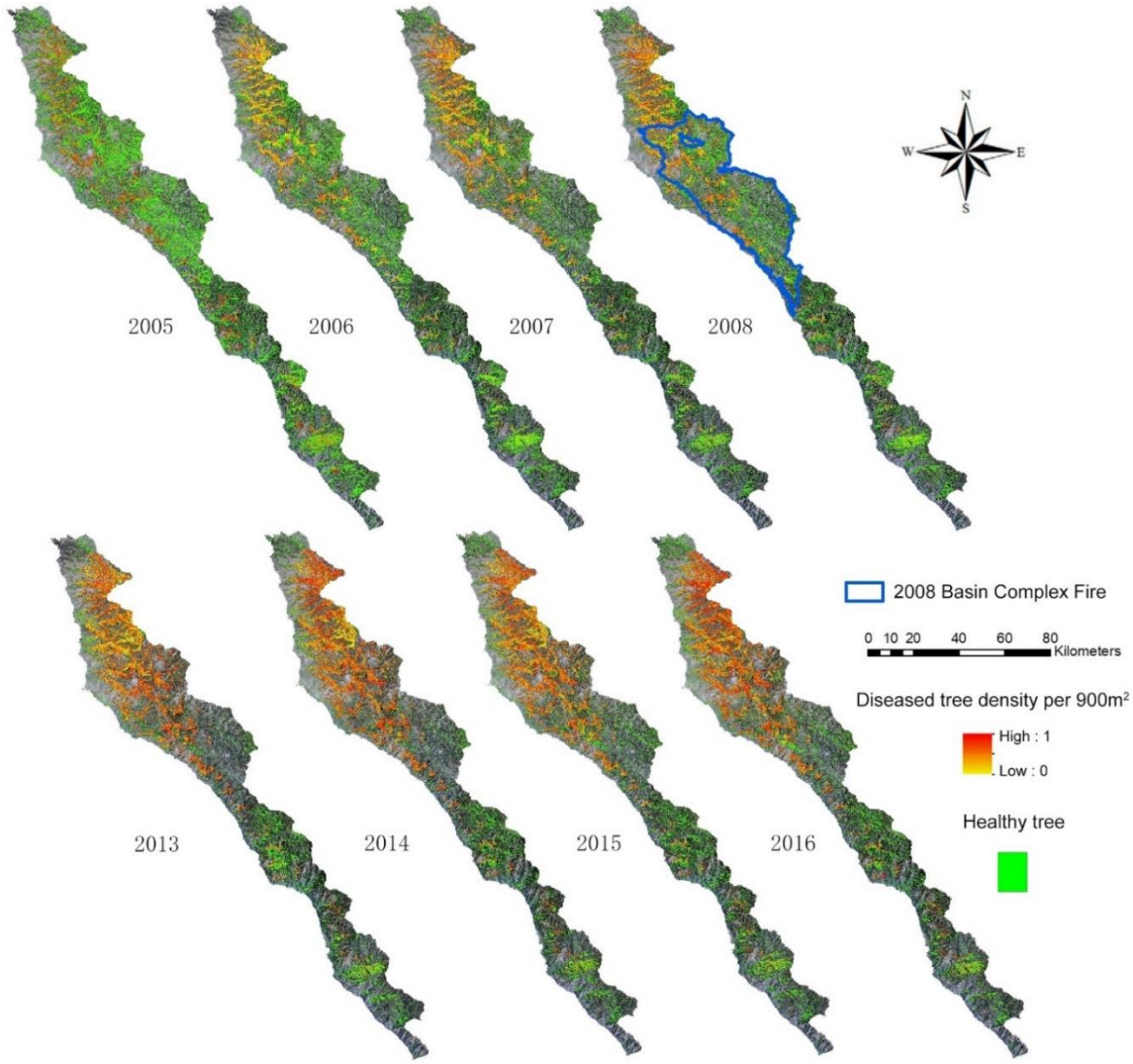

Fig. 3.2 Annual maps of tree mortality caused by Sudden Oak Death (2005-2008, 2013-2016).

3.2.3. Burn severity estimation

The burn severity map over the same area was produced by He et al. (2019a), who developed the Disturbance Weighting Analysis Model (DWAM) to intentionally estimate post-fire burn severity in the forest landscape that has been jointly affected by wildfire and Sudden Oak Death. DWAM treats burn severity in each basic mapping unit as a linear combination of burn severity of trees affected and not affected by the disease,

weighted by their areal fractions in each unit. Landsat and AVIRIS (Airborne Visible InfraRed Imaging Spectrometer) imagery (Green et al., 1998) were used to create the map at the 30 m resolution (Fig. 3.3), which is consistent with that of the disease maps.

The burn severity result has an average error of 0.36 measured in Geometrically structured Composite Burn Index (GeoCBI; De Santis and Chuvieco, 2009), which showed a 42% improvement as compared with results ignoring the existence of pre-fire forest disturbances (e.g., disease presence) in burn severity modeling (He et al., 2019a). The resulting burn severity map (Fig. 3.3) suggests that moderate burns ($1.5 \leqslant \text{GeoCBI} < 2.5$) occurred in the majority of the burned area, accounting for 63.5% of the land surface within the fire boundary. Low burns ($0 \leqslant \text{GeoCBI} < 1.5$) covered 3.7% of the surface, while severe burns ($2.5 \leqslant \text{GeoCBI} \leqslant 3.0$) affected 32.8% of the region. The estimated average GeoCBI scores of the three burn levels from low to severe are 1.26, 2.20 and 2.64, respectively; while the standard deviation of these scores is 0.27, 0.22 and 0.09, respectively.

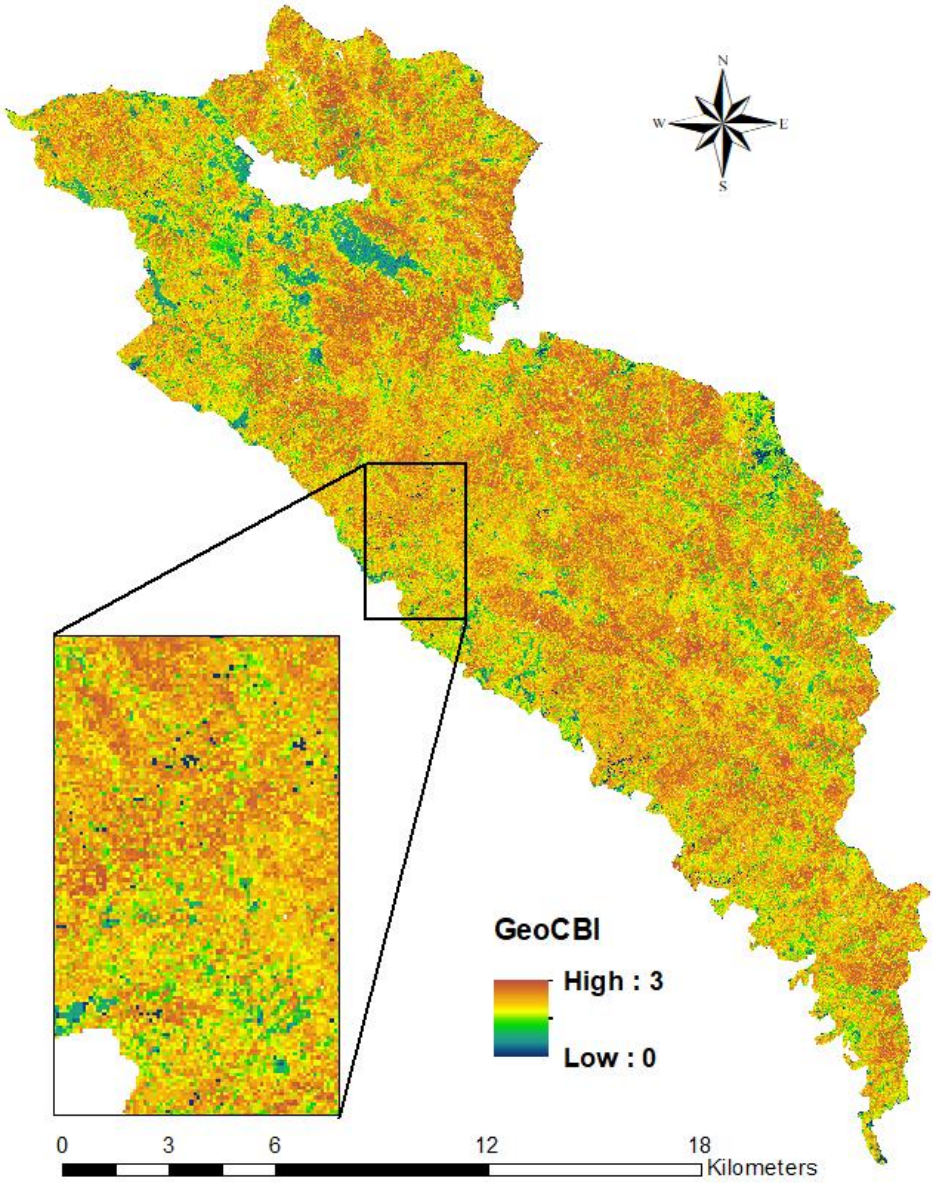

Fig. 3.3 Burn severity map with GeoCBI showing the severity of burn from low (0) to high (3).

3.2.4. Environmental factors

The environmental factors used in this study included three groups: climatic, topographic and fire-related factors. Both climate and topography are known to affect Sudden Oak Death outbreaks (Kelly et al., 2005). For climatic factors, we extracted the monthly mean precipitation and temperature in the disease's general reproductive season

from December to May (Meentemeyer et al., 2008a). The climatic data are part of a broader-scale database Daily surface weather data (Daymet) (https://daymet.ornl.gov), which is a continuous surface dataset available at a spatial resolution of 1 km for the Contiguous United States (Thornton et al., 2018).

Due to the complex topography in the study area, we used the fine-resolution 10 m Digital Elevation Model (DEM) from the National Elevation Dataset (NED; http://ned.usgs. gov/). Elevation, topographic moisture index (TWI), and solar insolation index (SII) were generated from the DEM. TWI describes the effect of topography on local moisture availability, which was calculated as the natural log of the ratio between the upslope contributing drainage area and the slope gradient of the grid cell (Moore et al., 1991). Specifically, the upslope contributing drainage area is the accumulation of flow from upstream. SII characterizes the potential mean solar irradiation for the rainy season (December to May), and was calculated using the cosine of illumination angle on slope equation (Dubayah, 1994).

We have further extracted two fire-related factors to quantify the effect of wildfire on disease spread, including burn severity (i.e., GeoCBI) for the trees within the fire boundary (i.e., unburned trees), and the shortest Euclidean distance to the fire boundary for the trees outside of the fire scar (i.e., unburned trees).

Table 3.1 Description of environmental factors.

Factor	Description
Climate	
● Precipitation	● Monthly mean precipitation (December to May)
● Temperature	● Monthly mean temperature (December to May)
Topography	
● Elevation	● Mean elevation
● TWI	● Mean Topographic Wetness Index
● SII	● Mean Solar Insolation Index (December to May)
Fire-related	
● Burn severity	● Mean burn severity
● Distance	● Shortest Euclidean distance to fire boundary

3.2.5. Statistical analysis

To evaluate the significance of wildfire in changing the disease spread rate, we compared four different circumstances. Temporally, we divided the disturbance time window into two: pre-fire (2005 to 2008), and post-fire (2013 to 2016). Here, we did not consider the post-fire early stage of tree recovery (2008-2013), because burned and disease-killed trees revealed high spectral similarities in remotely sensed data causing uncertainties to identify diseased trees (Chen et al., 2017). After five years of recovery (starting from 2013), fire-damaged tree crowns started to turn green, facilitating the identification of diseased trees (Chu et al., 2017). Spatially, we divided the study area into two: burned (area within the fire boundary) and unburned (area outside the fire boundary). In total, the four disturbances cases included: (a) pre-fire and burned, (b) pre-fire and unburned, (c) post-fire and burned, and (d) post-fire and unburned.

We fit a multiple regression model on the data for each of the four circumstances. The dependent variable was the average rate of disease spread during each of the two

time windows, while the independent variables varied. Specifically, for the pre-fire circumstances (a) and (b), the independent variables were climatic (precipitation and temperature), and topographic factors (elevation, TWI, and SII). Fire-related factors were not used because the Basin Complex Fire had not occurred yet. For the post-fire circumstance (c), the independent variables included climatic (precipitation and temperature), topographic (elevation, TWI, and SII), and burn severity factors. For case (d), we replaced burn severity with the shortest Euclidean distance to fire boundary. We intended to evaluate whether the proximity to wildfire may have played a role in disease progression. All models were developed at a 0.05 significance level using Akaike's information criterion (AIC) for determining the best model. The development of all the models was completed in the statistical environment R package (R Core Team, 2019).

All the factors were derived from 300 randomly sampled plots, in which 106 plots were within the burned area, and 194 plots were not. To ensure minimized spatial autocorrelation among the plots, we conducted a semivariogram analysis in the ArcGIS environment (Esri, Redlands, California, USA). The effective distance of spatial autocorrelation was found at 600 m, which was smaller than the average distance between our tested plots. We also set up a minimum distance value of 400 m between any two plot centers to avoid overlaps.

3.2.6. Landscape pattern analysis

Forest landscape may demonstrate a unique fragmentation pattern caused by the fire-disease disturbances. Here, we applied landscape metrics to quantify such patterns and compare the differences among the four circumstances: (a) pre-fire and burned, (b) pre-fire and unburned, (c) post-fire and burned, and (d) post-fire and unburned. While a

range of metrics have been examined to assess the effects of disease/insect outbreaks on landscape change (Chen et al. 2017; Coops et al., 2010; Gillanders et al. 2008; Lee et al., 2009), we selected and calculated four representative metrics in Fragstats (Table 3.2; McGarigal, 2014) with data from the annual disease maps (Fig. 3.2): Class Area (CA), Number of Patches (NP), Edge Density (ED), Mean Proximity Index (PROX_MN). These metrics were chosen to represent three categories of landscape, including area (CA and NP), shape (ED), and isolation/proximity (PROX_MN), respectively. We focused on healthy tree patches for calculating the metrics, aiming to understand how disturbances have affected the spatial patterns of tree recovery. The 8-neighbor rule was chosen for patch delineation treating both cardinal and diagonal pixels/cells as adjacent neighbors. This rule has been found to generate appropriate patches in previous studies (e.g., Chen et al. 2017; Richardson and Moskal, 2011).

Table 3.2 Descriptions of the selected landscape pattern indices applied to this study.

Landscape Metrix	Description	Category
Class Area (CA)	Total class area	Area
Number of Patches (NP)	Total number of patches in a class	Area
Edge Density (ED)	The ratio of total edges and total area	Shape
Mean Proximity Index (PROX_MN)	The degree of isolation and fragmentation of the corresponding patch type	Isolation/proximity

3.3. Results and discussion

3.3.1. Effects of wildfire on disease spread rate

Fire-related factors (Burn Severity and Distance) demonstrated a significant contribution to disease spread as revealed in the post-fire circumstances (Table 3.3).

Specifically, for the burned area, we found a significantly ($p < 0.01$) negative correlation between the rate of disease spread and burn severity (Table 3.3). This is consistent with the finding by Beh et al. (2012), who studied the same fire-disease disturbances and discovered a substantial decrease of the Sudden Oak Death causing pathogen due to the hot environmental condition and the removal of host trees. However, their analysis was based on the data acquired immediately following the wildfire, while ours reflected a longer-term recovery stage from 2013 to 2016. These findings together suggest a persistent, significant effect of wildfire on Sudden Oak Death spread for nearly a decade.

Table 3.3 Multiple regression models for the four disturbance scenarios.

Scenario	Independent Variable	Estimate	Standard Error	t Value
Pre-fire & Burned	Intercept	-4.6928	1.9801	-2.37*
	TWI	0.6014	0.1629	3.69***
Pre-fire & Unburned	Intercept	-7.1633	1.4831	-4.83***
	TWI	0.8136	0.2311	3.52***
Post-fire & Burned	Intercept	-8.6673	3.8866	-2.23*
	Burn Severity	-0.3456	0.1144	-3.02**
	Elevation	-0.0340	0.0121	-2.81**
Post-fire & Unburned	Intercept	-12.343	-4.1419	2.98**
	Distance	0.0036	0.0016	2.25*

* $p < 0.05$; ** $p < 0.01$; *** $p < 0.001$.

Outside of the fire scar, we found a significantly ($p < 0.05$) positive correlation between disease spread and the distance to the fire boundary (Table 3.3). That is, with the host trees being closer to the wildfire, they were less susceptible to disease attack after the fire. Because Sudden Oak Death spreads faster in the wet environment (Davidson et al. 2005, Condeso and Meentemeyer 2007), the fire-enhanced dry habitat may have suppressed disease activity. The elongated shape of the mountainous study site

may have also played a role (Fig. 3.1). The burned area was not well surrounded by the unburned area. As the distance from the fire boundary increased, the amount of host trees increased proportionally, significantly influencing the spatial pattern of disease spread.

When comparing the pre- and the post-fire model for the burned area, we found that elevation became significant, replacing the moisture factor TWI following fire occurrence (Table 3.3). According to the definition of TWI (Beven and Kirkby, 1979), small upslope drainage areas (e.g., ridges) have lower TWI values than the sites having large upslope areas (e.g., valleys). When the upslope areas are the same, the sites with steep slopes have lower TWI values than those having gentle slopes. Previous field studies discovered the positive contribution of moisture to the spread of Sudden Oak Death (Anacker et al., 2008; Cushman and Meentemeyer, 2008), which was also confirmed in our study in the pre-fire models. After the area was affected by the fire event, however, elevation started to demonstrate a significant effect on disease spread. This is possibly explained by the fact that severe burns occurred mostly at high altitudes along ridgetops (Chen et al., 2017), reducing the odds of pathogen survival and outbreak.

Although significant effects of the wildfire on disease spread are apparent in our findings, caution is advised when extrapolating the conclusions to other regions. In a case study examing the interaction between bark beetle and wildfire in the Northern Rocky Mountains, Harvey et al. (2014) did not find a direct relationship between beetle outbreak and post-fire tree seedling establishment, suggesting strong resilience of the lodgepole pine (*Pinus contorta* var. *latifolia*) dominated subalpine forests to the interacting disturbances. It is possible that post-fire disease or insect spread not only depends on the complex environmental factors (as discussed in our study), but also relies

on the spatial patterns of host tree recovery (Lombardero et al., 2011). Nevertheless, our results strongly suggest that these impacts are worth evaluating in a greater range of forest types.

3.3.2. Effects of disturbance interaction on forest fragmentation pattern

Prior to wildfire occurrence, the calculated landscape metrics were different for the burned versus the unburned area suggesting different fragmentation patterns (Fig. 3.4). Specifically, the burned area demonstrated lower CA and NP and higher ED than the unburned area. However, the trajectories (2005-2008) were similar for the two areas, i.e., decreased CA, increased NP, decreased ED, and decreased PROX_MN. Due to the increased disease severity showing an isolated, patchy progression pattern, the number of healthy tree patches decreased, with an exception in 2008. Meanwhile, the distance between those patches increased in general (Meentemeyer et al., 2012). Because healthy trees gradually declined in both areas, it was also reasonable for their edge density to show a downward trend. The effect of Sudden Oak Death outbreak on landscape change is not unique, which is similar to previous findings studying forest mortality caused by Mountain Pine Beetle (*Dendroctonus ponderosae*) (Coops et al., 2010; Vorster et al., 2017).

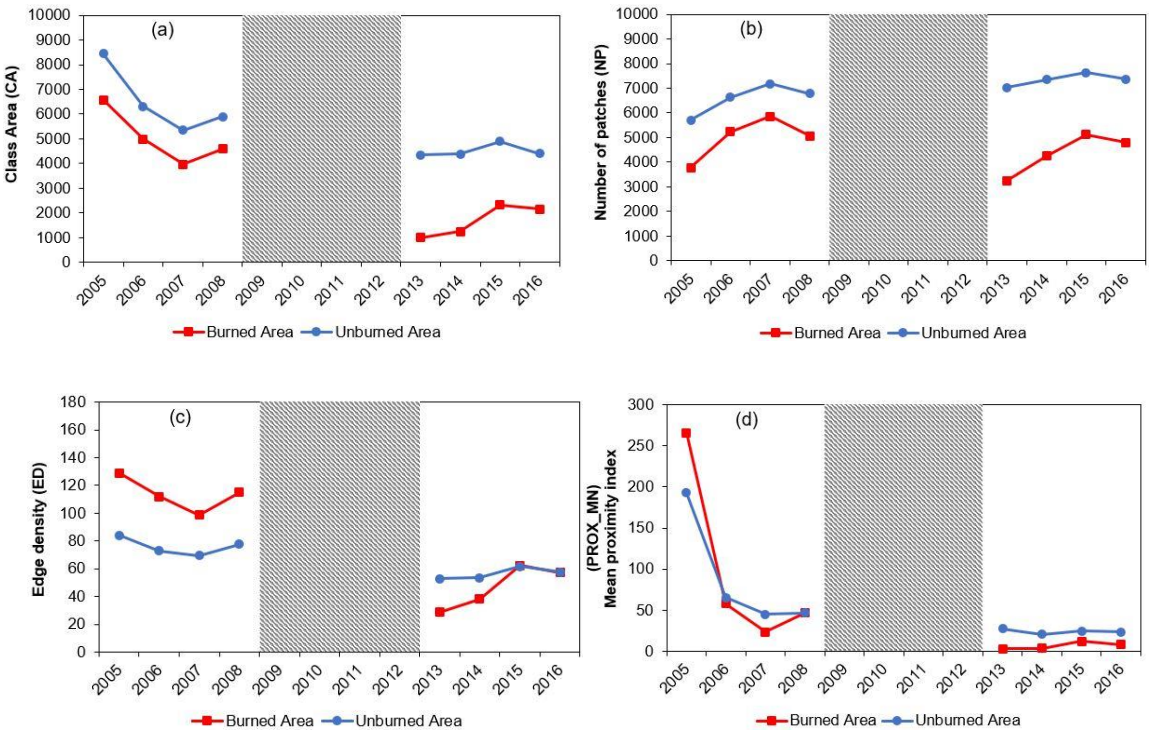

Fig. 3.4 Comparisons of the spatial patterns for the burned (red line) and the unburned area (blue line) in two time windows: pre-fire (2005-2008) and post-fire (2013-2016).

While Sudden Oak Death affected the burned and the unburned area in a similar way prior to fire occurrence in 2008, the forest landscapes revealed different changing patterns after the fire event (Fig. 3.4). Specifically, forests in the burned area remained at the recovery stage in the 2013-2016 period, where new and healthy tree patches continued to appear in the area, with CA and NP values showing an upward trend. The same reason also applies to the increase of edge density ED. The unburned area, however, showed relatively flat trending lines for all the four metrics, suggesting that the fragmentation level of the forest has reached a stable period. We further noticed that the wildfire, together with Sudden Oak Death had a long-term detrimental effect on forest recovery. Although the pre-fire ED and PROX_MN values for the burned area were

consistently higher than or equal to those for the unburned area, their relationship was reversed for most of the forest recovery period even after eight years of fire occurrence (Fig. 3.4). While the rate of forest recovery from wildfire depends on multiple factors (e.g., severity of fire, plant species, and climate), our study showed slower recovery rate than that of a forest in a similar Mediterranean climate (Viana-Soto et al., 2017) and the boreal ecoregion (Pickell et al., 2016).

3.4. Conclusion

In this study, we investigated the role of wildfire in changing the spread pattern of forest disease Sudden Oak Death in the Big Sur, California ecoregion. The use of remote-sensing-derived burn severity and disease-caused tree mortality maps allowed us to quantify the change in disease spread prior to (2005-2008) and after the fire event (2013-2016). The outcome of this research reveals a significant impact of wildfire on the post-fire spread of Sudden Oak Death. For the burned forest, the severity of fire exerted a significantly negative effect on the spread rate of the disease. Outside the fire scar, the distance to fire boundary showed a significantly positive effect on the spread rate of the disease. Our findings also suggest a slowdown of forest recovery due to the disease-fire interaction, as compared with several other disturbance studies. The spatial patterns of the forest landscape (e.g., edge density and isolation of healthy tree patches) were not able to return to the pre-fire status even after eight years of the fire event. Although our study focused on one case study, it adds to our knowledge of understanding disturbance interactions in a coastal forest ecosystem. Our results strongly suggest that these interactions are worth evaluating in a greater range of forest types. This research further

highlights the benefit of applying remote sensing data and products in spatially explicit, and high-frequency disturbance monitoring and evaluation at the landscape scale.

Acknowledgments

This research was supported by the National Science Foundation (EF-0622770) as part of the joint NSF-NIH Ecology and Evolution of Infectious Disease program, the North Carolina Space Grant, and the University of North Carolina at Charlotte CLAS Junior Faculty Development Award. The authors also gratefully acknowledge financial support from the USDA Forest Service – Pacific Southwest Research Station, and the Gordon & Betty Moore Foundation. We thank numerous contributors who provided vital field and laboratory support, including J. Geng, K. Aram, M. Beh, A. Brauer, M. Chan, C, DeLong, W. Dillon, K. Frangioso, A. Hohl, H. Mehl, A. Oguchi, E. Paddock, K. Pietrzak, M. Vaclavikova, J. Vieregge, L. Waks and A. Wickland.

References

Anacker, B.L., Rank, N.E., Hüberli, D., Garbelotto, M., Gordon, S., Harnik, T., Whitkus, R., Meentemeyer, R., 2008. Susceptibility to Phytophthora ramorum in a key infectious host: landscape variation in host genotype, host phenotype, and environmental factors. New Phytol. 177, 756–766.

Asner, G.P., 2013. Geography of forest disturbance. Proc. Natl. Acad. Sci. 110, 3711–3712.

Beh, M.M., Metz, M.R., Frangioso, K.M., Rizzo, D.M., 2012. The key host for an invasive forest pathogen also facilitates the pathogen's survival of wildfire in California forests. New Phytol. 196, 1145–1154.

Beh, M.M., Metz, M.R., Seybold, S.J., Rizzo, D.M., 2014. The novel interaction between Phytophthora ramorum and wildfire elicits elevated ambrosia beetle landing rates on tanoak, Notholithocarpus densiflorus. For. Ecol. Manag. 318, 21–33.

Beven, K.J., Kirkby, M.J., 1979. A physically based, variable contributing area model of basin hydrology. Hydrol. Sci. Bull. 24, 43–69.

Bonan, G.B., 2008. Forests and Climate Change: Forcings, Feedbacks, and the Climate Benefits of Forests. Science 320, 1444–1449.

Buma, B., Wessman, C.A., 2011. Disturbance interactions can impact resilience mechanisms of forests. Ecosphere 2, 1–13.

Canelles, Q., Aquilué, N., Duane, A., Brotons, L., 2019. From stand to landscape: modelling post-fire regeneration and species growth. Ecol. Model. 404, 103–111.

Chambers, J.C., Bradley, B.A., Brown, C.S., D'Antonio, C., Germino, M.J., Grace, J.B., Hardegree, S.P., Miller, R.F., Pyke, D.A., 2014. Resilience to stress and

disturbance, and resistance to Bromus tectorum L. invasion in cold desert shrublands of western North America. Ecosystems 17, 360–375.

Chen, G., He, Y., De Santis, A., Li, G., Cobb, R., Meentemeyer, R.K., 2017. Assessing the impact of emerging forest disease on wildfire using Landsat and KOMPSAT-2 data. Remote Sens. Environ. 195, 218–229.

Chen, G., Meentemeyer, R.K., 2016. Remote sensing of forest damage by diseases and insects. In: Weng, Q. (Ed.), Remote Sensing for Sustainability. CRC Press, Taylor & Francis Group, Boca Raton, Florida, pp. 145–162.

Chen, G., Metz, M.R., Rizzo, D.M., Meentemeyer, R.K., 2015. Mapping burn severity in a disease-impacted forest landscape using Landsat and MASTER imagery. Int. J. Appl. Earth Obs. Geoinf. 40, 91–99.

Chu, T., Guo, X., Takeda, K., 2017. Effects of burn severity and environmental conditions on post-fire regeneration in Siberian Larch forest. Forests 8, 1–27.

Coates, P.S., Ricca, M.A., Prochazka, B.G., Brooks, M.L., Doherty, K.E., Kroger, T., Blomberg, E.J., Hagen, C.A., Casazza, M.L., 2016. Wildfire, climate, and invasive grass interactions negatively impact an indicator species by reshaping sagebrush ecosystems. Proc. Natl. Acad. Sci. 113, 12745–12750.

Condeso, T.E., Meentemeyer, R.K., 2007. Effects of landscape heterogeneity on the emerging forest disease Sudden Oak Death. J. Ecol. 95, 364–375.

Coops, N.C., Gillanders, S.N., Wulder, M.A., Gergel, S.E., Nelson, T., Goodwin, N.R., 2010. Assessing changes in forest fragmentation following infestation using time series Landsat imagery. For. Ecol. Manag. 259, 2355–2365.

Cushman, J.H., Meentemeyer, R.K., 2008. Multi-scale patterns of human activity and the

incidence of an exotic forest pathogen. J. Ecol. 96, 766–776.

Daniel, C.J., Ter-Mikaelian, M.T., Wotton, B.M., et al., 2017. Incorporating uncertaintyinto forest management planning: timber harvest, wildfire and climate change in theboreal forest. For. Ecol. Manage. 400, 542–554.

Davidson, J.M., Wickland, A.C., Patterson, H.A., Falk, K.R., Rizzo, D.M., 2005. Transmission of Phytophthora ramorum in mixed evergreen forest in California. Phytopathology 95, 587–596.

Davis, R.S., Hood, S., Bentz, B.J., 2012. Fire-injured ponderosa pine provide a pulsed resource for bark beetles. Can. J. For. Res. 42, 2022–2036.

De Santis, A., Chuvieco, E., 2009. GeoCBI: a modified version of the composite burn index for the initial assessment of the short-term burn severity from remotely sensed data. Remote Sens. Environ. 113, 554–562.

De Santis, A., Chuvieco, E., Vaughan, P.J., 2009. Short-term assessment of burn severity using the inversion of PROSPECT and GeoSail models. Remote Sens. Environ. 113, 126–136.

Dubayah, R.C., 1994. Modeling a solar radiation topoclimatology for the Rio Grande river basin. J. Veg. Sci. 5, 627–640.

Gillanders, S.N., Coops, N.C., Wulder, M.A., Gergel, S.E., Nelson, T., 2008. Multitemporal remote sensing of landscape dynamics and pattern change: describing natural and anthropogenic trends. Prog. Phys. Geogr. 32, 503–528.

Gornish, E.S., Ambrozio dos Santos, P., 2016. Invasive species cover, soil type, and grazing interact to predict long-term grassland restoration success. Restor. Ecol. 24, 222–229.

Green, R.O., Eastwood, M.L., Sarture, C.M., Chrien, T.G., Aronsson, M., Chippendale, B.J., Faust, J.A., Pavri, B.E., Chovit, C.J., Solis, M.S., Olah, M.R., Williams, O., 1998. Imaging spectroscopy and the airborne visible infrared imaging spectrometer (AVIRIS). Remote Sens. Environ. 65, 227–248.

Hatala, J. a., Crabtree, R. L., Halligan, K. Q., Moorcroft, P. R., 2010. Landscape-scale patterns of forest pest and pathogen damage in the Greater Yellowstone Ecosystem. Remote Sens. Environ. 114, 375–384.

Harvey, B.J., Donato, D.C. and Turner, M.G., 2014. Recent mountain pine beetle outbreaks, wildfire severity, and postfire tree regeneration in the US Northern Rockies. Proc. Natl. Acad. Sci. 111,15120–15125.

He, Y., Chen, G., De Santis, A., Roberts, D.A., Zhou, Y., Meentemeyer, R.K., 2019a. A disturbance weighting analysis model (DWAM) for mapping wildfire burn severity in the presence of forest disease. Remote Sens. Environ. 221, 108–121.

He, Y., Chen, G., Potter, C., Meentemeyer, R.K., 2019b. Integrating multi-sensor remote sensing and species distribution modeling to map the spread of emerging forest disease and tree mortality. Remote Sens. Environ. 231, 111238.

Hultquist, C., Chen, G., Zhao, K., 2014. A comparison of Gaussian process regression, random forests and support vector regression for burn severity assessment in diseased forests. Remote Sens. Lett. 5, 723–732.

Janousek, W.M., Hicke, J.A., Meddens, A.J. and Dreitz, V.J., 2019. The effects of mountain pine beetle outbreaks on avian communities in lodgepole pine forests across the greater Rocky Mountain region. For. Ecol. Manage. 444, 374–381.

Jenkins, M.J., Runyon, J.B., Fettig, C.J., Page, W.G., Bentz, B.J., 2014. Interactions

among the Mountain Pine Beetle, fires, and fuels. For. Sci. 60, 489–501.

Kane, J.M., Varner, J.M., Metz, M.R., van Mantgem, P.J., 2017. Characterizing interactions between fire and other disturbances and their impacts on tree mortality in western US Forests. For. Ecol. Manag. 405,188–199.

Kelly, M., Shaari, D., Guo, Q., Liu, D., 2005. Modeling risk for SOD nationwide: what are the effects of model choice on risk prediction? In: Sudden oak death second science symposium. January 18–21, USDA Forest Service General Technical Report PSW-GTR-196, Monterey, CA.

Keeley, J.E., 2009. Fire intensity, fire severity and burn severity: a brief review and suggested usage. Int. J. Wildland Fire 18, 116–126.

Lee, S.-W., Lee, M.-B., Lee, Y.-G., Won, M.-S., Kim, J.-J., Hong, S., 2009. Relationship between landscape structure and burn severity at the landscape and class levels in Samchuck, South Korea. For. Ecol. Manag. 258, 1594–1604.

Lentile, L.B., Holden, Z.A., Smith, A.M.S., Falkowski, M.J., Hudak, A.T., Morgan, P., Lewis, A.A., Gessler, P.E., Benson, N.C., 2006. Remote sensing techniques to assess active fire characteristics and post-fire effects. Int. J. Wildland Fire 15, 319–345.

Loehman, R.A., Keane, R.E., Holsinger, L.M., Wu, Z., 2017. Interactions of landscape disturbances and climate change dictate ecological pattern and process: spatial modeling of wildfire, insect, and disease dynamics under future climates. Landsc. Ecol. 1–13.

Lombardero, M.J. and Ayres, M.P., 2011. Factors influencing bark beetle outbreaks after forest fires on the Iberian Peninsula. Environ. Entomol. 40, 1007–1018.

McGarigal, K., 2014. FRAGSTATS Help. University of Massachusetts, Amherst, MA (209 pp.).

Meentemeyer, R.K., Anacker, B.L., Mark, W. and Rizzo, D.M., 2008a. Early detection of emerging forest disease using dispersal estimation and ecological niche modeling. Ecol. Appl. 18, 377–90.

Meentemeyer, R.K., Haas, S.E., Václavík, T., 2012. Landscape epidemiology of emerging infectious diseases in natural and human-altered ecosystems. Annu. Rev. Phytopathol. 50, 379–402.

Meentemeyer, R.K., Rank, N.E., Shoemaker, D.A., Oneal, C.B., Wickland, A.C., Frangioso, K.M., Rizzo, D.M., 2008b. Impact of sudden oak death on tree mortality in the Big Sur ecoregion of California. Biol. Invasions 10, 1243–1255.

Meigs, G. W., Kennedy, R. E., Gray, A. N., Gregory, M. J., 2015. Spatiotemporal dynamics of recent mountain pine beetle and western spruce budworm outbreaks across the Pacific Northwest Region, USA. For. Ecol. Manag. 339, 71–86.

Meng, R., Wu, J., Schwager, K.L., Zhao, F., Dennison, P.E., Cook, B.D., Brewster, K., Green, T.M., Serbin, S.P., 2017. Using high spatial resolution satellite imagery to map forest burn severity across spatial scales in a Pine Barrens ecosystem. Remote Sens. Environ. 191, 95–109.

Moore, I.D., Grayson, R.B., Ladson, A.R., 1991. Digital terrain modelling. A review of hydrological, geomorphological, and biological applications. Hydrol. Proc. 5, 3–30.

Pasquarella, V.J., Bradley, B.A., Woodcock, C.E., 2017. Near-real-time monitoring of insect defoliation using Landsat time series. Forests 8, p.275.

Pickell, P. D., Hermosilla, T., Frazier, R. J., Coops, N. C., Wulder, M. A., 2016. Forest

recovery trends derived from Landsat time series for North American boreal forests. Int. J. Remote Sens. 37(1), 138–149.

Powell, E.N., Townsend, P.A., Raffa, K.F., 2012. Wildfire provides refuge from local extinction but is an unlikely driver of outbreaks by mountain pine beetle. Ecol. Monogr. 82, 69–84.

Quintano, C., Fernandez-Manso, A. and Roberts, D.A., 2017. Burn severity mapping from Landsat MESMA fraction images and Land Surface Temperature. Remote Sens. Environ. 190, 83–95.

R Core Team, 2019. R: A Language and Environment for Statistical Computing. R Foundation for Statistical Computing, Vienna, Austria URL. https://www.r-project.org/

Richardson, J.J., Moskal, L.M., 2011. Strengths and limitations of assessing forest density and spatial configuration with aerial LiDAR. Remote Sens. Environ. 115, 2640–2651.

Rizzo, D.M., Garbelotto, M., Hansen, E.M., 2005. Phytophthora ramorum: integrative research and management of an emerging pathogen in California and Oregon forests. Annu. Rev. Phytopathol. 43, 309–35.

Roberts, D.A., Gardner, M., Church, R., Ustin, S., Scheer, G., Green, R.O., 1998. Mapping chaparral in the Santa Monica Mountains using multiple endmember spectral mixture models. Remote Sens. Environ. 65, 267–279.

Sánchez-Pinillos, M., Leduc, A., Ameztegui, A., Kneeshaw, D., Lloret, F., Coll, L., 2019. Resistance, Resilience or Change: Post-disturbance Dynamics of Boreal Forests After Insect Outbreaks. Ecosystems 23, 1–16.

Simler, A.B., Metz, M.R., Frangioso, K.M., Meentemeyer, R.K., Rizzo, D.M., 2018. Novel disturbance interactions between fire and an emerging disease impact survival and growth of resprouting trees. Ecology, 99, 2217–2229.

Skowronek, S., Ewald, M., Isermann, M., Van De Kerchove, R., Lenoir, J., Aerts, R., Warrie, J., Hattab, T., Honnay, O., Schmidtlein, S., Rocchini, D., 2017. Mapping an invasive bryophyte species using hyperspectral remote sensing data. Biol. Invasions 19, 239–254.

Thornton, M.M., Thornton, P.E., Wei, Y., Mayer, B.W., Cook, R.B., VoseR, S., 2018. Daymet: Monthly Climate Summaries on a 1-km Grid for North America, Version 3. ORNL DAAC, Oak Ridge, Tennessee, USA.

Turner, M.G., 2010. Disturbance and landscape dynamics in a changing world. Ecology, 91, 2833-2849.

USDA Forest Service, 2008. Executive Summary: Basin Complex Fire/Indians Fire BAER Initial Assessment (16 pp.).

Václavík, T., Meentemeyer, R.K., 2012. Equilibrium or not? Modelling potential distribution of invasive species in different stages of invasion. Divers. Distrib. 18, 73–83.

Viana-Soto, A., Aguado, I., Martínez, S., 2017. Assessment of post-fire vegetation recovery using fire severity and geographical data in the mediterranean region (Spain). Environments 4 (4), 90.

Vorster, A.G., Evangelista, P.H., Stohlgren, T.J., Kumar, S., Rhoades, C.C., Hubbard, R.M., Cheng, A.S. and Elder, K., 2017. Severity of a mountain pine beetle outbreak across a range of stand conditions in Fraser Experimental Forest, Colorado, United

States. For. Ecol. Manag. 389, 116–126.

White, J.D., Ryan, K.C., Key, C.C., Running, S.W., 1996. Remote sensing of forest fire severity and vegetation recovery. Int. J. Wildland Fire 6, 125−136.

Wulder, M.A., Dymond, C.C., White, J.C., Leckie, D.G., Carroll, A.L., 2006. Surveying mountain pine beetle damage of forests: a review of remote sensing opportunities. For. Ecol. Manag. 221, 27–41.

Wulder, M.A., Masek, J.G., Cohen, W.B., Loveland, T.R., Woodcock, C.E., 2012. Opening the archive: How free data has enabled the science and monitoring promise of Landsat. Remote Sens. Environ. 122, 2–10.

CONCLUSIONS

Dissertation Conclusion

The purpose of this dissertation is to increase our understanding of the interacting disturbances of wildfire and EIDs in forest ecosystems through remote sensing technology. Sudden oak death is used as an example of a chronic EID disturbance that has caused widespread tree mortality in the Big Sur, California ecoregion, which interacted with a short-term wildfire disturbance which occurred in 2008. The outcomes from this dissertation have the potential to advance the scientific understanding of how a prior disturbance regime (i.e., disease) influences the spatial and temporal response of a forest ecosystem to another disturbance (i.e., wildfire).

In this dissertation, my novel Ph.D. contribution is the integration of multiple satellite and airborne sensors to investigate how environmental disturbances (i.e., EIDs and wildfire) interact, and how such novel interactions affect a forest ecosystem. Specifically, in Chapter 1, I integrated multi-sensor remote sensing and species distribution modeling, which for the first time applied species distribution modeling to refine a remote sensing model for remotely identifying the cause of tree mortality related to sudden oak death. In Chapter 2, my novel contribution was to consider the effects of pre-fire disease disturbances, which has significantly improved the results in burn severity mapping. None of the other existing remote sensing models have accounted for the non-fire disturbances in burn severity modeling. In Chapter 3, I applied the remote sensing products of burn severity and disease maps to study the spatial patterns of fire effects on disease spread and post-fire forest recovery. The findings were not revealed in previous studies due to their limited field observations.

Future Research

The study in this dissertation also provides some possibilities for future research. The availability of NASA's HyspIRI images provides the research community with new opportunities for mapping disease/insect mortality and detecting the changes with high spatial and temporal accuracies. As suggested by He et al. (2019b), using hyperspectral data with enhanced spectral signatures from the shortwave infrared portion of the spectrum may contribute to the discrimination among disturbances. Because different types of disturbances may reveal varying progression patterns over time, high-resolution time series images have the potential to capture those patterns. Although DWAM has proven its ability to mitigate the overestimation of burn severity, this model has not been evaluated for other data sources (e.g., MASTER and AVIRIS). In addition, a comprehensive comparison is needed to clearly understand the performance of existing models, including physical and empirical models (e.g., random forests, joint deep learning) in the face of hyperspectral imagery. The comparison would also benefit natural resource and ecosystem management. Meanwhile, the performance of those models is highly depended upon the reliability and sufficiency of field samples and is site-specific, which reduce the generality across complex geographic conditions. Physical models have been used to address such limitation due to their wide generality and applicability. Nevertheless, current physical models have been calibrated and validated only in the healthy forests without accounting for other pre-fire disturbances. More efforts should be placed in terms of the compound effects of multiple disturbances. Another goal is to adjust the radiative transfer models (i.e., leaf-level PROSPECT and canopy-level GeoSail models) to simulate the physical interactions between radiation

and burned canopies under compound disturbance situation, establishing the correspondence between reference spectra and tree damages that are caused by fires and diseases.

REFERENCES

Assal, T.J., Sibold, J., Reich, R., 2014. Modeling a Historical Mountain pine beetle outbreak using Landsat MSS and multiple lines of evidence. Remote Sens. Environ. 155, 275–288.

Anderegg, W.R.L., Kane, J.M., Anderegg, L.D.L., 2013. Consequences of widespread tree mortality triggered by drought and temperature stress. Nat. Clim. Chang. 3, 30–36.

Asner, G.P., 2013. Geography of forest disturbance. Proc. Natl. Acad. Sci. 110, 3711–3712.

Beh, M.M., Metz, M.R., Frangioso, K.M., Rizzo, DM., 2012 The key host for an invasive forest pathogen also facilitates the pathogen's survival of wildfire in California forests. New Phytol. 196, 1145–1154.

Chen, G., He, Y., De Santis, A., Li, G., Cobb, R., Meentemeyer, R.K., 2017. Assessing the impact of emerging forest disease on wildfire using Landsat and KOMPSAT-2 data. Remote Sens. Environ. 195, 218–229.

Chen, G., Meentemeyer, R.K., 2016. Remote sensing of forest damage by diseases and insects. In: Weng, Q. (Ed.), Remote Sensing for Sustainability. CRC Press, Taylor & Francis Group, Boca Raton, Florida, pp. 145–162.

Chen, G., Metz, M.R., Rizzo, D.M., Dillon, W.W., Meentemeyer, R.K., 2015a. Object-based assessment of burn severity in diseased forests using high-spatial and high-spectral resolution MASTER airborne imagery. ISPRS J. Photogramm. Remote Sens. 102, 38–47.

Chen, G., Metz, M.R., Rizzo, D.M., Meentemeyer, R.K., 2015b. Mapping burn severity

in a disease-impacted forest landscape using Landsat and MASTER imagery. Int. J. Appl. Earth Obs. Geoinf. 40, 91–99.

Chuvieco, E., Riaño, D., Danson, F.M., Martin, P., 2006. Use of a radiative transfer model to simulate the postfire spectral response to burn severity. J. Geophys. Res. Biogeosci. 111 (G4), 1–15.

Chuvieco, E., Mouillot, F., van der Werf, G.R., San Miguel, J., Tanasse, M., Koutsias, N., García, M., Yebra, M., Padilla, M., Gitas, I., Heil, A., 2019. Historical background and current developments for mapping burned area from satellite Earth observation. Remote Sens. Environ. 225, 45–64.

Cobb, R. C., Hartsough, P., Ross, N., Klein, J., LaFever, D. H., Frankel, S. J., Rizzo, D. M. 2017. Resiliency or restoration: Management of sudden oak death before and after outbreak. For. Phytophthoras 7, 1–14.

Daniel, C.J., Ter-Mikaelian, M.T., Wotton, B.M., Rayfield, B., Fortin, M.J., 2017. Incorporating uncertainty into forest management planning: Timber harvest, wildfire and climate change in the boreal forest. For. Ecol. Manag. 400, 542–554.

Davis, R.S., Hood, S., Bentz, B.J., 2012. Fire-injured ponderosa pine provide a pulsed resource for bark beetles. Can. J. For. Res. 42, 2022–2036.

De Santis, A., Chuvieco, E., Vaughan, P.J., 2009. Short-term assessment of burn severity using the inversion of PROSPECT and GeoSail models. Remote Sens. Environ. 113, 126–136.

Dlamini, L.S., Little, K.M., Sivparsad, B., Nadel, R., 2019. Quantifying the impact of foliar insects on two Eucalyptus hybrids in Zululand, northern KwaZulu-Natal, South Africa. S. Afr. J. Sci. 3, 129–135.

Fernandez-Manso, A., Quintano, C., Roberts, D.A., 2016. Burn severity influence on post- fire vegetation cover resilience from Landsat MESMA fraction images time series in Mediterranean forest ecosystems. Remote Sens. Environ. 184, 112–123.

Hatala, J. A., Crabtree, R. L., Halligan, K. Q., Moorcroft, P. R., 2010. Landscape-scale patterns of forest pest and pathogen damage in the Greater Yellowstone Ecosystem. Remote Sens. Environ. 114, 375–384.

He, Y., Chen, G., De Santis, A., Roberts, D.A., Zhou, Y., Meentemeyer, R.K., 2019a. A disturbance weighting analysis model (DWAM) for mapping wildfire burn severity in the presence of forest disease. Remote Sens. Environ. 221, 108–121.

He, Y., Chen, G., Potter, C., Meentemeyer, R.K., 2019b. Integrating multi-sensor remote sensing and species distribution modeling to map the spread of emerging forest disease and tree mortality. Remote Sens. Environ. 231, 111238.

He, Y., Chen, G., Zhao, K., Meentemeyer, R.K., Wildfire affects the spread of forest disease Sudden Oak Death and post-fire tree recovery. For. Ecol. Manage.

Hultquist, C., Chen, G., Zhao, K., 2014. A comparison of Gaussian process regression, random forests and support vector regression for burn severity assessment in diseased forests. Remote Sens. Lett. 5, 723–732.

Janousek, W.M., Hicke, J.A., Meddens, A.J., Dreitz, V.J., 2019. The effects of mountain pine beetle outbreaks on avian communities in lodgepole pine forests across the greater Rocky Mountain region. For. Ecol. Manage. 444, 374–381.

Kane, J.M., Varner, J.M., Metz, M.R., van Mantgem, P.J., 2017. Characterizing interactions between fire and other disturbances and their impacts on tree mortality in western US Forests. For. Ecol. Manag. 405,188–199.

Keeley, J.E., 2009. Fire intensity, fire severity and burn severity: a brief review and suggested usage. Int. J. Wildland Fire 18, 116–126.

Key, C.H., Benson, N.C., 2006. Landscape assessment (LA) sampling and analysis methods. In: USDA Forest Service General Technical Report, RMRS-GTR-164-CD.

Kokaly, R.F., Rockwell, B.W., Haire, S.L., King, T.V.V., 2007. Characterization of post-fire surface cover, soils, and burn severity at the Cerro Grande Fire, New Mexico, using hyperspectral and multispectral remote sensing. Remote Sens. Environ. 106, 305–325.

Lee, S.-W., Lee, M.-B., Lee, Y.-G., Won, M.-S., Kim, J.-J., Hong, S., 2009. Relationship between landscape structure and burn severity at the landscape and class levels in Samchuck, South Korea. For. Ecol. Manag. 258, 1594–1604.

Lentile, L.B., Holden, Z.A., Smith, A.M.S., Falkowski, M.J., Hudak, A.T., Morgan, P., Lewis, A.A., Gessler, P.E., Benson, N.C., 2006. Remote sensing techniques to assess active fire characteristics and post-fire effects. Int. J. Wildland Fire 15, 319–345.

Lewis, S., Lentile, L., Hudak, A., Robichaud, P., Morgan, P., Bobbitt, M., 2007. Mapping ground cover using hyperspectral remote sensing after the 2003 Simi and old wildfires in Southern California. Fire Ecol. 3, 109–128.

Loehman, R.A., Keane, R.E., Holsinger, L.M., Wu, Z., 2017. Interactions of landscape disturbances and climate change dictate ecological pattern and process: spatial modeling of wildfire, insect, and disease dynamics under future climates. Landsc. Ecol. 1–13.

López-García, M.J., Caselles, V., 1991. Mapping burns and natural reforestation using

thematic mapper data. Geocarto Int. (1), 31–37.

Meddens, A.J.H., Hicke, J.A., Vierling, L.A., 2011. Evaluating the potential of multi-spectral imagery to map multiple stages of tree mortality. Remote Sens. Environ. 115, 1632–1642.

Meng, R., Wu, J., Schwager, K.L., Zhao, F., Dennison, P.E., Cook, B.D., Brewster, K., Green, T.M., Serbin, S.P., 2017. Using high spatial resolution satellite imagery to map forest burn severity across spatial scales in a Pine Barrens ecosystem. Remote Sens. Environ. 191, 95–109.

Metz, M.R., Varner, J., Frangioso, K., 2013. Unexpected redwood mortality from synergies between wildfire and an emerging infectious disease. Ecology 94, 2152–2159.

Miller, J.D., Thode, A.E., 2007. Quantifying burn severity in a heterogeneous landscape with a relative version of the delta normalized burn ratio (dNBR). Remote Sens. Environ. 109, 66–80.

Oboite, F.O., Comeau, P.G., 2019. Release response of black spruce and white spruce following overstory lodgepole pine mortality due to mountain pine beetle attack. Forest For. Ecol. Manag. 432, 446–454.

Pasquarella, V.J., Bradley, B.A., Woodcock, C.E., 2017. Near-real-time monitoring of insect defoliation using Landsat time series. Forests 8, 275.

Pettinari, M., Chuvieco, E., 2017. Fire behavior simulation from global fuel and climatic information. Forests 8, 179.

Potterf, M., Nikolov, C., Kočická, E., Ferenčík, J., Mezei, P., Jakuš, R., 2019. Landscape-level spread of beetle infestations from windthrown-and beetle-killed

trees in the non-intervention zone of the Tatra National Park, Slovakia (Central Europe). For. Ecol. Manag. 432, 489-500.

Powell, E.N., Townsend, P.A., Raffa, K.F., 2012. Wildfire provides refuge from local extinction but is an unlikely driver of outbreaks by mountain pine beetle. Ecol. Monogr. 82, 69–84.

Quintano, C., Fernandez-Manso, A., Roberts, D.A., 2017. Burn severity mapping from Landsat MESMA fraction images and Land Surface Temperature. Remote Sens. Environ. 190, 83–95.

Riley, K.L., Williams, A.P., Urbanski, S.P., Calkin, D.E., Short, K.C., O'Connor, C.D., 2019. Will Landscape Fire Increase in the Future? A Systems Approach to Climate, Fire, Fuel, and Human Drivers. Curr. Pollut. Rep. 1–16.

Rizzo, D.M., Garbelotto, M., Hansen, E.M., 2005. Phytophthora ramorum: integrative research and management of an emerging pathogen in California and Oregon forests. Annu. Rev. Phytopathol. 43, 309–35.

Sánchez-Pinillos, M., Leduc, A., Ameztegui, A., Kneeshaw, D., Lloret, F., Coll, L., 2019. Resistance, Resilience or Change: Post-disturbance Dynamics of Boreal Forests After Insect Outbreaks. Ecosystems 23, 1–16.

Seidl, R., Schelhaas, M.J., Rammer, W., Verkerk, P.J., 2014. Increasing forest disturbances in Europe and their impact on carbon storage. Nat. Clim. Chang. 4, 806–810.

Simler, A.B., Metz, M.R., Frangioso, K.M., Meentemeyer, R.K., Rizzo, D.M., 2018. Novel disturbance interactions between fire and an emerging disease impact survival and growth of resprouting trees. Ecology 99, 2217–2229.

Skowronek, S., Ewald, M., Isermann, M., Van De Kerchove, R., Lenoir, J., Aerts, R., Warrie, J., Hattab, T., Honnay, O., Schmidtlein, S., Rocchini, D., 2017. Mapping an invasive bryophyte species using hyperspectral remote sensing data. Biol. Invasions 19, 239–254.

Turner, M.G., 2010. Disturbance and landscape dynamics in a changing world. Ecology 91, 2833–2849.

Turner, M.G., Baker, W.L., Peterson, C.J., Peet, R.K., 1998. Factors influencing succession: lessons from large, infrequent natural disturbances. Ecosystems 1, 511–523.

Václavík, T., Meentemeyer, R.K., 2012. Equilibrium or not? Modelling potential distribution of invasive species in different stages of invasion. Divers. Distrib. 18, 73–83.

Václavík, T., Meentemeyer, R.K., 2009. Invasive species distribution modeling (iSDM): are absence data and dispersal constraints needed to predict actual distributions? Ecol. Modell. 220, 3248–3258.

Vaughn, N.R., Asner, G.P., Brodrick, P.G., Martin, R.E., Heckler, J.W., Knapp, D.E., Hughes, R.F., 2018. An approach for high-resolution mapping of Hawaiian metrosideros forest mortality using laser-guided imaging spectroscopy. Remote Sens. 10, 502.

Veraverbeke, S., Dennison, P., Gitas, I., Hulley, G., Kalashnikova, O., Katagis, T., Kuai, L., Meng, R., Roberts, D., Stavros, N., 2018. Hyperspectral remote sensing of fire: State-of-the-art and future perspectives. Remote Sens. Environ. 216, 105–121.

Wulder, M.A., Dymond, C.C., White, J.C., Leckie, D.G., Carroll, A.L., 2006. Surveying

mountain pine beetle damage of forests: a review of remote sensing opportunities. For. Ecol. Manag. 221, 27–41.